Doctoral Dissertation

Studies on the Development of n-Type Organic Semiconductors for Organic Solar Cells by Engineering Frontier Orbitals and Molecular Arrangement
(フロンティア軌道と分子の配列設計に基づく
有機太陽電池用 n 型有機半導体の開発に関する研究)

WANG KAI

May 2025

Division of Applied Chemistry
Graduate School of Engineering,
The University of Osaka

Preface

The study presented in this thesis has been carried out under the guidance of Professor Yutaka Ie at SANKEN (The Institute of Scientific and Industrial Research), The University of Osaka from 2021 to 2025.

This work focuses on the design and development of novel non-fullerene acceptors for organic solar cells by structural modification of the ITIC backbone. Through tuning the molecular geometry and substituents, and studying their effects on aggregation behavior, exciton binding energy, and interfacial energy levels, the relationship between molecular structure and device performance was systematically investigated. The findings of this study provide insights into molecular design strategies aimed at improving the efficiency and stability of organic solar cells.

Table of Contents

General Introduction

Energy is fundamental to human survival and development. Throughout history, humans have continuously explored and utilized various forms of energy. From early practices such as fire-making and wood burning to modern methods like oil extraction and coal combustion, and now the adoption of new energy sources such as wind, nuclear, and solar energy, the dependence on energy has steadily increased alongside growing consumption. However, traditional energy sources like oil and natural gas produce significant greenhouse gases and toxic sulfides during use and combustion, exacerbating global warming, and posing severe threats to the environment and human health. Developing clean energy is essential for achieving sustainable development.

Among renewable energy sources, solar energy stands out as an inexhaustible resource. In the context of the rapid depletion of traditional energy reserves, advancing the solar energy industry has become increasingly crucial. Photovoltaic (PV) power generation, a technology that converts solar energy into electricity, is a clean, renewable, and rapidly evolving energy solution that has garnered extensive global attention. As shown in **Figure 1**, the latest efficiency chart released by the U.S. National Renewable Energy Laboratory indicates that the efficiency of multi-junction inorganic solar cells has reached 47.6%, while single-crystal and polycrystalline silicon cells have achieved efficiencies of 27.6% and 23.3%, respectively.[1] Although the efficiency of these inorganic silicon cells is sufficient for practical applications, their development remains constrained by high production costs and environmental concerns.

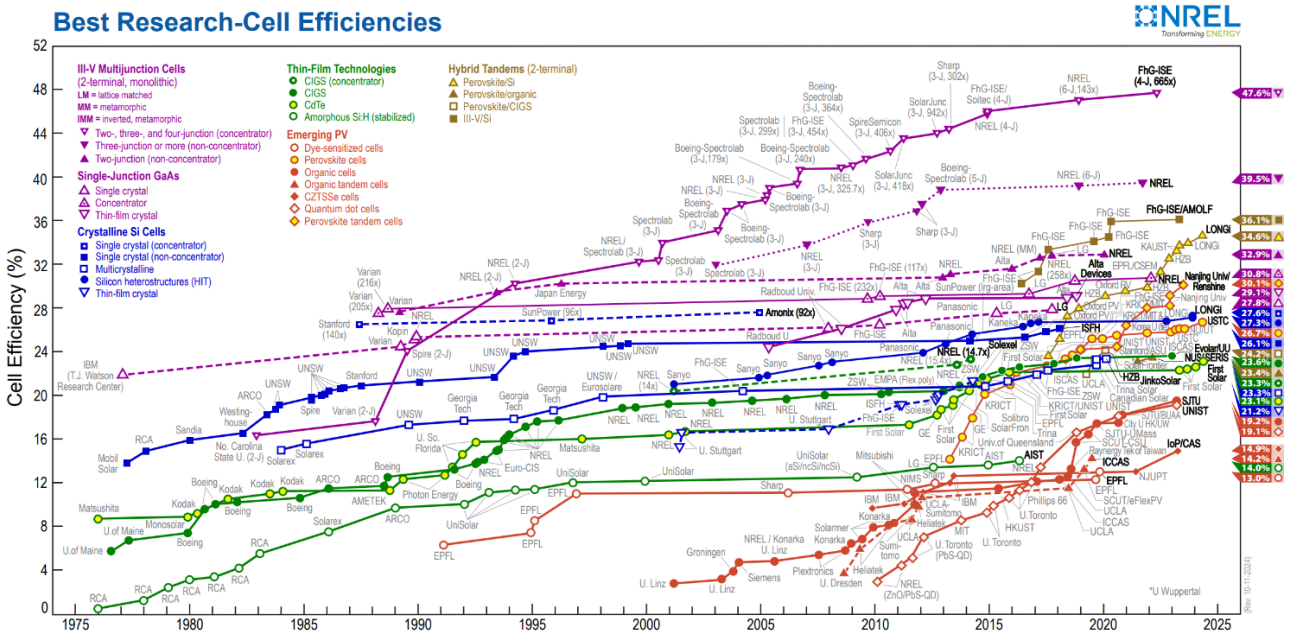

Figure 1. Highest certified efficiency of various types of photovoltaic devices.

In contrast, organic solar cells (OSCs) represent a promising new photovoltaic technology. With abundant sources of active layer materials, OSCs offer advantages such as light weight, low cost, solution-processability, and the potential for flexible and semi-transparent designs. These attributes have made OSCs a focal point of research. The photoelectric properties of organic materials can be finely tuned through chemical synthesis, enabling significant improvements in power conversion efficiency (PCE). Recent reports indicate that the efficiency of

single-junction OSCs has surpassed 20%.[2] As a result, organic photovoltaics hold immense potential for future development and practical applications.

As early as 1958, Kallmann et al. discovered the photovoltaic phenomenon in their research on single crystal anthracene, which produced a photovoltaic efficiency of less than 0.1%.[3] Due to the low efficiency, scientists did not pay enough attention to it. Later in 1986, Deng et al. used copper phthalocyanine as a donor and perylene derivatives as an acceptor, and used the evaporation method to process the device.[4] They reported the first double-layer organic photovoltaic device. After further research, this device can greatly improve the dissociation efficiency of excitons at the donor-acceptor interface. Finally, the efficiency of the device reached about 1%. This study attracted the attention of researchers, and since then, OSCs have gradually developed. In 1992, Heeger et al. discovered that the conjugated polymer MEH-PPV can transfer electrons to fullerene C60 in a very short time (fs level).[5] This phenomenon provides important theoretical support for the development of fullerene-based organic photovoltaic cells. Later in 1995, Heeger et al. first proposed the concept of bulk heterojunction (BHJ) in the field of organic photovoltaics.[6] They blended the donor and acceptor and prepared organic photovoltaic devices by solution processing and spin coating. Due to the blending of the donor and acceptor, many small donor/acceptor contact surfaces can be formed between them, which is very conducive to the dissociation of excitons and charge transfer. Finally, an efficiency of 2.9% was obtained. This bulk heterojunction battery is not only simple to process, but also has greatly improved efficiency. Until today, most of the research on organic solar cells by scientists is based on this structure.[7-10]

Since the advent of the BHJ structure, scientists have continuously improved and optimized it on this basis to improve the photovoltaic efficiency of the device. For example, using trans-structure devices to increase current, preparing new polymer donor materials, developing interface materials to match the energy levels between the active layer and the electrode, and adopting ternary strategies to further improve device efficiency.[11-13] In the early days, due to the characteristics of fullerene itself being relatively simple and easy to obtain, its application in organic solar cells received widespread attention. The latest equipment performance of organic solar cells using fullerene can reach more than 10%.[14] However, due to its narrow absorption band, structural rigidity, high cost and low band tunability, the energy loss of fullerene-based devices is too high, making it difficult to further improve photovoltaic efficiency (**Figure 2, left**).[15] Gradually, researchers began to shift their attention to non-fullerene acceptors (NFAs).[16-18]

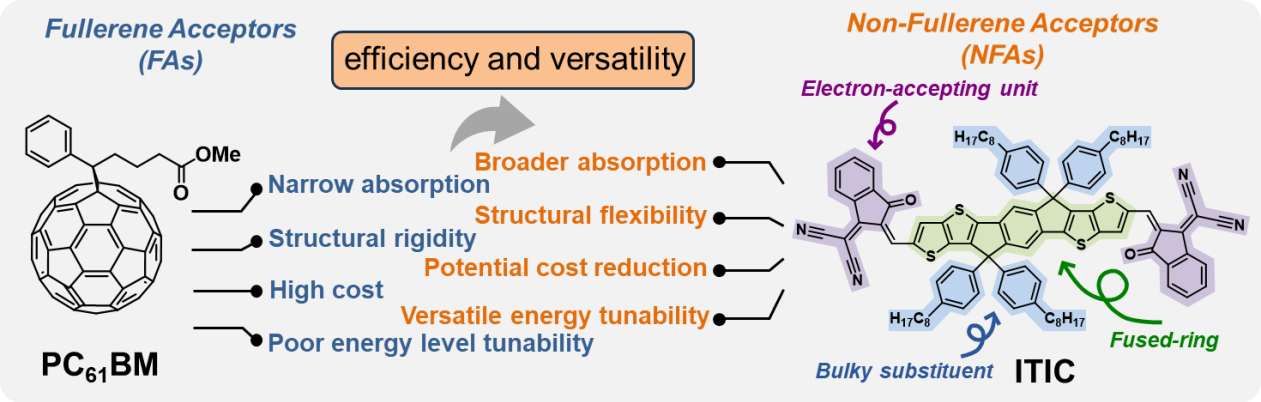

Figure 2. Representative skeletons of fullerene acceptors (FAs) and non-fullerene acceptors (NFAs).

In 2015, Zhan et al. developed a new NFA, named ITIC.[19] ITIC (**Figure 2, right**) is a representative NFA that has gained significant attention in OSC research due to its outstanding optoelectronic properties and flexible molecular design. The molecular engineering strategies for the ITIC series include replacing terminal electron-accepting units to adjust energy levels and absorption properties, modifying electron-donating fused cores (indacenodithieno[3,2-*b*]thiophene, IDTT) to enhance conjugation and improve charge transport, and regulating bulky side chains to optimize molecular packing, solubility, and nanoscale phase separation in active layer.[20-22] This new system of acceptor molecules has greatly promoted the rapid improvement of the efficiency of organic solar cell devices. In just a few years, the efficiency has increased from the initial 6.8% to the current 20%.[23,24] Currently, significant attention in OSCs is directed toward the molecular design, synthesis, and device engineering of NFAs.[17] As research in this area advances, the ongoing discovery of novel materials and refinement of fabrication techniques is steadily pushing OSCs toward commercialization, highlighting their vast potential for practical applications.

According to the process from simple to complex device structure, organic solar cells can be divided into single-layer structure cells, double-layer structure cells, bulk heterostructure cells and stacked structure cells.[13] In single-layer structure cells, since the diffusion distance of excitons is much smaller than the thickness of the active layer, the excitons in the active layer are lost before they are diffused. In addition, the dissociation efficiency of excitons at the interface between the metal electrode and the active layer is also very low, so the short-circuit current of the device is very small and the device efficiency is very low. This device structure is no longer studied. Double-layer structure cells are generally composed of an active layer of donor and acceptor materials.[25] Although compared with single-layer structure cells, double-layer structure cells have many advantages and device efficiency is also improved, but double-layer structure cells do not solve the problem of a large number of excitons being lost before they are dissociated, and the thickness of the active layer cannot be too large, otherwise the excitons will also be lost during the transmission process. In bulk heterostructure cells, the donor and acceptor materials are mixed together, and many small contact surfaces can be formed between the two.[9] Excitons can be dissociated and transmitted at these contact surfaces, which greatly improves the utilization rate of excitons and the device efficiency is also improved. This device structure is currently the most widely studied. The stacked structure battery is to connect two or more bulk heterojunction batteries in series, and then add a buffer layer between the batteries to increase charge transfer.

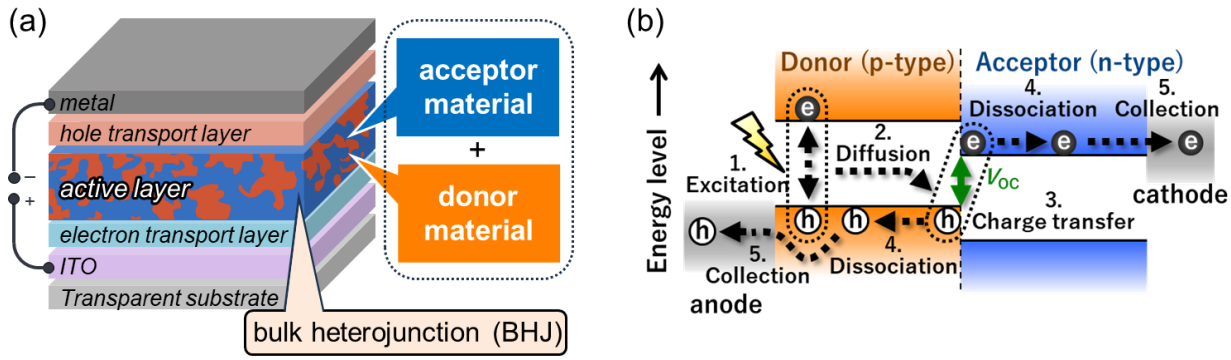

Figure 3. (a) Inverted configuration of OSCs. (b) Photon-to-current conversion process.

Bulk heterojunction photovoltaic cells with inverted structure are shown in **Figure 3a**. The inverted structure is to swap the cathode interface and anode interface in the upright device, from bottom to top, it is ITO glass, cathode interface (generally ZnO, TiO_x, etc.), active layer, anode interface (MoO_3, V_2O_5, etc.), metal anode (Ag, Au, etc.).

As shown in **Figure 3b**, the photon-to-current conversion process in a BHJ structure involves several main steps:[26]

(1) Generation of excitons.

After the active layer (donor or acceptor) absorbs photons, the electrons are stimulated to emit and jump from the HOMO to the LUMO, while the holes remain on the HOMO. The pair of holes and electrons generated under the Coulomb force is called excitons.

(2) Diffusion of excitons.

The generated excitons need to diffuse to the donor-acceptor interface before they can be used. The diffusion distance of excitons in organic materials is about 10-20 nm. Therefore, optimizing the active layer so that the donor-acceptor forms an interpenetrating network structure is very beneficial for the diffusion of excitons.

(3) Dissociation of excitons.

When the excitons diffuse to the donor-acceptor interface, under the action of the built-in electric field, that is, the HOMO and LUMO energy level difference between the donor and the acceptor, the excitons are split into free electrons and holes.

(4) Carrier transport

Under the action of the built-in electric field, free carriers will be transported to the corresponding electrodes. When the active layer morphology, that is, the donor and the acceptor are over-aggregated or the phase separation is not good, the carriers will recombine and be lost during the transport process. In addition, the transmission rate of electrons and holes affects the mobility of the active layer. Generally, a more balanced electron and hole mobility is one of the factors to improve device performance.

(5) Charge collection.

The free electrons and holes are separated and transferred in the acceptor and donor respectively, and finally collected by the cathode and anode to form current. It is worth noting that in order to extract free charges to the greatest extent, the potential barrier between the electrode and the active layer should be as low as possible to form good ohmic contact.

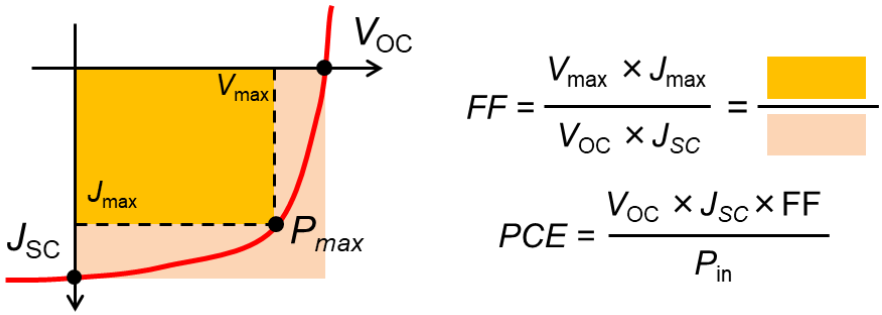

Figure 4. Current density-voltage characteristic curve of OSCs.

Figure 4 shows the *J-V* characteristic curve of OSCs. The intersection of the curve and the ordinate is the short-circuit current (J_{SC}), which indicates the maximum output current of the photovoltaic device when the applied

voltage is zero. The intersection of the curve and the ordinate is the open-circuit voltage (V_{OC}), which indicates the maximum voltage value that the device can output, and is related to the HOMO and LUMO level of the donor and acceptor. The fill factor (FF) is defined as the ratio of the maximum output power of the device ($V_{max} \times J_{max}$) to the product of V_{OC} and J_{SC} ($V_{OC} \times J_{SC}$). This parameter is closely related to the morphology of the active layer and the carrier mobility. The photoelectric conversion efficiency (PCE) is the ratio of the product of V_{OC}, J_{SC}, and FF to the incident light power. From the above, it can be seen that the final photovoltaic efficiency is mainly related to V_{OC}, J_{SC}, and FF. The following mainly discusses the factors affecting the photoelectric conversion efficiency from four aspects:[27]

1. Absorption and utilization of the solar spectrum by the active layer.

The first step of exciton generation requires the absorption of photons, so the number of absorbed photons directly affects the number of excitons generated. The stronger the ability of the active layer in organic photovoltaic cells to capture sunlight, that is, the larger the molar absorption coefficient, the more conducive it is to absorb more photons. In addition, the narrower the band gap of the compound, the wider the absorption spectrum range, which will also increase the number of photons absorbed. Generally, planar, D-A structured molecules are designed to increase intramolecular charge transfer and reduce the band gap, thereby enhancing light absorption.[28]

2. Carrier mobility.

As mentioned above, the size of carrier mobility and the balance of carrier mobility have an important influence on the final J_{SC} and FF of the device. There are many factors that affect carrier mobility, such as improving the regularity of the molecular plane, enhancing the size of the intermolecular force, and introducing specific groups, which can increase the carrier mobility.[29]

3. Energy level matching.

Designing a reasonable donor-acceptor energy level is crucial to improving the V_{OC} of the device. The energy level difference between the donor and the acceptor is greater than the binding energy of the exciton, so that the exciton can be effectively dissociated. Generally, the energy level difference between HOMO and LUMO needs to be greater than about 0.3 eV. Of course, there are many efficient devices now with an energy level difference less than this value, and the exciton can also be efficiently dissociated. Under the condition of ensuring sufficient driving force, increasing the energy level difference between the donor HOMO and the acceptor LUMO can increase the V_{OC} of the device, thereby improving the efficiency of the device.[30]

4. Micromorphology of the active layer.

The micromorphology of the active layer plays a very important role in the overall performance of the device. Generally speaking, the formation of a nano-interpenetrating network structure between the donor and the acceptor, and the active layer molecules present a face-to-face orientation (face on), the phase separation scale is small, and the phase purity is high, which is beneficial to the device. The device performance can be improved by optimizing the active layer morphology through device means such as adding appropriate additives, heat treatment, solvent vapor annealing, and ternary blending.[31]

Compared to inorganic solar cells, OSCs experience significant energy losses during the photo-current conversion process due to their lower dielectric constant, higher electron-phonon coupling coefficient, and larger exciton binding energy, which result in significant limitations in both PCE and stability. In addition, according to the above description, the BHJ structure is composed of a D/A mixture, and its performance is often affected by

multiple factors, and the microscopic mechanism is extremely complex. At present, BHJ still has the following main problems: phase separation issues, energy level matching challenges, complex D:A interactions and material optimization challenges, which further restrict the performance of OSCs. To address these challenges, this work designed novel NFAs for OSCs by modifying the central backbone and bulk substituents of the highly flexible, structurally modifiable, and high-performance ITIC molecular structure. By studying molecular perspectives such as structure and performance, molecular stacking and aggregation, along with performance perspectives like exciton binding energy and energy levels at the D/A interface, this study focus on clarifying the relationship between structure and performance in OSCs, providing important insights for the design of high-performance OSCs.

Development of a V-shaped ITIC-based NFA

In Chapter 1, a V-shaped ITIC-based NFA with C_{2v} symmetry possessing bulky substituents on the same side of the molecule was designed and synthesized to study the effect of molecular structure on the properties, exciton binding energy, and OSC characteristics. Characterization of the physical and chemical properties in solution and film states showed that the aggregation behavior of the molecules significantly affects the energy levels of the molecules. Molecular dynamics simulations and density functional theory (DFT) calculations revealed how different aggregation modes of the molecules affect the orbital energy levels of the aggregates and exciton binding energy, and thus affect the OSC performance such as open-circuit voltage (V_{OC}) and short-circuit current density (J_{SC}).

Development of a *meta*-linked isomer of ITIC

In Chapter 2, to further study the effect of molecular aggregation behavior on the performance of OSCs, a new W-type with C_{2v} symmetry was synthesized by changing the folding angle of the ITIC skeleton. Physical and chemical characterizations in solution and film state show how aggregation behavior impacts the energy levels of the molecule. Single crystal X-ray diffraction analyses and DFT calculations show that the H- and J-aggregations exhibited in the isomer significantly affect the energy levels of the molecules. In addition, in combination with time-resolved infrared (TR-IR) absorption spectroscopy, molecular dynamics simulations and time-dependent (TD) DFT calculations, the effects of different stacking on the excited states at the D/A interface and their correlation with the performance of OSCs were studied.

Development of Ladder-Type Fused p-Conjugated Units Bearing Spiro units for NFAs

In Chapter 3, novel ITIC-based NFAs with spiro-substituted bithiophene and biphenyl bulky substituents were designed and synthesized to investigate their influence on electronic structure and OSC performance. Theoretical calculations, supported by electrochemical and photophysical measurements, reveal that variations in frontier molecular orbital (FMO) distributions of these structures significantly impact the electron–hole separation, thereby affecting exciton binding energy. This chapter underscores the relationship between specific structural modifications in NFAs and their consequent effects on E_b, providing insights into molecular design strategies for organic semiconductors.

References

1 NREL, Best Research-Cell Efficiency Chart, National Renewable Energy Laboratory, 2025, https://www.nrel.gov/pv/cell-efficiency.html.

2 Sun Y. D., Wang L., Guo C. H., Xiao J. Y., Liu C. H., Chen C., Xia W. Y., Gan Z. R., Cheng J. C., Zhou J. P., Chen Z. H., Zhou J., Liu D., Wang T., Li W., *J. Am. Chem. Soc.* **2024**, *146*, 12011-12019.

3 Kallmann H., Pope M., *J. Chem. Phys.* **1959**, *30*, 585-586.

4 Tang C. W., *Appl. Phys. Lett.* **1986**, *48*, 183-185.

5 Sariciftci N. S., Smilowitz L., Heeger A. J., Wudl F., *Science* **1992**, *258*, 1474-1476.

6 Yu G., Gao J., Hummelen J. C., Wudl F., Heeger A. J., *Science* **1995**, *270*, 1789-1791.

7 Zhang G. Y., Zhao J. B., Chow P. C. Y., Jiang K., Zhang J. Q., Zhu Z. L., Zhang J., Huang F., Yan H., *Chem. Rev.* **2018**, *118*, 3447-3507.

8 Chen J. W., Cao Y., *Acc. Chem. Res.* **2009**, *42*, 1709-1718.

9 Scharber M. C., Sariciftci N. S., *Prog. Polym. Sci.* **2013**, *38*, 1929-1940.

10 Cheng P., Zhan X. W., *Chem. Soc. Rev.* **2016**, *45*, 2544-2582.

11 Cheng Y. J., Yang S. H., Hsu C. S., *Chem. Rev.* **2009**, *109*, 5868-5923.

12 Peumans P., Yakimov A., Forrest S. R., *J Appl Phys* **2003**, *93*, 3693-3723.

13 Hoppe H., Sariciftci N. S., *J. Mater. Res.* **2004**, *19*, 1924-1945.

14 Hu H. W., Chow P. C. Y., Zhang G. Y., Ma T. X., Liu J., Yang G. F., Yan H., *Acc. Chem. Res.* **2017**, *50*, 2519-2528.

15 Nielsen C. B., Holliday S., Chen H. Y., Cryer S. J., McCulloch I., *Acc. Chem. Res.* **2015**, *48*, 2803-2812.

16 Chatterjee S., Jinnai S., Ie Y., *J. Mater. Chem. A* **2021**, *9*, 18857-18886.

17 Lin Y. Z., Zhan X. W., *Mater. Horiz.* **2014**, *1*, 470-488.

18 Zhang G. C., Lin F. R., Qi F., Heumüller T., Distler A., Egelhaaf H. J., Li N., Chow P. C. Y., Brabec C. J., Jen A. K. Y., Yip H. L., *Chem. Rev.* **2022**, 14180-14274.

19 Lin Y. Z., Wang J. Y., Zhang Z. G., Bai H. T., Li Y. F., Zhu D. B., Zhan X. W., *Adv. Mater.* **2015**, *27*, 1170-1174.

20 Wang J. Y., Zhan X. W., *Acc. Chem. Res.* **2021**, *54*, 132-143.

21 Ge J. F., Xie L., Peng R. X., Ge Z. Y., *Adv. Mater.* **2023**, *35*, 2206566.

22 Cheng B., Xia X. X., Cheng S. X., Han C. Y., Sun F. B., Fu Z., Hou W. W., Hua F., Wang H., Sun W., Huo Y. M., Ji S. Q., Guo X., Yin H., Du X. Y., Hao X. T., Li Y. F., Zhang M. J., *Adv. Mater.* **2025**, *37*, 2500357.

23 Zhu L., Zhang M., Zhou G. Q., Wang Z. Y., Zhong W. K., Zhuang J. X., Zhou Z. C., Gao X. Y., Kan L. X., Hao B. N., Han F., Zeng R., Xue X. N., Xu S. J., Jing H., Xiao B., Zhu H. M., Zhang Y. M., Liu F., *Joule* **2024**, *8*, 3153-3168.

24 Li Y. F., Li H. J., Xu X. P., Yu L. Y., Li R. P., Peng Q., *Adv. Funct. Mater.* **2025**, 2424327.

25 Faure M. D. M., Lessard B. H., *J. Mater. Chem. C* **2021**, *9*, 14-40.

26 Ostroverkhova O., *Chem. Rev.* **2016**, *116*, 13279-13412.

27 Goetzberger A., Hebling C., Schock H. W., *Mat. Sci. Eng. R* **2003**, *40*, 1-46.

28 Günes S., Neugebauer H., Sariciftci N. S., *Chem. Rev.* **2007**, *107*, 1324-1338.

29 Gicevicius M., Gong H. X., Turetta N., Wood W., Volpi M., Geerts Y., Samorì P., Sirringhaus H., *Adv. Mater.* **2025**, *37*, 2418694.

30 Zhu L. Y., Wei Z. X., Yi Y. P., *J. Phys. Chem. C* **2022**, *126*, 14-21.

31 McDowell C., Abdelsamie M., Toney M. F., Bazan G. C., *Adv. Mater.* **2018**, *30*, 1707114.

Chapter 1 Development of a V-shaped ITIC-based NFA

1.1 Introduction

In OSCs, absorption of incident light by the active layer leads to the formation of excitons.[1] For these excitons to contribute to photocurrent, they must overcome Coulombic attraction and dissociate into free charge carriers—a process that requires overcoming the exciton binding energy (E_b).[2] Lowering E_b is crucial for reducing energy loss and suppressing charge recombination, thereby improving device efficiency. However, E_b is strongly dependent on factors such as molecular structure, intermolecular interactions, packing motifs, and D/A interfacial morphology, posing a major challenge in the development of high-performance OSCs.[3]

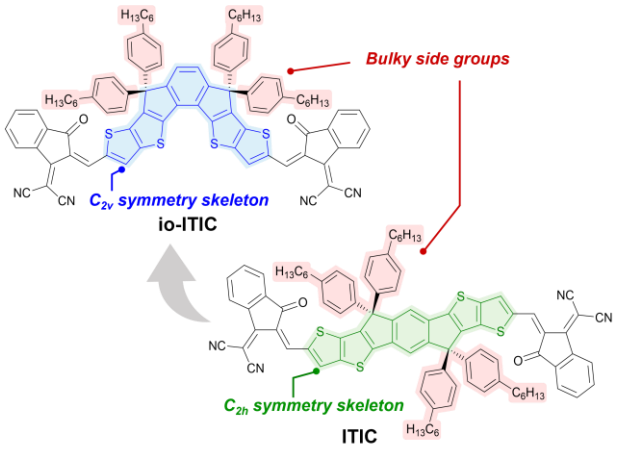

Figure 1.1. Molecular structures of **io-ITIC** and ITIC.

The E_b can be evaluated by **Eq. (1.1)**[4]:

$$E_b = \mathrm{IE} - \mathrm{EA} - E_g^{opt} \tag{1.1}$$

Where IE is the ionization energy, EA is the electron affinity and E_g^{opt} is the optical band gap. The ionization energy generally refers to the first ionization energy, which is the necessary energy to remove the least tightly bound electron from a molecule. The EA of a molecule is defined as the amount of energy released when an electron attaches to a molecule to form an anion. Therefore, in theory, EA and IE are highly related to the energy levels of the lowest unoccupied molecular orbital (LUMO) and the highest occupied molecular orbital (HOMO), respectively. The orbital energy levels of molecules are affected by multiple factors such as molecular structure, intermolecular interactions, solvent effects, and external electric fields. Herein, these factors can be used to adjust the molecular orbital, thereby affecting the EA and IE values, and ultimately changing the exciton binding energy of the molecule.

In this study, the symmetry of the ITIC molecular skeleton (C_{2h}) was modified and its bulk substituents were concentrated on the same side of the molecule to prepare a new NFA acceptor molecule with (C_{2v}) symmetry (**Figure 1.1**). Through detailed characterizations of the molecular physical and chemical properties combined with theoretical simulations, this study explains the influence of molecular structure and aggregation behavior on molecular energy levels, exciton binding energy, and the performance of organic solar cells.

1.2 Synthesis of compounds

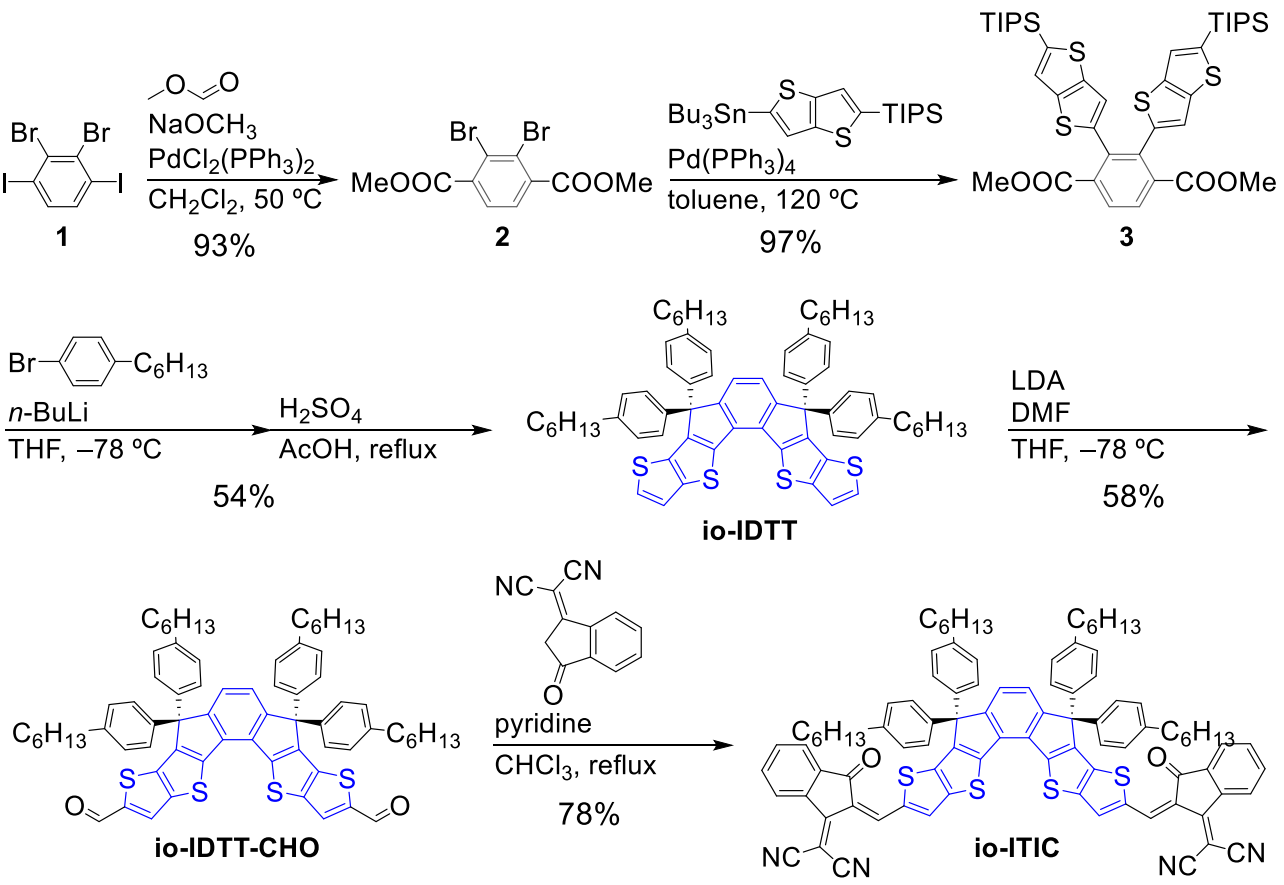

Scheme 1.1. Synthetic route to **io-ITIC**.

The synthetic pathway for **io-ITIC** is illustrated in **Scheme 1.1**. Compound 1 was synthesized according to a previously reported procedure.[5] A palladium-catalyzed alkoxycarbonylation of aryl halide 1 with methyl formate (HCOOMe) and sodium methoxide (NaOMe) was performed, affording compound 2 in a yield of 93%.[6] Note that in this synthesis, HCOOMe and NaOMe were added twice in total, with a yield of up to 93%, while the yield was only 60% when added once. Subsequently, compound 3 was obtained via a Stille coupling reaction in 97% yield. The intermediate io-IDTT was prepared through nucleophilic aryllithium addition followed by acid-mediated cyclization using H_2SO_4/AcOH, with an overall yield of 54% over two steps. Formylation of io-IDTT using the LDA/DMF system provided the aldehyde intermediate io-IDTT-CHO in 58% yield, while attempts using the Vilsmeier-Haack method with $POCl_3$ were unsuccessful. Finally, Knoevenagel condensation between io-IDTT-CHO and 1-(dicyanomethylene)-3-indanone (DCI) afforded the target compound **io-ITIC** with a yield of 78%.

The thermal properties of **io-ITIC** were assessed via thermogravimetric analysis (TGA). As shown in **Figure 1.2**, **io-ITIC** displays excellent thermal stability, with a decomposition temperature of 338 °C at 5% weight loss.

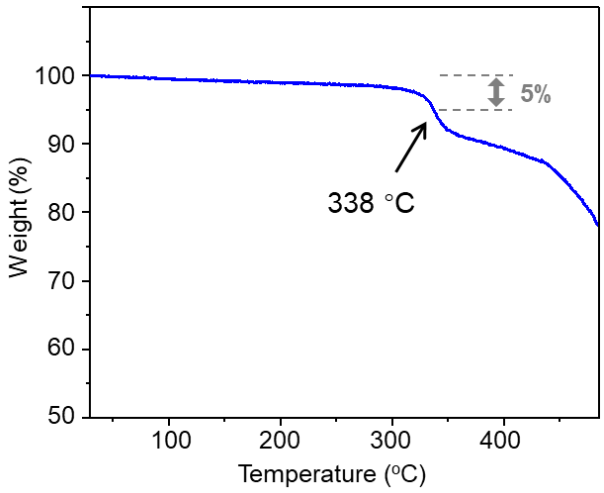

Figure 1.2. TGA profile of **io-ITIC**.

1.3 DFT investigation

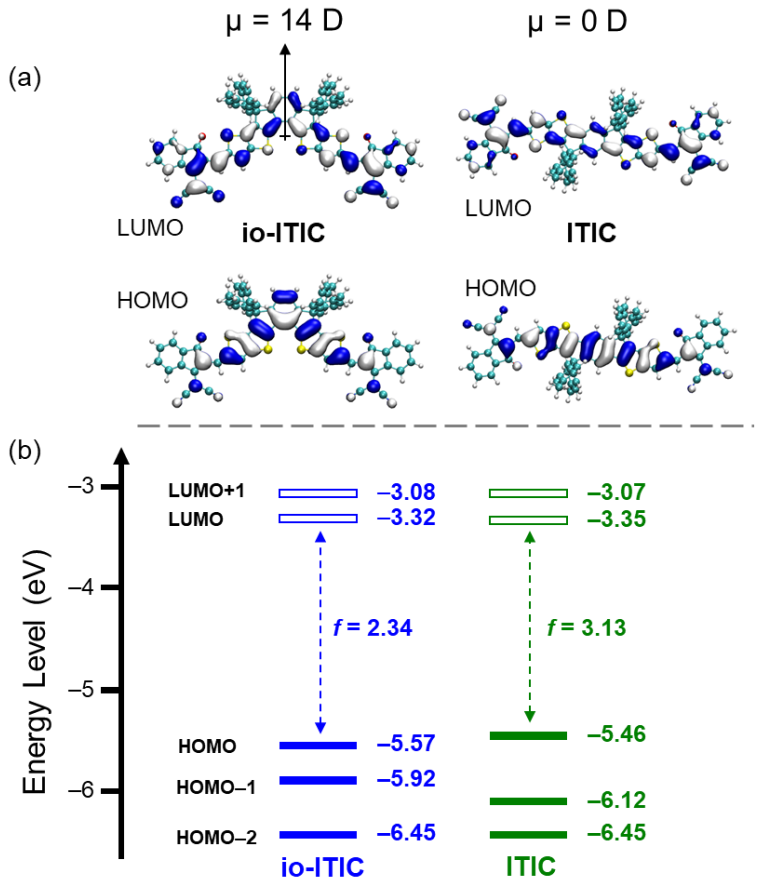

Figure 1.3. (a) Distribution of HOMO and LUMO. The dipole moments (μ) were also shown in the picture. (b) Energy level of molecular orbitals.

To assess the electronic structures of the target molecules, density functional theory (DFT) computations were carried out using the Gaussian 16 package with the B3LYP functional and 6-31G(d,p) basis set. The corresponding

frontier orbital energies, dipole moments (μ), and HOMO–LUMO distributions are presented in **Figure 1.3**. Due to the differences in molecular shape and symmetry caused by the isomerization of the molecular core, **io-ITIC** exhibits a large μ of 14 D compared to that of ITIC (0 D). It is generally believed that a larger μ of a molecule helps to increase the dielectric constant of the molecule, which is also helpful in improving the performance of organic solar cells. **Figure 1.3b** illustrates that upon transformation from C_{2h} to C_{2v} molecular symmetry, **io-ITIC** exhibits a lower HOMO energy of –5.57 eV, which is more stabilized than the –5.46 eV observed for ITIC. In parallel, the LUMO level becomes less stabilized, rising to –3.32 eV relative to that of ITIC. Simultaneously, the LUMO energy level shifts upward to –3.32 eV compared to ITIC. In addition, **io-ITIC** and ITIC have high similarity in the distribution of HOMO/LUMO, both concentrated on the indacenodithieno[3,2-*b*]thiophene (IDTT) core of the molecule. The oscillator strength (*f*) of the first excited state were found to be 2.34 and 3.13 for **io-ITIC** and ITIC, respectively.

1.4 Electrochemical and photophysical properties

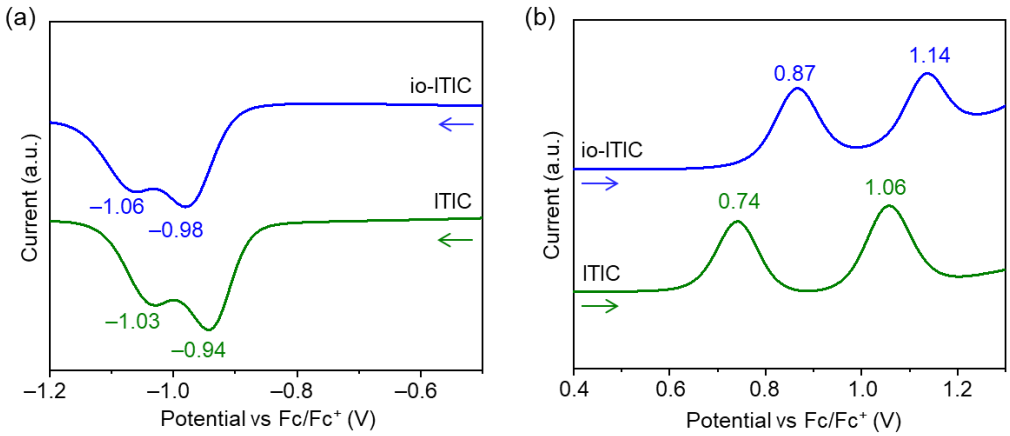

Figure 1.4. DPVs of **io-ITIC** and ITIC for (a) negative and (b) positive scans in *o*-DCB/acetonitrile (5:1) containing 0.1 M $TBAPF_6$.

Differential pulse voltammetry (DPV) was employed to determine the redox potentials of **io-ITIC** and ITIC in a binary solvent mixture of o-dichlorobenzene and acetonitrile (5:1, v/v), using 0.1 M tetrabutylammonium hexafluorophosphate ($TBAPF_6$) as the electrolyte. All potentials were referenced to the oxidation peak of ferrocene, which was used as an internal standard. As shown in **Figure 1.4a**, the reduction peaks of **io-ITIC** and ITIC showed similar patterns that their first reduction peak was found to be −0.98 V and −0.94 V, respectively. At the same time, as shown in **Figure 1.4b**, their oxidation wavelets showed a more obvious difference that their first oxidation peak variates from 0.87 V to 0.74 V for **io-ITIC** and ITIC, respectively. The HOMO and LUMO energy levels (E_{HOMO} and E_{LUMO}) were derived based on the onset potentials of the first oxidation and reduction peaks, respectively. These values were determined according to the equations provided below:

$$E_{HOMO} = -(E_{ox} + 4.80)\ \text{eV} \quad (1.2)$$

$$E_{LUMO} = -(E_{red} + 4.80)\ \text{eV} \quad (1.3)$$

The E_{HOMO}/E_{LUMO} of **io-ITIC** and ITIC were found to be −5.67 eV/−3.82 eV and −5.54 eV/−3.86 eV, respectively. The E_{HOMO} of **io-ITIC** was found to be 0.13 eV lower than that of ITIC in solution, and their E_{LUMO} showed a more closed level, which indicates that the core-isomerization obviously changed their oxidation behaviors. The electrochemical results were summarized in **Table 1.1**.

Table 1.1. Physical properties of **io-ITIC** and ITIC.

Compounds	λ_{max}^{sol} / nm[a]	λ_{max}^{film} / nm	λ_{onset}^{film} / nm	ε_{sol} / L mol^{-1} cm^{-1}	E_g^{opt} / eV[b]	E_{HOMO} / eV[c]	E_{LUMO} / eV[c]	IP / eV [d]	EA / eV[e]
io-ITIC	642	667	729	1.32×10^5	1.70	–5.67	–3.82	5.80	3.85
ITIC	679	697	765	1.76×10^5	1.62	–5.54	–3.86	5.85	3.87

[a] Obtained from a chloroform solution. [b] E_g^{opt} was estimated by the equation of 1240 / λ_{onset}^{film}. [c] Estimated by DPV. [d] Determined using PYS. [e] Determined using LEIPS.

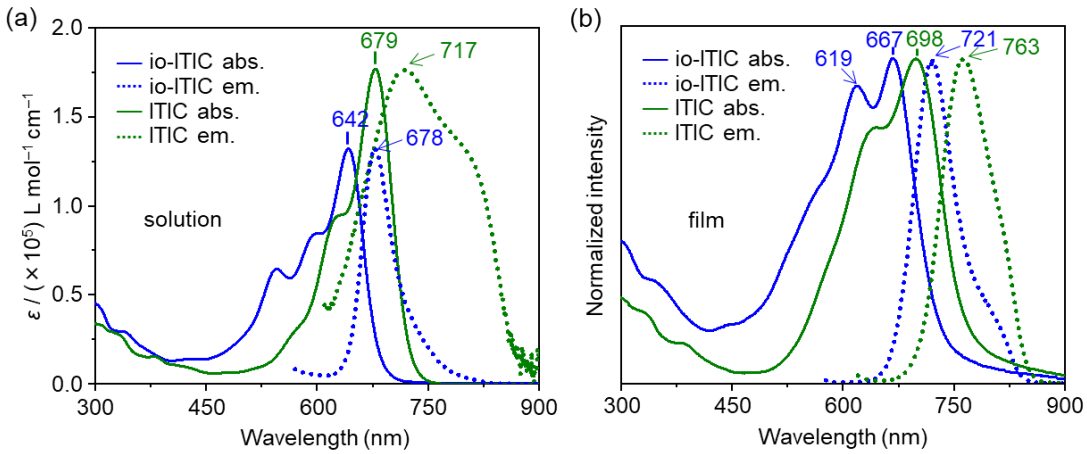

Figure 1.5. UV-vis absorption spectra (solid lines) and fluorescence spectra (dotted lines) of **io-ITIC** and ITIC in chloroform solutions (a) and films (b). Fluorescence spectra are unified to the same intensity as the absorption spectra for direct comparison.

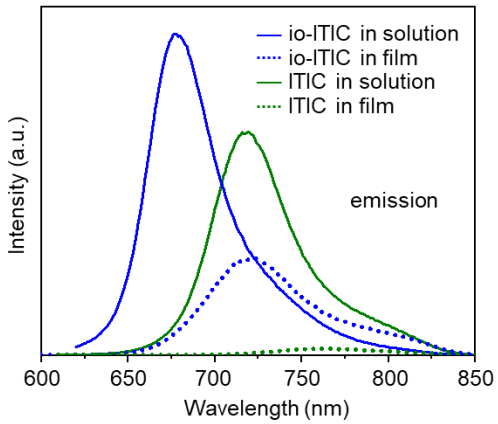

Figure 1.6. Fluorescence spectra of **io-ITIC** and ITIC in chloroform solutions and films.

The UV-vis absorption spectra and fluorescence spectra of **io-ITIC** and ITIC in chloroform solution and thin film state are shown in **Figure 1.5**. In the solution spectra, the absorption patterns of **io-ITIC** show an obvious blue-shift compared to ITIC, and their maximum absorption peaks (λ_{max}^{sol}) were found to be 642 and 679 nm, respectively. The molar absorption coefficient (ε_{sol}) in solution for **io-ITIC** and ITIC was estimated to be 1.32×10^5 and 1.76×10^5 L mol^{-1} cm^{-1}, respectively. The ε_{sol} is consistent with the DFT results (**Figure 1.3b**) that **io-ITIC** has a lower *f*.

In π-conjugated molecules, head-to-tail stacking, or J-aggregation, could red-shift the absorption spectrum and enhance emission intensity due to the super-radiance effect, driven by negative dipole coupling and exciton resonant in the lowest energy state.[7] The shift for the maximum absorption peak from solution to film for **io-ITIC** and ITIC were 25 and 19 nm, respectively. In addition, as shown in **Figure 1.6**, the highest emission intensity of **io-ITIC** is 1.4 times higher than that of ITIC in solution, but this value increases dramatically to 15 in the film state. The above results indicate that there exists a more obvious head-to-tail stacking tendency in **io-ITIC** molecules compared with ITIC. The optical energy gap (E_g^{opt}) based on the onset of the absorption spectra in film state was estimated to be 1.70 eV for **io-ITIC** and 1.62 eV for ITIC, which are summarized in **Table 1.1**.

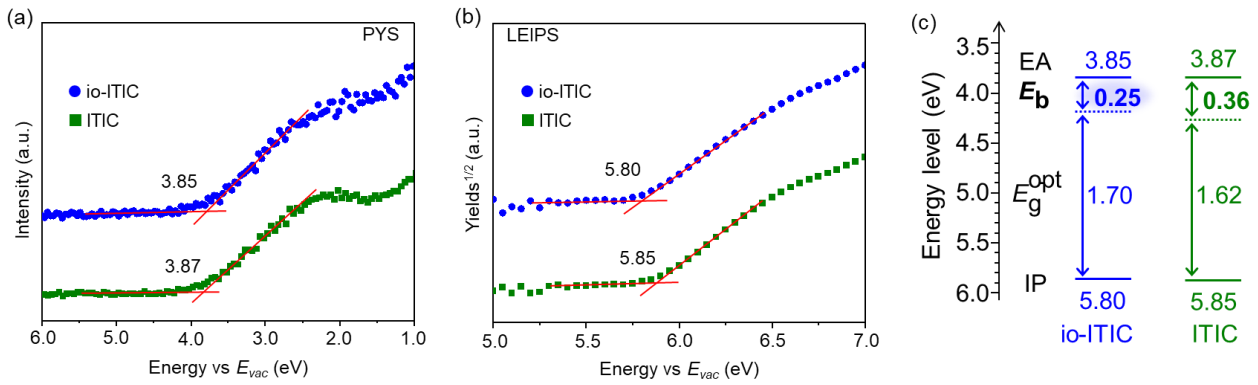

Figure 1.7. (a) LEIPS and (b) PYS of **io-ITIC** and ITIC in thin film state. (c) Energy level diagrams of **io-ITIC** and ITIC.

Low-energy inverse photoemission spectroscopy (LEIPS) and photoelectron yield spectroscopy (PYS)[8,9] were conducted to determine the EA and IE[10] of **io-ITIC** and ITIC. As shown in **Figure 1.7a**, **io-ITIC** and ITIC exhibit near EA values of 3.85 eV and 3.87 eV, respectively. Interestingly, as shown in **Figure 1.7b**, the IE values for **io-ITIC** and ITIC were determined to be 5.80 and 5.85 eV, respectively, which indicate an oppsite trend compared to the DPV results. It is considered that the IE values were affected by the intermolecular interaction difference.

Based on the EA, IE, and E_g^{opt} values, the E_b for **io-ITIC** and ITIC in film state were determined by **Eq. (1.1)**. As shown in **Figure 1.7c**, **io-ITIC** possesses a smaller E_b value of 0.25 eV compared with that of ITIC (0.36 eV). Compared with the energy level in the solution state, the IE value of **io-ITIC** in the solid state is increased, which contributes to a smallar exciton binding energy than that of ITIC. A lower exciton binding energy is crucial for effective charge separation in photocurrent conversion.

1.5 Single-crystal X-ray analysis

Single-crystal X-ray diffraction analysis was conducted to elucidate the molecular conformation and solid-state packing of **io-ITIC**. Suitable single crystals were obtained via vapor diffusion of methanol into a chloroform solution over the course of several weeks.

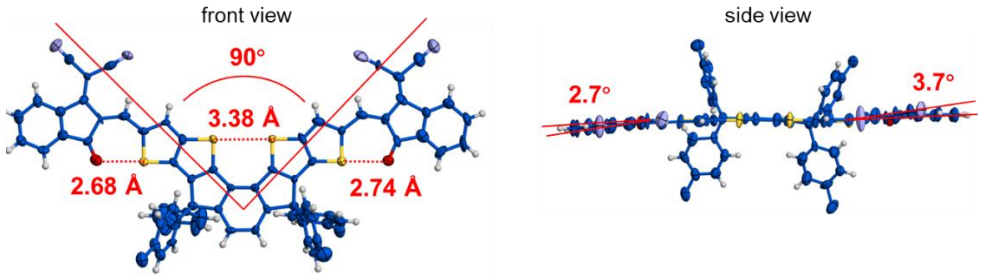

Figure 1.8. Front and side view representations of the **io-ITIC** molecular core, as obtained from single-crystal structure analysis. Side chains have been omitted or simplified to enhance structural clarity.

As shown in **Figure 1.8**, the molecular skeleton of **io-ITIC** adopts a V-shaped geometry with a folding angle of 90°. The distance of the S···O interaction was found to be 2.68 and 2.74 Å, and the distance of the S···S in the center was found to be 3.38 Å. From the side view, the **io-ITIC** molecule showed a generally planar structure with a distortion around 3° for the DCI unit.

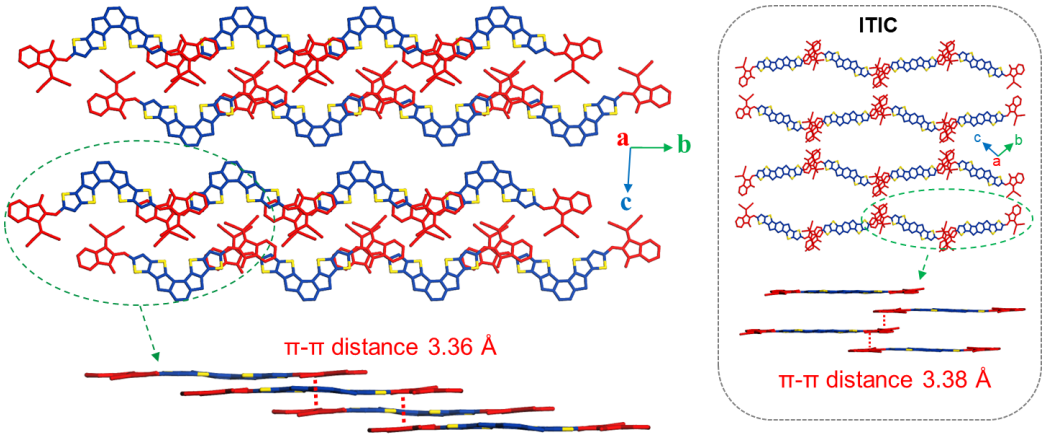

Figure 1.9. Top and side view illustrations of the single-crystal packing structures of **io-ITIC** (left) and ITIC (right). For visual clarity, side chains have been either removed or simplified. Key parameters for the crystal: $P\bar{1}$, GooF = 1.416, R_1 = 13.16%, wR_2 = 36.72%, data completeness = 77.5%. The structural data of ITIC were referenced from a previously reported source.[11]

As shown in **Figure 1.9**, the stacking mode of **io-ITIC** molecules is different from that of ITIC. The **io-ITIC** molecules are stacked through the end groups (red color), and the bulky side chain groups of the molecules are concentrated on the same side (the blank part in the middle). Overall, the **io-ITIC** molecules are stacked in a linear manner, which is highly consistent with the characteristics of the observed needle-like crystals. The ITIC molecules form a molecular stacking mode that is approximately two-dimensional through the end groups. In addition to stacking aggregation, there also exists an embedded aggregate between **io-ITIC** molecules.

1.6 Photovoltaic properties

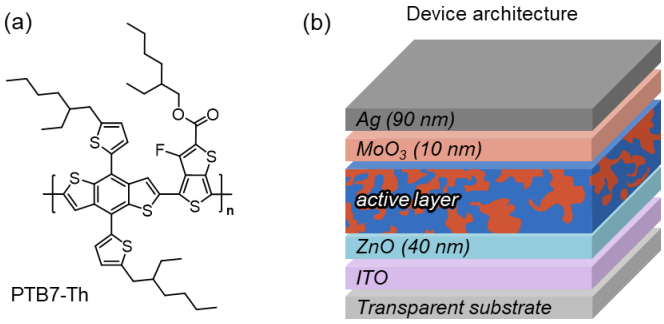

Figure 1.10. (a) Chemical structure of PTB7-Th. (b) Device architecture of OSCs.

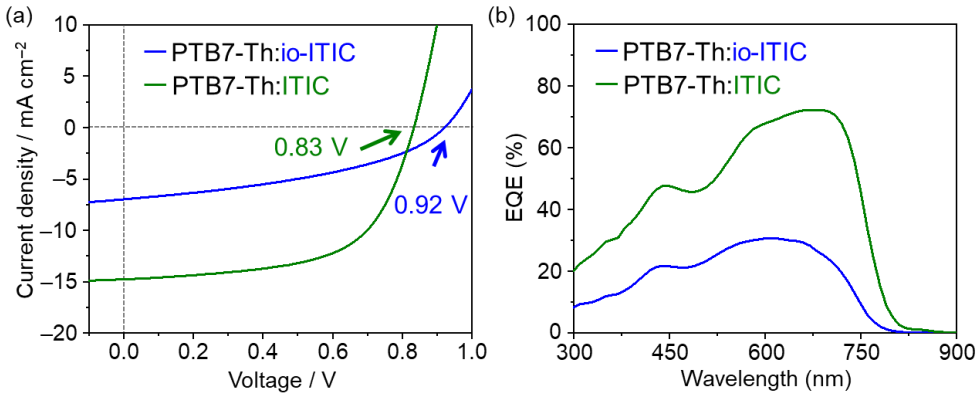

Figure 1.11. (a) *J*–*V* curves, and (b) EQE spectra of best performing PTB7-Th:**io-ITIC** and PTB7-Th:ITIC OSCs.

Table 1.2. OSC characteristics of **io-ITIC** and ITIC.

Compounds	PCE / %	J_{SC} / mA cm^{-2}	V_{OC} / V	FF / %	EQE_{max} / %
io-ITIC	2.62	6.99	0.92	41	30.7
ITIC	7.41	14.78	0.83	60	72.2

The photovoltaic performance of **io-ITIC** was assessed using an inverted device structure comprising ITO/ZnO/D:A/MoO_3/Ag, as illustrated in **Figure 1.10b**. The representative narrow-bandgap polymer PTB7-Th was employed as the donor material (**Figure 1.10a**). As shown in **Figure 1.11**, the PTB7-Th:**io-ITIC** blend film yielded a PCE of 2.62%, with a J_{SC} of 6.99 mA cm^{-2}, an V_{OC} of 0.92 V, and an FF of 0.41. The corresponding device parameters are summarized in **Table 1.2**. Although the PCE was lower than that of the PTB7-Th:ITIC-based devices—primarily due to the reduced J_{SC}—the V_{OC} of the **io-ITIC**-based device was notably higher (0.92 V vs. 0.83 V). While V_{OC} is generally correlated with the EA of the acceptor, the experimentally determined EA values of **io-ITIC** and ITIC were nearly identical (**Table 1.1**), suggesting that other factors—such as interfacial energetics or aggregation behavior—may contribute to the observed difference in V_{OC}.

To elucidate the origin of the V_{OC} difference, the CT state (E_{CT}) was estimated from the intersection of the electroluminescence (EL) and external quantum efficiency (EQE) spectra, as shown in **Figure 1.12**. The E_{CT} values for the **io-ITIC**- and ITIC-based devices were determined to be 1.71 eV and 1.65 eV, respectively, demonstrating a clear correlation with their corresponding V_{OC} values.[10]

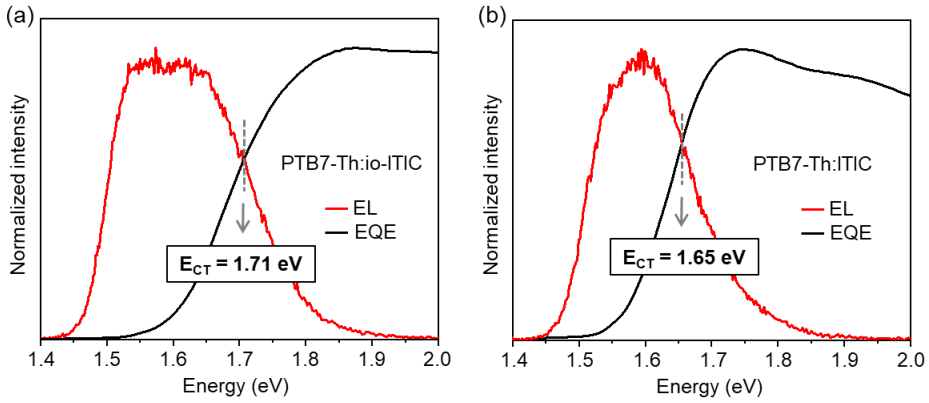

Figure 1.12. Normalized EQE and EL spectra for PTB7-Th:**io-ITIC** (a) and PTB7-Th:ITIC (b).

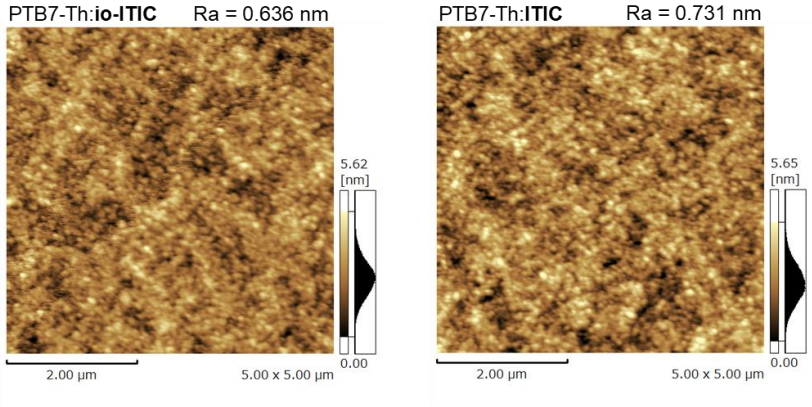

Figure 1.13. AFM height images of PTB7-Th:**io-ITIC** and PTB7-Th:ITIC blend films.

The surface morphologies of the blend films were investigated via atomic force microscopy (AFM). As shown in **Figure 1.13**, both films show very similar smooth surface morphologies with tiny nanostructures, and the average arithmetic roughness (Ra) were calculated to be 0.636 and 0.731 nm for PTB7-Th:**io-ITIC** and PTB7-Th:ITIC blend films, respectively.

1.7 Molecular dynamic (MD) simulation

To investigate the origins of the differences in exciton binding energy E_b and OSC performance between **io-ITIC** and ITIC, molecular dynamics (MD) simulations were conducted.[12-14] Representative simulation snapshots and examples of stacking configurations for both molecules are shown in **Figure 1.14**. Notably, **io-ITIC** displays a broader variety of aggregation modes compared to ITIC. In addition to the typical head-to-tail stacking, **io-ITIC** exhibits distinctive full head-tail alignment as well as embedded-type aggregation structures.

To better inspect their stacking difference, the radial distribution functions (RDFs) that normally indicates the likelihood of locating one group at a certain distance from a reference group, where a more pronounced g(r) peak corresponds to increased molecular packing density at that specific separation, were analyzed for the pristine system.[15] As shown in **Figure 1.15a**, the average distance of full head-tail stacking for **io-ITIC** is 3.7 Å, which is the π-π stacking distance. Additionally, in **Figure 1.15b**, the distance between the DCI groups and the H and S atoms near the molecular center is 2.9 Å, indicating strong intermolecular interactions between the DCI groups and the molecular center in the embedded aggregation of **io-ITIC**. In **Figure 1.15c**, the distance between the DCI groups in **io-ITIC** and ITIC is almost identical, suggesting very similar end-group stacking configurations in both molecules, which contains both full head-tail stacking and head-to-tail stacking. This variation in stacking patterns can significantly impact the solid-state performance of the molecules.

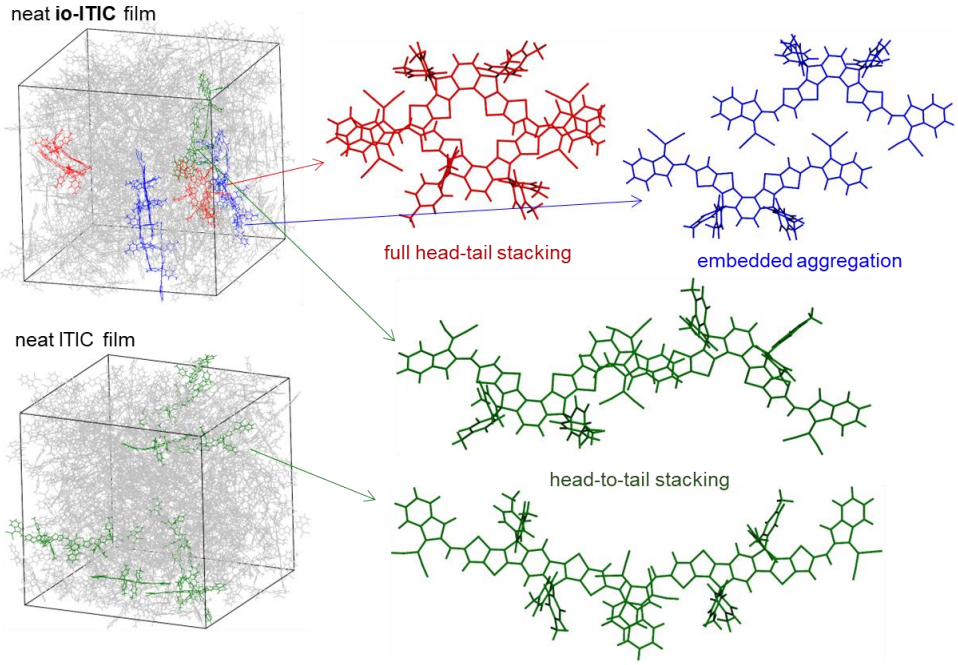

Figure 1.14. Molecular-dynamics (MD) simulations of **io-ITIC** and ITIC in pristine film state. Left: snapshots of the system; Right: examples of stacking mode.

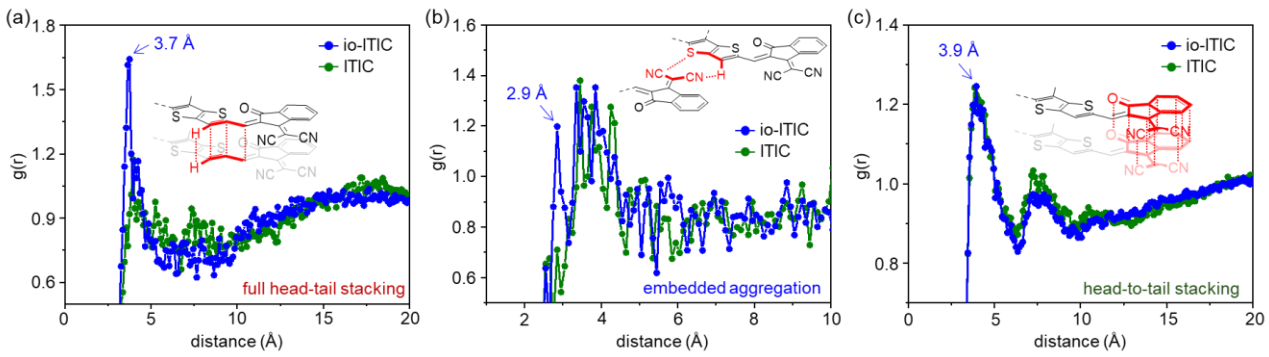

Figure 1.15. (a), (b) and (c) Radial distribution function data for full head-tail stacking, embedded stacking, and head-to-tail stacking, respectively. The red portion of the embedded structure view indicates the average distance to be considered.

To clearly elucidate the impact of stacking on molecular electronic structure, the energy levels of different aggregation modes based on MD results were calculated. While electrostatic interactions have been previously analyzed through DFT calculations,[15] additional factors—such as transition dipole moments and polarization energies—must also be considered to more comprehensively evaluate the impact of intermolecular interactions on energy level modulation.[16] As shown in **Figure 1.16**, the dimer energy level of the **io-ITIC** shows a marked difference than ITIC compared to their monomer. Specifically, the HOMO energy level varies notably across different stacking configurations, with the HOMO of the embedded dimer even higher than that of the ITIC dimer. This disparity of **io-ITIC** explains the origin of the higher ionization energy than ITIC in film state. The significantly increased HOMO energy level of embedded aggregation for **io-ITIC** may be related to the stronger interaction between molecules, which also increases the HOMO-LUMO interactions.[16] On the other hand, the increased variability in energy levels may lead to a broader density of states (DOS) in **io-ITIC**, as shown in **Figure 1.17**. This broadened DOS can enhance energetic disorder, potentially resulting in increased charge recombination and hindered charge transport, which collectively contribute to the reduced short-circuit current density J_{SC} observed in **io-ITIC**-based OSCs.

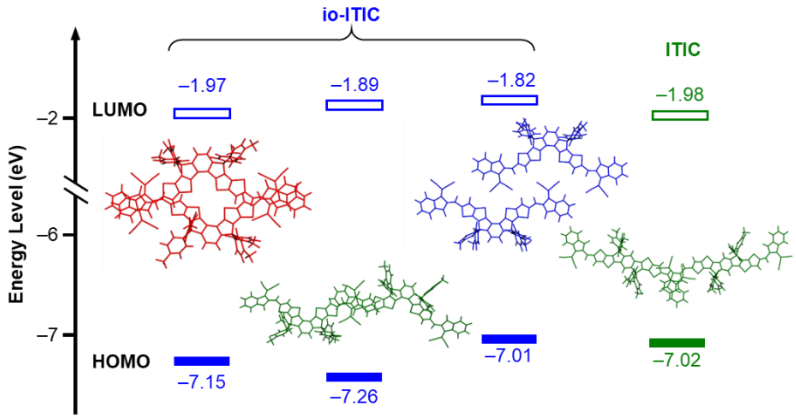

Figure 1.16. Schematic representation of electronic energy levels for monomeric and dimeric molecular models.

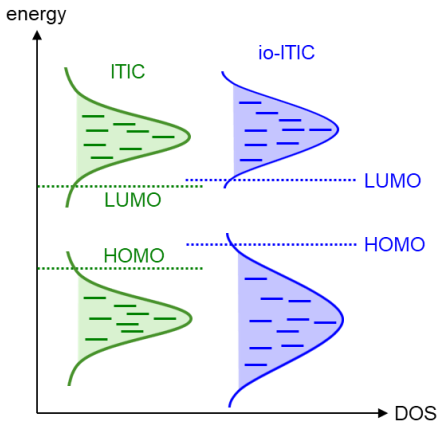

Figure 1.17. DOS distributions of ITIC and **io-ITIC**.

1.8 Conclusion

In summary, a novel ITIC isomer, **io-ITIC**, was designed and synthesized to explore the relationship between molecular structure, E_b, and device performance in OSC. DPVs in solution revealed that **io-ITIC** possesses a deeper HOMO energy level compared to ITIC. However, in the solid state, the IE of **io-ITIC** was 0.05 eV higher than that of ITIC. Based on the E_g^{opt}, IE, and EA values, **io-ITIC** exhibited a reduced E_b relative to ITIC. Despite achieving a higher V_{OC} in device applications, **io-ITIC**-based OSCs showed only moderate PCE, primarily due to limited J_{SC} and FF. MD simulations suggested that the V-shaped backbone of **io-ITIC** promotes diverse stacking arrangements, which may contribute to the modulation of HOMO energy levels and the reduction of E_b. This work highlights the role of asymmetric molecular design in tuning intermolecular packing and electronic properties, offering valuable guidance for the development of next-generation high-efficiency non-fullerene acceptors.

1.9 Experimental Section

General Information

^{1}H and ^{13}C NMR spectra were measured using a JEOL ECS-400 spectrometer. Chemical shifts (δ) are given in ppm, with signal multiplicities noted as s (singlet), d (doublet), t (triplet), m (multiplet), or br (broad), and coupling constants reported in Hz. High-resolution mass spectra (HRMS) were acquired via atmospheric pressure chemical ionization (APCI) on a Thermo Scientific LTQ Orbitrap XL. TGA analysis was carried out under nitrogen atmosphere at a heating rate of 10 °C min^{-1} using a Shimadzu TGA-50. UV-vis spectra were obtained using a Shimadzu UV-3600 spectrophotometer. Emission spectra were recorded with a Fluoromax-4 spectrometer operating in photon-counting mode and equipped with a Hamamatsu R928P detector. DPV measurements were performed on a BAS CV-620C using a platinum disk working electrode, platinum wire counter electrode, and $Ag/AgNO_3$ reference electrode at a scan rate of 100 mV s^{-1}. All measurements were conducted in spectroscopic-grade solvents. PYS was conducted using a Bunkoukeiki BIP-KV202GD system. LEIPS data were collected on an Ulvac-Phi system. Elemental analysis was conducted using a Perkin Elmer LS-50B by the Comprehensive Analysis Center (CAC), SANKEN, The University of Osaka.

OSC device fabrication and evaluation

OSCs were fabricated with the device structure ITO/ZnO/active layer/MoO_3/Ag. ITO-coated glass substrates were cleaned sequentially by ultrasonication in acetone, deionized water, and 2-propanol for 15 minutes each, followed by ozone treatment for 1.5 hours. A ZnO layer was deposited by spin-coating a precursor solution of zinc acetate dihydrate (200 mg), ethanolamine (55 μL), and 2-methoxyethanol (2 mL) at 4000 rpm, followed by thermal annealing at 200 °C for 30 minutes in air. The active layer was spin-coated onto the ITO/ZnO substrates inside a nitrogen-filled glove box. MoO_3 (10 nm) and Ag (100 nm) top electrodes were thermally evaporated through a shadow mask under a vacuum of 10^{-5} Pa, defining an active area of 0.09 cm^2. After encapsulation, the photovoltaic performance was measured in air under simulated AM 1.5G illumination (100 mW cm^{-2}) using a solar simulator (SAN-EI ELECTRIC, XES-301S). *J-V* characteristics were recorded with a KEITHLEY 2400 source meter. External quantum efficiency (EQE) spectra were acquired using a Soma Optics S-9240 system. Film thicknesses of active layers were measured by a KLA Tencor Alpha-step IQ profilometer.

Theological calculations

In the calculations, the alkyl chains in the acceptor molecules were replaced by methyl groups for simplification. In the calculation of the distribution of frontier molecular orbitals, structural optimization was calculated by density functional theory (DFT) calculations at B3LYP/6-31G(d,p). Calculations of the energy level for different packing modes were carried out at ωB97XD/6-31G(d,p) level.

Molecular-dynamics (MD) simulations

The MD simulations were carried out with the software package of Gromacs 2024.2 based on the general AMBER force field (GAFF) with the RESP charges.[17-20] The Berendsen method was applied for the control of pressure, and the velocity rescaling method with a stochastic term (v-rescale) was applied for the control of temperature. All covalent hydrogen bonds were constrained using the LINCS algorithm and a cutoff range for the short-range electrostatics was set to 13 Å. For **io-ITIC** and ITIC, the molecular geometry was optimized at B3LYP/6-31 G(d,p) level. For pristine systems, the initial cell was built by randomly placing 200 molecules of **io-ITIC** or ITIC in a 20 × 20 × 20 nm^3 cubic box to generate an initial geometry. The simulation was carried out using the following procedure: (1) 5 ns of simulation at 800 K and 100 bar to make molecules close together quickly; (2) 10 ns of simulation at 800 K and 1 bar, then cooling down to 300 K in 5 ns; (3) 20 ns of equilibration at 300 K and 1 bar for production.[13]

Preparation of materials

All starting materials, including ITIC, were sourced from commercial suppliers and utilized without additional purification. Reactions were conducted under an inert nitrogen atmosphere unless otherwise noted. The synthesis of compound 1 followed previously published methods.[5]

Synthetic procedures and characterizations

Synthesis of dimethyl 2,3-dibromoterephthalate (**2**): Compound 1 (1.0 g, 2.1 mmol), methyl formate (333 mg, 5.5 mmol), $PdCl_2(PPh_3)_2$ (70 mg, 0.1 mmol), and sodium methoxide (277 mg, 5.13 mmol) were dissolved in 30 mL of dichloromethane under inert atmosphere. The mixture was heated to reflux and stirred for 2 h. After cooling to room temperature, another batch of methyl formate (333 mg, 5.5 mmol) and sodium methoxide (277 mg, 5.13 mmol) were added soon. The mixture was again heated to reflux and stirred for another 2 h. After the reaction, the system was allowed to cool to room temperature and wash with water, then the organic phase was concentrated under reduced pressure. The crude product was purified by column chromatography on silica gel using *n*-hexane/ethyl acetate (4/1, v/v) as eluent, yielding compound **2** as a light-yellow solid (672 mg, 93%). ^{1}H NMR (400 MHz, $CDCl_3$): δ (ppm) 7.56 (s, 2H), 3.95 (s, 6H). ^{13}C NMR (100 MHz, $CDCl_3$) *δ*: 166.40, 138.02, 128.31, 125.44, 53.15. HRMS (APCI) m/z calcd. for $C_{68}H_{75}S_4$ $[M + H]^+$: 352.8847; found: 352.8802. Elemental Anal. Calcd. for $C_{10}H_8Br_2O_4$: C 34.12, H 2.29, N 0.00; found: C 33.97, H 2.38, N 0.00.

Synthesis of dimethyl 2,3-bis(5-(triisopropylsilyl)thieno[3,2-b]thiophen-2-yl)terephthalate (**3**): Compound 2 (672 mg, 1.9 mmol), triisopropyl(5-(tributylstannyl)thieno[3,2-b]thiophen-2-yl)silane (2.8 g, 4.8 mmol), and $Pd(PPh_3)_4$ (110 mg, 0.1 mmol) were dissolved in 30 mL of toluene under inert atmosphere. The mixture was heated to 120 °C and stirred for 15 h. After the reaction, the system was allowed to cool to room temperature and was then concentrated under reduced pressure. The crude product was purified by column chromatography on silica gel using *n*-hexane/chloroform (1/2, v/v) as eluent, yielding compound **3** as a yellow solid (1.45 g, 97%). ^{1}H NMR (400 MHz, $CDCl_3$): δ (ppm) 7.76 (s, 2H), 7.20 (s, 2H), 6.98 (s, 2H), 3.64 (m, 4H), 1.37-1.30 (m, 6H), 1.09-1.07 (m, 36H).

Synthesis of **io-IDTT**: To a solution of 1-bromo-4-hexylbenzene (3.0 mL, 14.8 mmol) in THF (30 mL) at –78 °C, *n*-butyllithium solution (2.66 M in *n*-hexane, 5.5 mL, 14.8 mmol) was added dropwise and stirred for 1 h. The solution was kept at –78 °C, and a solution of compound **3** (1.4 g, 1.8 mmol) in THF (30 mL) was added dropwise. The mixture was slowly warmed up to room temperature and stirred for 16 h and then quenched by water. The solution was extracted by $CHCl_3$ and washed with water and brine. The organic phase was concentrated and purified by column chromatography on silica gel using *n*-hexane/$CHCl_3$/EtOAc (10/2/1, v/v/v) as an eluent to give a yellow oil. This compound was subjected immediately to a solution of 50 mL acetic acid with 1 mL of concentrated sulfuric acid, and reflux for 4 h. After reaction, the mixture was washed with water and extracted by $CHCl_3$. The organic phase was concentrated and purified by column chromatography on silica gel using *n*-hexane/$CHCl_3$ (4/1, v/v) as an eluent to give **io-IDTT** as a light-yellow solid (990 mg, 54%). ^{1}H NMR (400 MHz, $CDCl_3$): δ (ppm) 7.37-7.36 (d, *J* = 5.09 Hz, 2H), 7.32-7.31 (d, *J* = 5.32 Hz, 2H), 7.27 (s, 2H), 7.18-7.16 (d, *J* = 8.37 Hz, 8H), 7.06-7.04 (d, *J* = 8.22 Hz, 8H), 2.55-2.51 (m, 8H), 1.58-1.51 (m, 8H), 1.30-1.26 (m, 24H), 0.88-0.83 (m, 12H). ^{13}C NMR (100 MHz, $CDCl_3$) *δ*: 153.18, 146.63, 142.82, 141.73, 141.43, 140.54, 133.80, 129.70, 128.42, 128.16, 126.89, 123.33, 120.41, 63.08, 35.66, 31.78, 31.34, 29.23, 22.67, 14.17. HRMS (APCI) m/z calcd. for $C_{68}H_{75}S_4$ $[M + H]^+$: 1019.4746; found: 1019.4756 . Elemental Anal. calcd. for $C_{68}H_{74}S_4$: C 80.11, H 7.32, N 0.00; found: C 80.03, H 7.16, N 0.00.

Synthesis of ***io-IDTT-CHO***: **io-IDTT** (250 mg, 0.25 mmol) was placed in a two-necked flask and dissolved in THF (20 mL). Lithium diisopropylamide (4.9 mL, 1.0 M in THF/*n*-hexane) was added to the mixture at –78 °C. After stirring for 1 h at the temperature, *N*,*N*-dimethylformamide (0.8 mL, 10 mmol) was added. The mixture was gradually warmed up to room temperature and stirred for 8 h. The reaction was quenched by water and extracted by $CHCl_3$. After removal of the solvent under reduced pressure, the crude product was purified by column chromatography on silica gel using *n*-hexane/$CHCl_3$ (3/1, v/v) as an eluent to give **io-IDTT-CHO** as orange solid (154 mg, 58%). This compound was subjected immediately to the next reaction without further purification. ^{1}H NMR (400 MHz, $CDCl_3$): δ (ppm) 9.93 (s, 2H), 8.02 (s, 2H), 7.39 (s, 2H), 7.12-7.10 (d, *J* = 8.46 Hz, 8H), 7.06-7.04 (d, *J* = 8.36 Hz, 8H), 2.54-2.40 (m, 8H), 1.58-1.50 (m, 8H), 1.33-1.27 (m, 24H), 0.86-0.83 (t, *J* = 6.79 Hz, 12H).

Synthesis of ***io-ITIC***: Pyridine (0.5 mL) was added to the solution of **io-IDTT-CHO** (80 mg, 0.074 mmol) and 3-(dicyanomethylidene)indan-1-one (86 mg, 0.44 mmol) in $CHCl_3$ (15 mL) and the resulting mixture was stirred at 75 °C for 12 h. The reaction mixture was washed with water 3 times and the organic phase was concentrated. The crude product was purified by column chromatography on silica gel using *n*-hexane/$CHCl_3$ (1/1 to 1/2, v/v) as eluent, followed by further purification with reprecipitation using $CHCl_3$ and acetone to give **io-ITIC** as deep blue solid (80 mg, 78%). ^{1}H NMR (400 MHz, $CDCl_3$): δ (ppm) 8.90 (s, 2H), 8.70-8.68 (d, *J* = 7.85 Hz, 2H), 8.32 (s, 2H), 7.93-7.91 (d, *J* = 7.24 Hz, 2H), 7.79-7.71 (m, 4H), 7.41 (s, 2H), 7.19-7.18 (d, *J* = 6.89 Hz, 8H), 7.10-7.08 (d, *J* = 7.06 Hz, 8H), 2.55-2.51 (m, 8H), 1.59-1.56 (m, 8H), 1.34-1.25 (m, 24H), 0.85-0.82 (t, *J* = 7.20 Hz, 12H). ^{13}C NMR (100 MHz, $CDCl_3$) *δ*: 188.23, 160.37, 155.15, 150.46, 148.21, 146.80, 144.17, 142.49, 140.09, 139.89, 139.11, 138.41, 136.93, 135.33, 134.63, 130.05, 128.86, 127.99, 125.69, 125.43, 123.91, 123.11, 114.66, 114.58, 69.75, 63.33, 35.67, 31.78, 31.35, 29.25, 22.67, 14.17. HRMS (APCI) m/z calcd. for $C_{94}H_{83}N_4O_2S_4$ $[M]^+$: 1428.5425; found: 1428.5437. Elemental Anal. calcd. for $C_{94}H_{82}N_4O_2S_4$: C 79.07, H 5.79, N 3.92; found: C 78.68, H 5.88, N 4.01.

1.10 References

1 Zhu Y. F., Zhao F. W., Wang W., Li Y. W., Zhang S. M., Lin Y. Z., *Adv. Energy Sustainability Res.* **2022**, *3*, 2100184.

2 Hummer K., Puschnig P., Sagmeister S., Ambrosch-Draxl C., *Mod. Phys. Lett. B* **2006**, *20*, 261-280.

3 Kippelen B., Brédas J. L., *Energy Environ. Sci.* **2009**, *2*, 251-261.

4 Knupfer M., *Appl. Phys. A* **2003**, *77*, 623-626.

5 Katoono R., Arisawa K., *RSC Adv.* **2023**, *13*, 11712-11719.

6 Carpentier J. F., Castanet Y., Brocard J., Mortreux A., Petit F., *Tetrahedron Lett.* **1991**, *32*, 4705-4708.

7 Spano F. C., *Acc. Chem. Res.* **2010**, *43*, 429-439.

8 Yoshida H., *Chem. Phys. Lett.* **2012**, *539*, 180-185.

9 Yoshida H., *J. Electron. Spectrosc. Relat. Phenom.* **2015**, *204*, 116-124.

10 Yang J. P., Bussolotti F., Kera S., Ueno N., *J. Phys. D: Appl. Phys.* **2017**, *50*, 423002.

11 Aldrich T. J., Matta M., Zhu W. G., Swick S. M., Stern C. L., Schatz G. C., Facchetti A., Melkonyan F. S., Marks T. J., *J. Am. Chem. Soc.* **2019**, *141*, 3274-3287.

12 Ye L., Hu H. W., Ghasemi M., Wang T. H., Collins B. A., Kim J. H., Jiang K., Carpenter J. H., Li H., Li Z. K., McAfee T., Zhao J. B., Chen X. K., Lai J. L. Y., Ma T. X., Bredas J. L., Yan H., Ade H., *Nat. Mater.* **2018**, *17*, 253-260.

13 Li Y. K., Guo Y., Chen Z., Zhan L. L., He C. L., Bi Z. Z., Yao N. N., Li S. X., Zhou G. Q., Yi Y. P., Yang Y., Zhu H. M., Ma W., Gao F., Zhang F. L., Zuo L. J., Chen H. Z., *Energy Environ. Sci.* **2022**, *15*, 855-865.

14 Han G. C., Yi Y. P., *Acc. Chem. Res.* **2022**, *55*, 869-877.

15 Zhang G. C., Chen X. K., Xiao J. Y., Chow P. C. Y., Ren M. R., Kupgan G., Jiao X. C., Chan C. C. S., Du X. Y., Xia R. X., Chen Z. M., Yuan J., Zhang Y. Q., Zhang S. F., Liu Y. D., Zou Y. P., Yan H., Wong K. S., Coropceanu V., Li N., Brabec C. J., Bredas J. L., Yip H. L., Cao Y., *Nat. Commun.* **2020**, *11*, 3943.

16 Okazawa K., Tsuji Y., Yoshizawa K., *J. Phys. Chem. A* **2023**, *127*, 4780-4786.

17 Hess B., *Abstr. Pap. Am. Chem. Soc.* **2009**, *237*, 435-447.

18 Wang J. M., Wolf R. M., Caldwell J. W., Kollman P. A., Case D. A., *J. Comput. Chem.* **2004**, *25*, 1157-1174.

19 Bayly C. I., Cieplak P., Cornell W. D., Kollman P. A., *J. Phys. Chem.* **1993**, *97*, 10269-10280.

20 Lu T., Chen F. W., *J. Comput. Chem.* **2012**, *33*, 580-592.

Chapter 2 Development of a *meta*-linked isomer of ITIC

2.1 Introduction

The V_{OC} of OSCs is primarily correlated with the energy offset between the HOMO of the donor and the LUMO of the acceptor.[1,2] Proper energy offset between donor and acceptor is demanded to achieve efficient charge dissociation and form CT state at the D/A interface (**Scheme 2.1**). The CT state arises from the interaction between donor and acceptor molecules among the D/A interfaces, where during the excitation process, the electron resides in the acceptor while the hole remains in the donor.[1,3] Hence, the energy level of CT state (E_{CT}) is largely influenced by the energy levels at the D/A interface. However, due to the complexity and variability of the morphology at the D/A interface, strategies for controlling E_{CT} through the molecular design are not well understood.

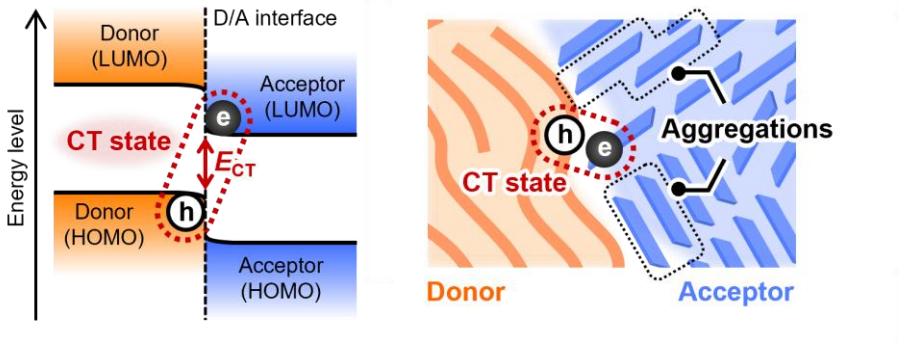

Scheme 2.1. Schematic diagram of energy states on the D/A interface.

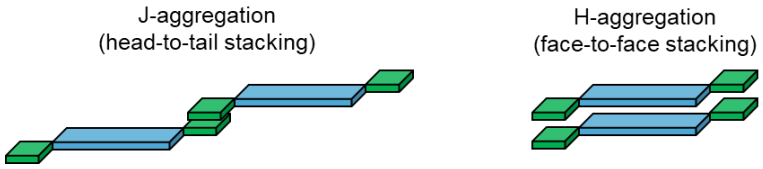

Figure 2.1. Schematic diagram of J-aggregation and H-aggregation.

The energy levels of organic semiconductors can be modulated by their aggregation behavior both in the solid phase and at D/A interface.[4] In particular, dimer-based models have demonstrated that these levels shift according to the nature of molecular packing, with notable differences observed between H-aggregates and J-aggregates.[5-8] J-aggregates are usually formed by the stacking of molecular end groups, usually without or rarely involving the molecular backbone. H-aggregates are usually formed by the stacking of molecular backbone centers, which is also called face-to-face stacking. **Figure 2.1** shows the schematic diagram of common J-aggregation and H-aggregation. However, for acceptor materials of OSCs, these molecules often have long and bulky side chains due to solubility considerations. Bulky side chains often hinder the effective face-to-face stacking between acceptor molecules, which is why commonly used acceptor materials, such as ITIC and Y6 (**Figure 2.2**), tend to adopt J-aggregation.

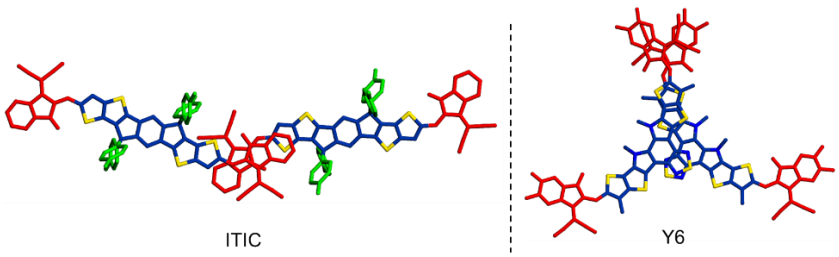

Figure 2.2. Different degrees of J-aggregation behavior in ITIC and Y6 crystal packing.

To explore how molecular aggregation influences the E_{CT} and V_{OC}, a novel isomer of ITIC with a W-shaped geometry, termed **im-ITIC**, was designed (**Figure 2.3**). While the classical ITIC molecule adopts a C_{2h}-symmetric structure characterized by bulky substituents flanking both sides of its fused polycyclic π-conjugated backbone, **im-ITIC** features a distinct C_{2v} symmetry, where the substituents are located only on one side of the backbone.[9] This structural variation is expected to alter the intermolecular packing behavior significantly, giving rise to different aggregation motifs in the solid phase. In this work, the effects of structural differences on molecular aggregation behavior were systematically investigated, and the correlations between the resulting molecular organization, the E_{CT} at the D/A interface, and the V_{OC} in OSCs were thoroughly analyzed.

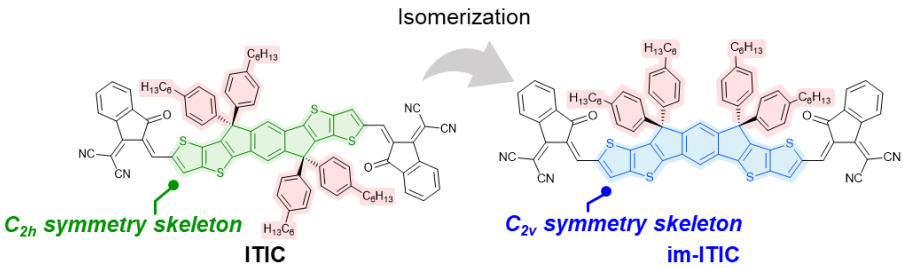

Figure 2.3. Molecular structures of **im-ITIC** and ITIC.

2.2 Synthesis of compounds

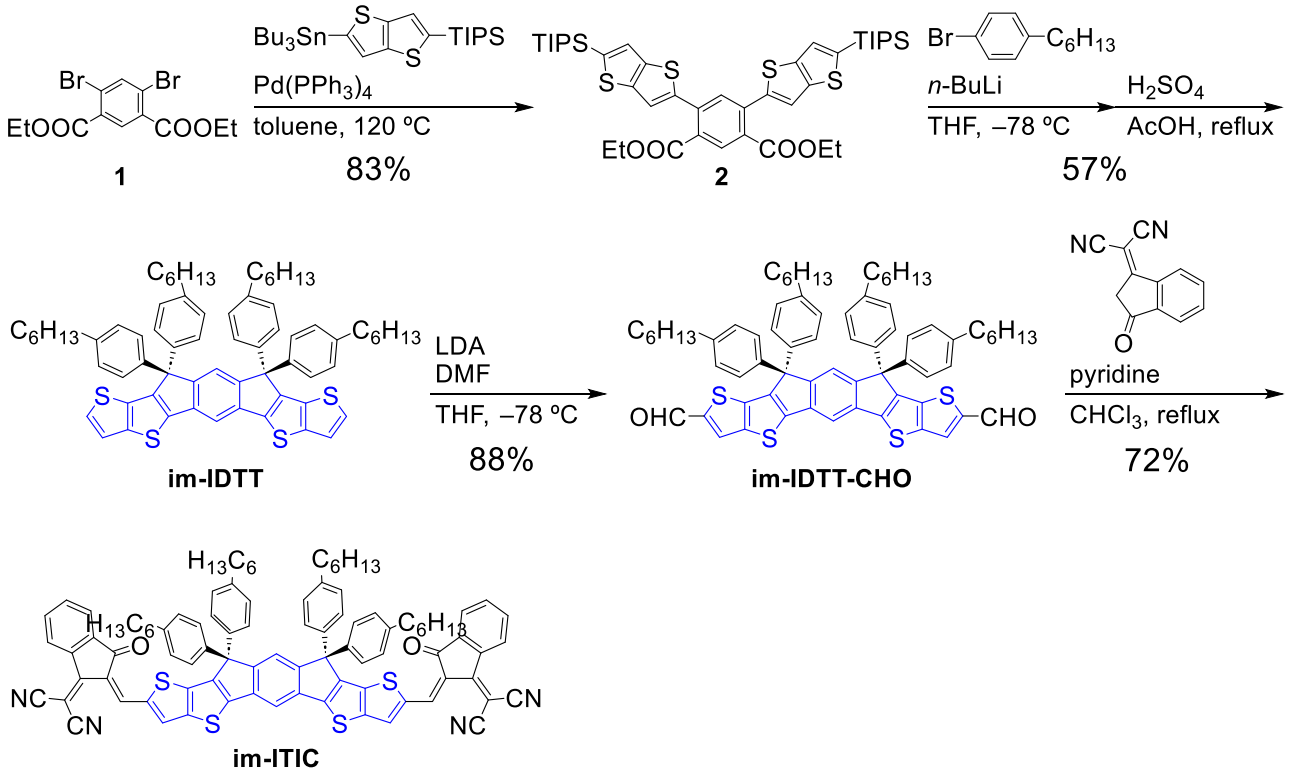

Scheme 2.2. Synthetic procedures for **im-ITIC**.

The synthetic procedure for **im-ITIC** is outlined in **Scheme 2.2**. Compound 1 was obtained using a previously established protocol.[10] Subsequently, a Stille coupling reaction was performed to generate compound 2 in a high yield of 83%. The intermediate im-IDTT was synthesized through a two-step sequence involving the nucleophilic addition of aryllithium, followed by intramolecular cyclization promoted by H_2SO_4/AcOH, yielding 57% overall. Formylation of im-IDTT using LDA and DMF furnished the aldehyde intermediate im-IDTT-CHO with an 88% yield. The final Knoevenagel condensation between im-IDTT-CHO and 1-(dicyanomethylene)-3-indanone (DCI) afforded the target molecule **im-ITIC** in a 72% yield.

Thermal stability of **im-ITIC** was evaluated by thermogravimetric analysis (TGA), as illustrated in **Figure 2.4**, A decomposition temperature of 342 °C at 5% weight loss was observed, indicating its excellent thermal robustness.

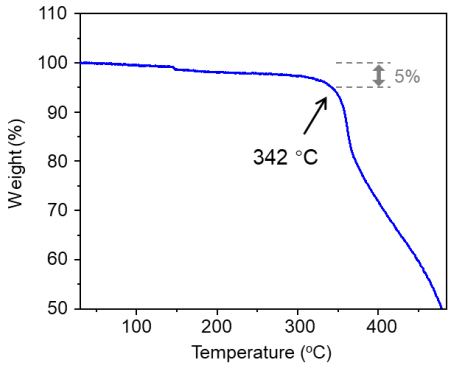

Figure 2.4. TGA profiles of **im-ITIC**.

2.3 Concentration-dependent ^{1}H NMR

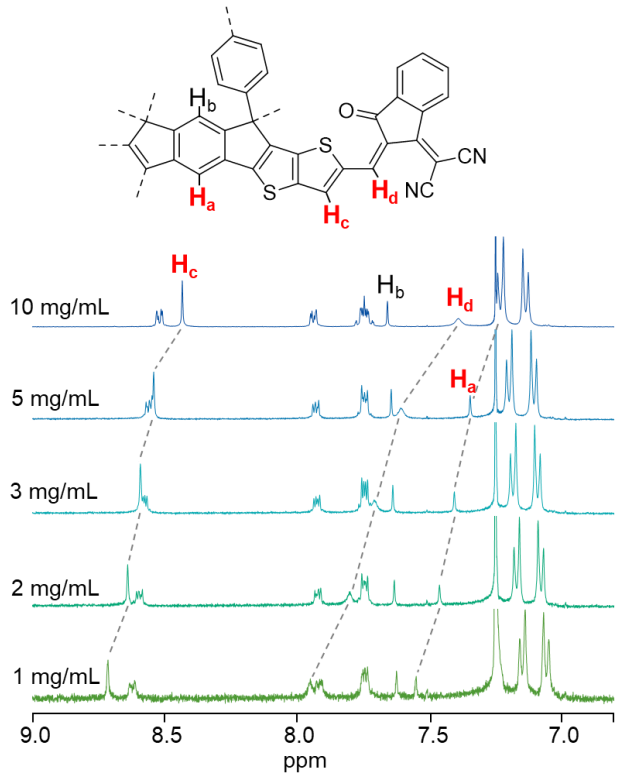

Figure 2.5. Concentration-dependent ^{1}H NMR spectra of aromatic region for **im-ITIC** in $CDCl_3$ at 20 °C. More concentration and the entire spectra are given in **Figure S2.2**.

To probe the aggregation behavior of **im-ITIC**, concentration-dependent ^{1}H NMR spectra were recorded in deuterated chloroform ($CDCl_3$), as presented in **Figure 2.5**. With increasing concentration, notable upfield shifts were observed for specific aromatic protons. In particular, H_a (central ring), H_c (thiophene unit), and H_d (vinyl group)—all positioned opposite to the bulky alkyl chains—exhibited significant chemical shift changes. In contrast, the H_b protons located on the same side as the alkyl substituents showed only minimal shifts. These findings suggest that molecular aggregation predominantly occurs on the side opposite the alkyl chains, indicating a distinct aggregation mode compared to the J-type aggregation typically observed in ITIC and other conventional NFAs (See **Figure S2.3**).

2.4 DFT investigation

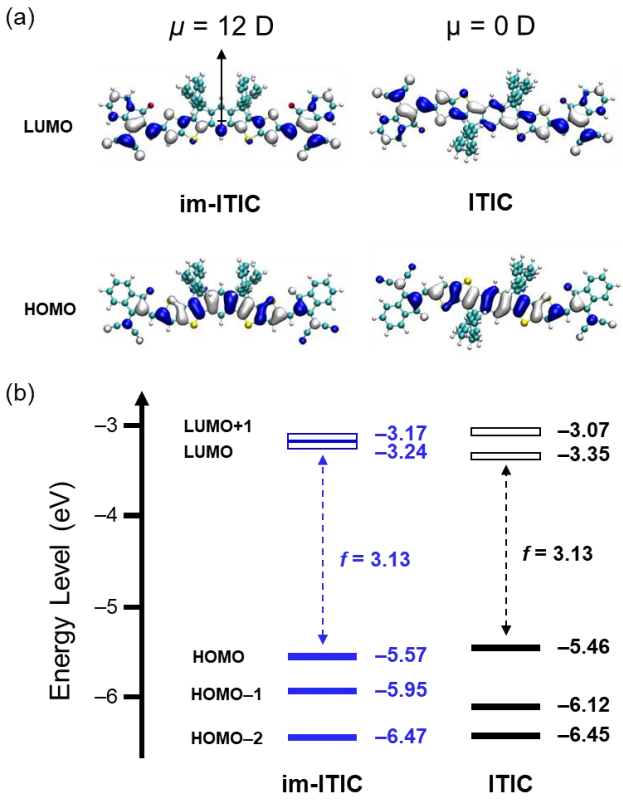

Figure 2.6. Distribution of HOMO and LUMO. The dipole moments (μ) were also shown in the picture. (b) Energy level of molecular orbitals.

Gaussian 16 software at B3LYP/6-31G(d,p) level was used for DFT calculations to evaluate the energy levels of those compounds. The HOMO/LUMO, dipole moments (μ) and energy levels of frontier molecular orbitals were shown in **Figure 2.6**. Similar to **io-ITIC** in Chapter 1, **im-ITIC** also shows a much larger molecular dipole moment than ITIC. In addition, **im-ITIC** and ITIC also have high similarity in the distribution of HOMO/LUMO. As shown in **Figure 2.6b,** with transferring from C_{2h} to C_{2v} symmetry, **im-ITIC** shows a deeper HOMO level of –5.57 eV which is the same to **io-ITIC** compared to that of –5.46 eV for ITIC. Simultaneously, the LUMO level shifts upward to –3.24 eV compared to **io-ITIC** (–3.32 eV) and ITIC (–3.35 eV). The oscillator strength (*f*) of first excited state keeps the same level as ITIC (3.13), which is higher that of **io-ITIC** (2.34). We can see that although **im-ITIC** and **io-ITIC** have the same symmetry, the structural differences bring significant differences to the electronic structures of the molecules.

2.5 Electrochemical and photophysical properties

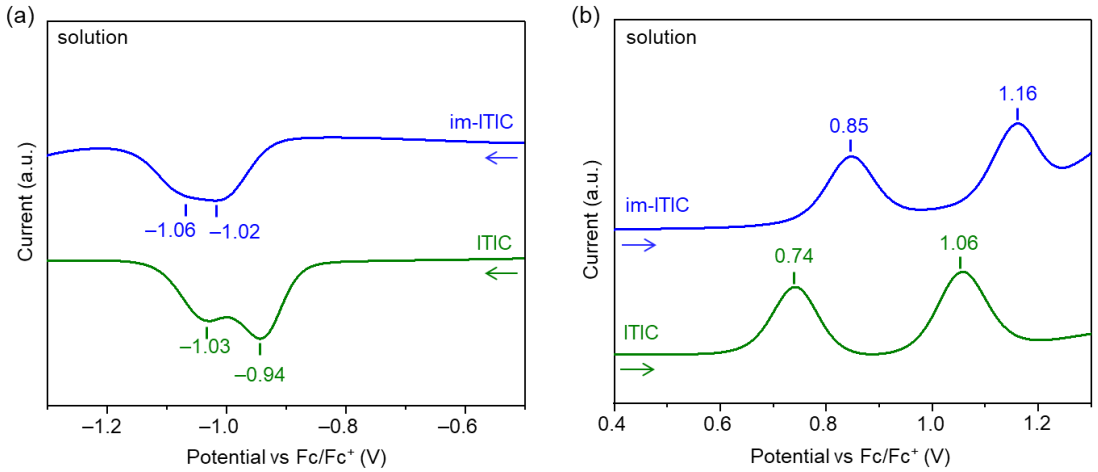

Figure 2.7. DPVs of **im-ITIC** and ITIC for (a) negative and (b) positive scans in *o*-DCB/acetonitrile (5:1) containing 0.1 M $TBAPF_6$.

The electrochemical properties of **im-ITIC** and ITIC were examined by DPV in a mixed solvent system of *o*-dichlorobenzene/CH_3CN (5/1) containing 0.1 M $TBAPF_6$. All potentials were referenced against the ferrocene/ferrocenium (Fc/Fc^+) redox couple as an internal standard. As illustrated in **Figure 2.7**, both compounds exhibited two distinct redox processes, corresponding to two-step reductions and oxidations in the cathodic and anodic scans, respectively. The first reduction potential (E_{red}) of **im-ITIC** was shifted negatively by 0.07 V compared to that of ITIC, while its first oxidation potential (E_{ox}) was 0.11 V more positive. A summary of the measured potentials is provided in **Table 2.1**. Using these electrochemical values, the estimated E_{LUMO} and E_{HOMO} energy levels were −5.65 eV and −3.79 eV for **im-ITIC**, and −5.54 eV and −3.86 eV for ITIC, respectively. These energy level estimations derived from DPV measurements show qualitative agreement with the DFT-predicted frontier orbital energies presented in **Figure 2.6**.

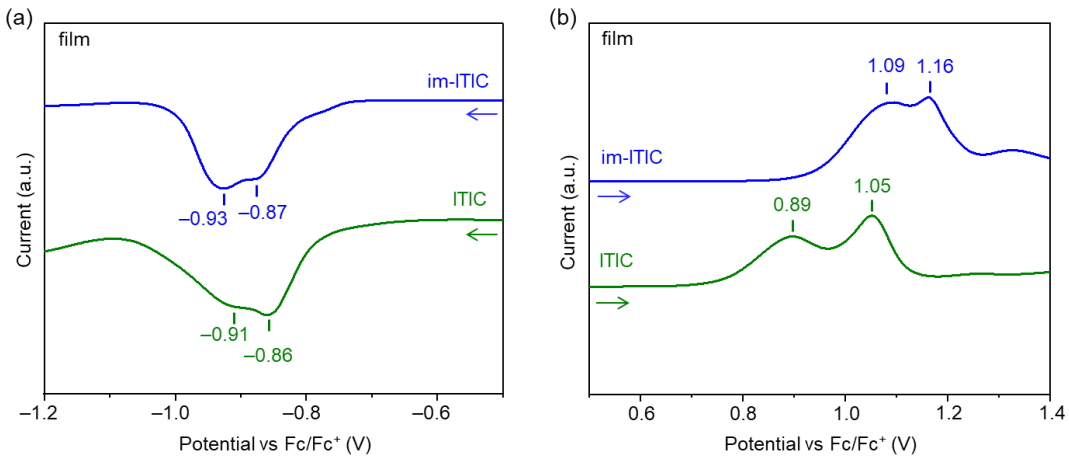

Figure 2.8. DPVs of **im-ITIC** and ITIC in film state for (a) negative and (b) positive scans in acetonitrile containing 0.1 M $TBAPF_6$.

To further understand the differences in the electronic structure caused by the aggregation behavior of **im-ITIC**, the electrochemical behaviors in film were investigated using DPV in CH_3CN containing 0.1 M $TBAPF_6$. As shown in **Figure 2.8a**, **im-ITIC** exhibits a reduction peak (−0.87 V) that is very close to ITIC (−0.86 V) in the solid state, which is significantly different from the peak position difference in solution. In contrast, their oxidation peaks maintained similar differences as in solution state (**Figure 2.8b**). This shows that the molecular energy level of **im-ITIC** in aggregation is quite different from that of single molecules, especially its LUMO energy level has a significant decrease in aggregation, reaching an energy level similar to the LUMO of ITIC.

Table 2.1. Physical properties of **im-ITIC** and ITIC.

Compounds	λ_{max}^{sol} / nm[a]	λ_{max}^{film} / nm	λ_{onset}^{film} / nm	ε_{sol} / L mol^{-1} cm^{-1}	E_g^{opt} / eV[b]	E_{HOMO} / eV[c]	E_{LUMO} / eV[c]	IP / eV [d]	EA / eV[e]
im-ITIC	621	636	704	1.62×10^5	1.76	–5.65	–3.79	5.97	3.85
ITIC	679	697	765	1.76×10^5	1.62	–5.54	–3.86	5.85	3.87

[a] Measured in chloroform solution. [b] E_g^{opt} was calculated using the equation: 1240 / λ_{onset}^{film}. [c] Values obtained from DPV. [d] Estimated from PYS. [e] Determined by LEIPS.

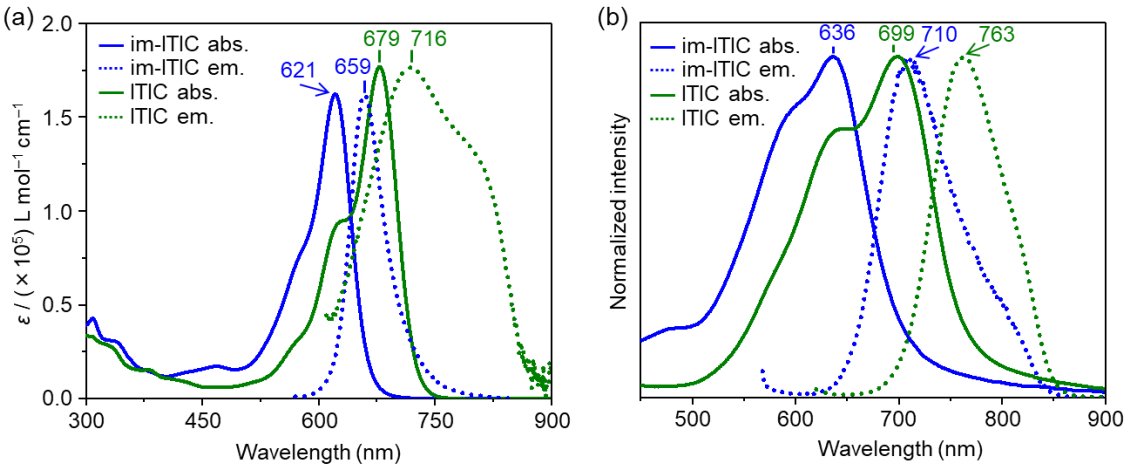

Figure 2.9. UV-vis absorption spectra (solid lines) and fluorescence spectra (dotted lines) of **im-ITIC** and ITIC in chloroform solutions (a) and films (b). Fluorescence spectra are unified to the same intensity as the absorption spectra for direct comparison.

Figure 2.9a displays the UV–vis absorption spectra of the compounds recorded in chloroform solution. Compared with ITIC, **im-ITIC** exhibits a noticeable blue shift in its absorption profile, with solution-phase absorption maxima (λ_{max}^{sol}) observed at 621 nm and 679 nm for **im-ITIC** and ITIC, respectively. The molar absorption coefficient (ε_{sol}) of **im-ITIC** was determined to be 1.62×10^5 L mol^{-1} cm^{-1}, closely matching that of ITIC (1.76×10^5 L mol^{-1} cm^{-1}), which aligns well with the oscillator strength (*f*) predicted from DFT calculations. In the film state, the absorption maxima (λ_{max}^{film}) appear at 636 nm for **im-ITIC** and 699 nm for ITIC. Interestingly, the red-shift of the absorption spectrum of **im-ITIC** (15 nm) from solution to solid state is smaller than that of ITIC (20 nm),

which also reflects the difference in their aggregation behaviors. H-aggregation is usually considered to cause a blue-shift in the absorption spectrum, which suggests that **im-ITIC** molecules may exhibit a mixed aggregation mode of H- and J-aggregations.[11] Meanwhile, the Stoke's shift of **im-ITIC** increases from 928 cm^{-1} in solution to 1638 cm^{-1} in the film, further confirming the presence of strong H-aggregation behavior in the solid state. The optical energy gap (E_g^{opt}) of **im-ITIC** and ITIC, estimated from the onset wavelengths of their film-state absorption spectra, were determined to be 1.76 eV and 1.62 eV, respectively. These values are also listed in **Table 2.1**.

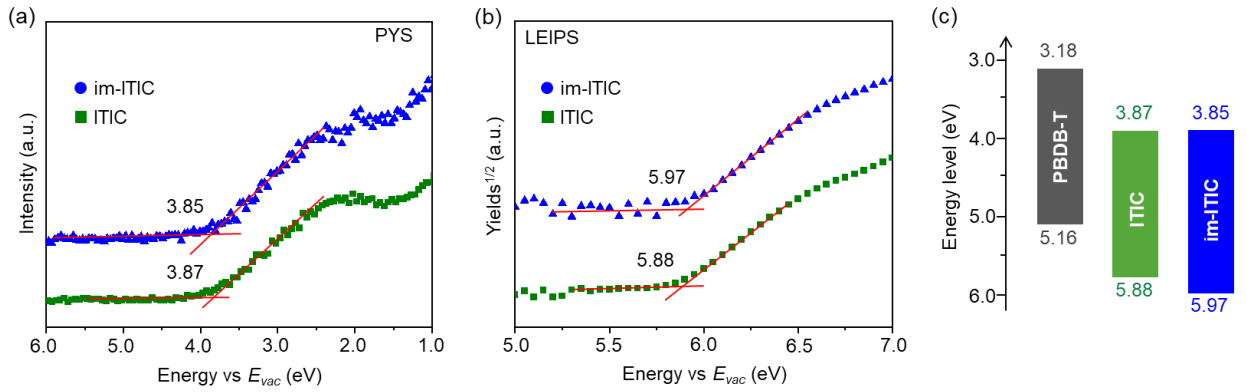

Figure 2.10. (a) LEIPS and (b) PYS of **im-ITIC** and ITIC in thin film state. (c) Energy level diagrams of **im-ITIC** and ITIC.

To evaluate the ionization energy (IE) and electron affinity (EA) of **im-ITIC** and ITIC, photoelectron yield spectroscopy (PYS)[12] and low-energy inverse photoemission spectroscopy (LEIPS)[13,14] were employed. As shown in **Figure 2.10a** and **Figure 2.10b**, the IE/EA values were determined to be 5.97/3.85 eV for **im-ITIC** and 5.88/3.87 eV for ITIC. Compared to the E_{HOMO} and E_{LUMO} values measured in solution, the differences in solid-state IE and EA became less pronounced, particularly with an EA difference of only 0.02 eV. This reduction in energy level offset is often attributed to enhanced intermolecular π–π stacking, which typically results in a shallower HOMO and a deeper LUMO, thereby narrowing the frontier orbital gap. In this context, the closer IE/EA values suggest that **im-ITIC** may exhibit stronger intermolecular packing in the solid state than ITIC. The corresponding energy level diagram, including the representative donor polymer PBDB-T (CAS No. 1415929-80-4), is illustrated in **Figure 2.10c**. Both **im-ITIC** and ITIC exhibit energy offsets greater than 0.3 eV relative to PBDB-T in both HOMO and LUMO levels, indicating sufficient energetic driving force for effective charge separation.[15] Based on the obtained IE, EA, and E_g^{opt} values, the E_b were estimated by **Eq. (1.1)** to be 0.36 for **im-ITIC** and 0.39 eV for ITIC, respectively. This reuslt suggest that excitons in **im-ITIC** experience weaker Coulombic binding compared to those in ITIC, which is favorable for efficient photogenerated charge separation.[15-17]

2.6 Single-crystal X-ray analysis

Single-crystal X-ray diffraction analysis was carried out to elucidate the molecular conformation and solid-state packing of **im-ITIC**. The crystals were obtained via vapor diffusion of methanol into a chloroform solution over a period of several weeks. As shown in **Figure 2.11**, **im-ITIC** adopts a characteristic W-shaped backbone and exhibits

two distinct configurations: configuration A, which displays an overall planar geometry, and configuration B, in which the terminal DCI units are twisted with a torsion angle of 17.8°. Compared with the more rigid and planar ITIC structure, the bent configuration for **im-ITIC** suggests increased packing disorder in the solid state.

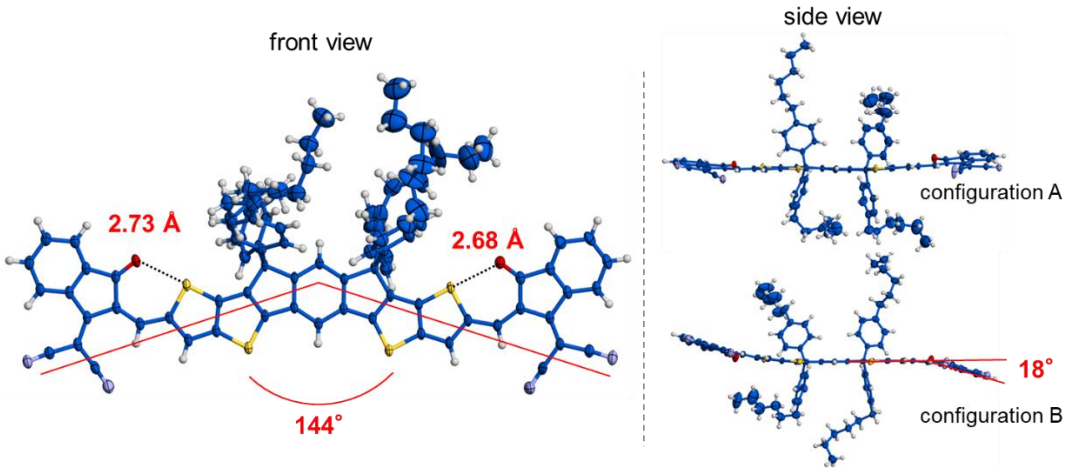

Figure 2.11. Configurations of **im-ITIC** monomer pattern in single crystal data from front and side views.

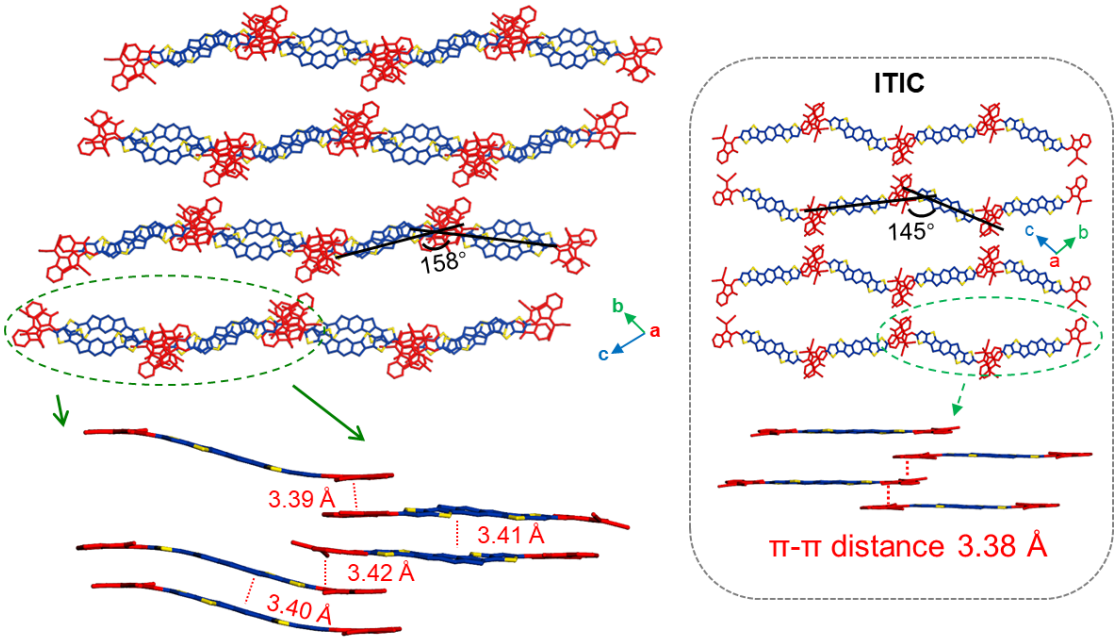

Figure 2.12. Top and side view representations of the single-crystal packing structures for **im-ITIC** (left) and ITIC (right). For better visualization, side chains have been omitted or simplified. The crystallographic data for ITIC were sourced from previously reported literature.[18] A detailed summary of the crystallographic parameters is provided in **Table S2.2**.

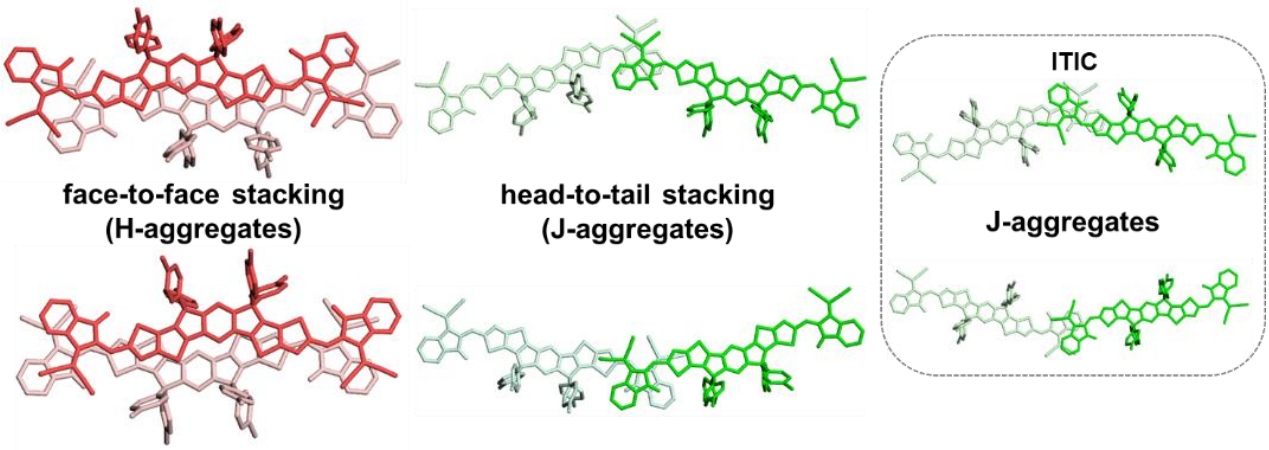

Figure 2.13. Different intermolecular packing pairs for **im-ITIC** and ITIC.

As shown in **Figure 2.12**, **im-ITIC** adopts a similarly twisted two-dimensional brickwork arrangement to that observed in ITIC. This packing motif further assembles into a three-dimensional crystal lattice, primarily driven by side-chain interactions and intermolecular hydrogen bonding. In general, both **im-ITIC** and ITIC form a similar diamond-shaped stacking framework with an angle of about 150°. For **im-ITIC**, an intermolecular π–π stacking distance of approximately 3.40 Å was observed. In the side view, if we look closely at their pairing patterns, we can see that **im-ITIC** forms the crystal framework by multiple pairing patterns, while ITIC molecules have only one pairing pattern.

If the pairing of **im-ITIC** and ITIC is divided into face-to-face stacking and head-to-tail stacking, obvious differences in their clustering patterns could be observed. As shown in **Figure 2.13**, ITIC was found to exclusively adopt head-to-tail stacking arrangements characteristic of J-aggregates. In contrast, **im-ITIC** exhibited a more diverse aggregation behavior, forming four distinct binary aggregate types—comprising two face-to-face H-aggregates and two head-to-tail J-aggregates. The proportion of H- to J-aggregates in **im-ITIC** was approximately 1:1, representing a marked deviation from the uniform J-type aggregation observed in ITIC.

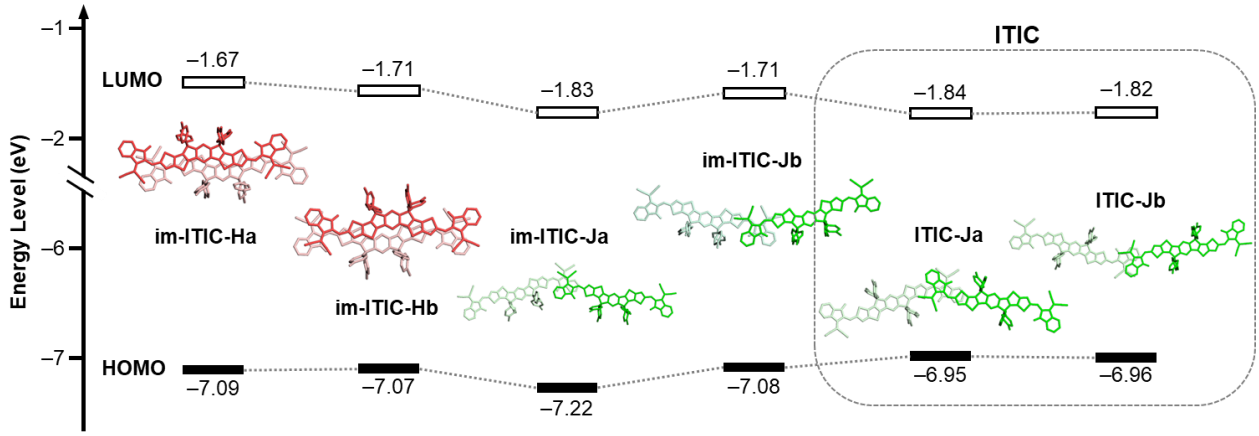

Figure 2.14. Energy level of HOMO and LUMO of **im-ITIC** and ITIC by different aggregation pairs. All calculations were performed at ωB97XD/6-31G(d,p) level.

Frontier molecular orbital energy levels of dimeric aggregates derived from **im-ITIC** and ITIC were calculated from their representative stacking configurations. As shown in **Figure 2.14**, the LUMO energy level of **im-ITIC-Ja** closely matches those of ITIC-Ja and ITIC-Jb. In contrast, the LUMO levels associated with the H-aggregates (**im-ITIC-Ha** and **im-ITIC-Hb**) are found to be higher than those of the corresponding J-aggregates (**im-ITIC-Ja** and **im-ITIC-Jb**).[11,19] These results suggest that the LUMO energy of **im-ITIC** is sensitive to the stacking geometry. On the other hand, the HOMO energy levels of both H- and J-aggregates remain relatively unchanged, likely due to the localization of HOMO electron density within the central core of the molecule. These computational findings are consistent with the experimentally obtained IE/EA results.

2.7 Photovoltaic properties

To evaluate the photovoltaic performance of **im-ITIC** and ITIC, OSCs were fabricated using an inverted device architecture of ITO/ZnO/PBDB-T:acceptor/MoO_3/Ag were fabricated, as shown in **Figure S2.1**.[20] The *J*–*V* characteristics of the best-performing devices, measured under simulated AM 1.5G illumination (100 mW cm^{-2}), are shown in **Figure 2.15**, and the corresponding OSC parameters are shown in **Table 2.2**. During the device optimization of **im-ITIC**-based OSCs, the use of processing additives such as 1,8-diiodooctane (DIO) and 1-chloronaphthalene (CN) was found to significantly influence both V_{OC} and J_{SC}.[6,21] Notably, the inclusion of DIO resulted in a marked improvement in V_{OC}, increasing from 0.95 V to 1.02 V, alongside enhanced J_{SC} and external quantum efficiency (EQE), as depicted in **Figure 2.15b**. Furthermore, UV-vis absorption measurements of DIO-treated **im-ITIC** films revealed a shoulder peak around 605 nm (**Figure S2.4** and **Figure S2.5**), which is attributed to the presence of H-aggregates.[6,11] These observations suggest that enhanced H-aggregation in the active layer contributes to the improved V_{OC} in **im-ITIC**-based OSCs.

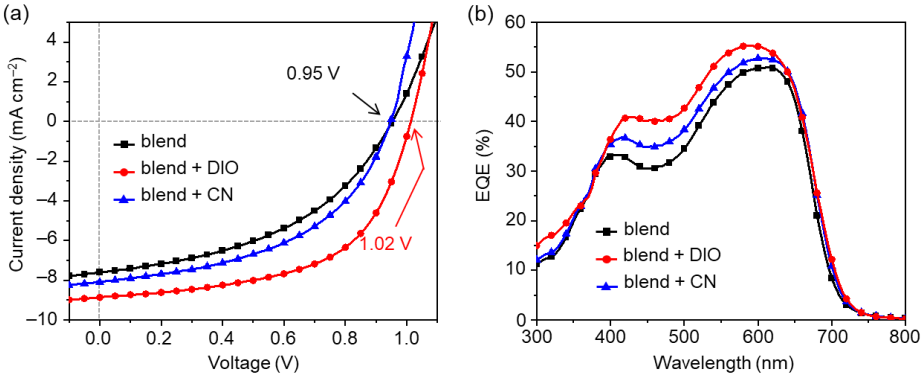

Figure 2.15. (a, b) *J*–*V* characteristics and EQE spectra of PBDB-T:**im-ITIC** OSCs with different additives.

Table 2.2 OSC characteristics of **im-ITIC** and **ITIC**.

Active layer	Additive	PCE (%)	J_{SC} (mA cm^{-2})	V_{oc} (V)	FF (%)	EQE_{max} (%)	E_{CT} (eV)
PBDB-T:**im-ITIC**	DIO[a]	5.13 (4.88 ± 0.37)	9.06 (8.84 ± 0.22)	1.02 (1.01 ± 0.01)	57 (56 ± 1)	56.2	1.57
PBDB-T:**im-ITIC**	CN[a]	3.74 (3.62 ± 0.12)	8.10 (7.98 ± 0.13)	0.95 (0.95 ± 0.01)	49 (56 ± 1)	52.7	1.54
PBDB-T:**im-ITIC**	-	3.25 (3.18 ± 0.06)	7.81 (7.71 ± 0.12)	0.95 (0.95 ± 0.01)	45 (44 ± 1)	50.8	1.54
PBDB-T:ITIC	DIO[b]	8.62 (8.41 ± 0.13)	14.73 (14.33 ± 0.28)	0.90 (0.90 ± 0.01)	65 (65 ± 1)	72.2	1.39

[a] 1 vol% concentration was added. [b] 0.5 vol% concentration was added.

Atomic force microscopy (AFM) was employed to examine the surface morphology of PBDB-T:**im-ITIC** blend films. As shown in **Figure S2.6**, all samples exhibited comparable surface textures and roughness, though **im-ITIC**-based films demonstrated a smoother surface relative to those based on ITIC. To further assess the crystallinity and molecular organization within the active layers, X-ray diffraction (XRD) analysis was conducted. As depicted in **Figure S2.7**, the addition of CN and DIO led to a noticeable enhancement in diffraction intensity along the out-of-plane direction, suggesting improved crystalline ordering in the blend films upon additive treatment.

The electron (μ_e) and hole (μ_h) mobilities of the PBDB-T:**im-ITIC** films processed with different additives were evaluated by space-charge-limited current (SCLC) method. The extracted mobilities are summarized in **Table S2.1**, **Figure S2.8a** and **Figure S2.8b**.[22-24] The μ_h remained constant at 2.5×10^{-5} cm^2 V^{-1} s^{-1} under all processing conditions. In contrast, a slight enhancement in μ_e was observed upon the addition of CN and DIO, increasing from 9.2×10^{-6} to 9.7×10^{-6} and 9.9×10^{-6} cm^2 V^{-1} s^{-1}, respectively. This improvement in μ_e is likely responsible for the enhanced J_{SC} and FF observed in the corresponding OSC devices.

The relationship between photocurrent density (J_{ph}) and effective applied voltage (V_{eff}) for PBDB-T:**im-ITIC** based OSCs is presented in **Figure S2.8c**.[25,26] Devices processed with CN or DIO exhibited J_{ph} saturation behavior, indicative of efficient charge extraction. In contrast, the device without any additive displayed no clear saturation, likely due to the non-geminate recombination. Based on the ratio of J_{ph} to the saturation current density (J_{sat}), the exciton dissociation probabilities ($P(E,T)$) were estimated to be 93% for CN-treated and 96% for DIO-treated devices. To further probe the extent of non-geminate recombination, the dependence of J_{SC} on light intensity (P_{light}) was analyzed. As shown in **Figure S2.8d**, the extracted exponential factors (α) were 0.87 for the non-additive film, 0.93 for the CN-treated film, and 0.99 for the DIO-treated film. An α value approaching unity, as seen in the DIO-processed device, suggests minimal non-geminate recombination losses. Conversely, the significantly lower α value observed in the untreated blend film implies a more pronounced recombination pathway. These findings are in good agreement with the photocurrent saturation trends shown in **Figure S2.8c**.

To elucidate the reason of the enhanced V_{OC} in the DIO-treated devices, the E_{CT} values was extracted from the normalized EQE spectra, as shown in **Figure 2.16**.[27] The E_{CT} of the DIO-treated PBDB-T:**im-ITIC** film was determined to be 1.57 eV, which is slightly higher than that of both the CN-treated and additive-free films (1.54 eV). A clear positive correlation between E_{CT} and V_{OC} was observed, indicating that the increased E_{CT} contributes to the higher V_{OC}.

The relatively lower PCE of **im-ITIC**-based devices compared to ITIC counterparts is mainly attributed to the reduced J_{SC}, as shown in **Figure S2.9a** and **Figure S2.9b**. This decline in J_{SC} is likely caused by the substantial spectral overlap between the absorption profiles of **im-ITIC** and PBDB-T (**Figure S2.10**), which limits the effective light-harvesting range. Despite this limitation, the **im-ITIC**-based OSC devices achieved a notably high V_{OC} of 1.02 V—an increase of 0.12 V relative to the ITIC-based counterpart. As discussed previously, both **im-ITIC** and ITIC exhibit comparable EA values in their pristine states. Therefore, the observed V_{OC} difference is more plausibly ascribed to variations in the interfacial E_{CT} rather than differences in intrinsic energy levels of the acceptors. In support of this, the E_{CT} of the PBDB-T:ITIC blend was determined to be 1.39 eV (**Figure S2.9c**).

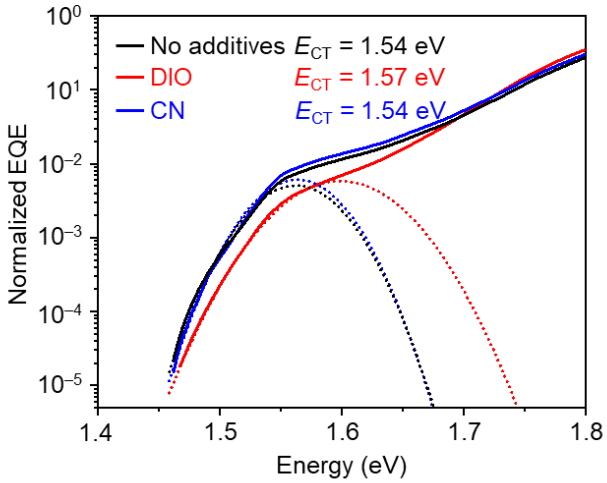

Figure 2.16. Normalized EQE spectra of the PBDB-T:**im-ITIC** blend films with different content of additives. The dashed plots indicate the fitting results to obtain E_{CT}.

2.8 Time-resolved infrared (TR-IR) absorption spectroscopy

Time-resolved infrared (TR-IR) absorption spectroscopy was utilized to study photoinduced charge generation in both pristine and blend films of **im-ITIC** and ITIC. This technique provides valuable insights into charge separation dynamics and the temporal behavior of free carriers. Notably, the vibrational frequency of the cyano group—commonly incorporated into NFAs as an electron-withdrawing moiety—undergoes a redshift (i.e., shift to lower wavenumbers) as the local electron density increases. This characteristic enables direct probing of intra- and intermolecular charge transfer processes within NFAs.[28-30]

TR-IR absorption spectra in the cyano stretching region were recorded under 660 nm pump pulse excitation, as presented in **Figure 2.17**. In the case of ITIC (**Figure 2.17b**), a negative signal at 2230 cm^{-1} and a broad positive feature spanning 2200–2160 cm^{-1} were observed. These signals are attributed to ground-state bleaching of the cyano stretching vibration, formation of the S_1 state via intramolecular charge transfer, and the generation of anionic ITIC species resulting from intermolecular charge separation, respectively.[28-30] These findings indicate that both intra- and intermolecular charge transfer processes occur in ITIC films upon photoexcitation. A similar spectral response was observed for **im-ITIC** (**Figure 2.17a**), where a negative peak at 2225 cm^{-1} and a positive band in the 2200–2160 cm^{-1} range appeared following pump irradiation. This confirms the occurrence of intermolecular charge transfer in the pristine **im-ITIC** film as well.

TR-IR measurements were also conducted on the **im-ITIC** and ITIC blend films with PBDB-T. As shown in **Figure 2.17d**, blending ITIC with PBDB-T led to a noticeable weakening of the absorption band at 2230 cm^{-1} (associated with the S_1 state), accompanied by a significant enhancement of the positive signal between 2200 and 2160 cm^{-1}. This spectral evolution suggests that heterojunction formation with the donor facilitates efficient charge separation and increases the population of ITIC anions. In contrast, for the PBDB-T:**im-ITIC** blend (**Figure 2.17c**), ground-state bleaching was detected at 2220 cm^{-1}, while the corresponding positive features were minimal. Although cationic **im-ITIC** species are theoretically expected to produce a blue-shifted CN stretching mode, their

oscillator strength is weak, rendering them difficult to observe directly.[38] Nevertheless, the depletion of neutral species due to hole transfer contributes to the bleaching signal. These findings imply that, in the case of **im-ITIC**, electrons are not trapped to form localized anionic states; instead, they are more likely to be released as free carriers, consistent with a more delocalized charge separation mechanism.

The generation of free electrons was further investigated by monitoring background absorption in the mid-infrared (mid-IR) region. Previous studies have shown that photoexcited free electrons in ITIC films produce broad absorption features spanning 4000–1000 cm^{-1}, which are attributed to intraband transitions of free electrons.[28,31-33] A similar broadband mid-IR absorption was observed in **im-ITIC** films upon 660 nm pump excitation, as shown in **Figure S2.11a** and **Figure S2.11b**. These results confirm that, akin to ITIC, free electron formation also occurs in the pristine **im-ITIC** film, supporting the presence of efficient charge delocalization and intermolecular electron transport.

The decay behavior of photoinduced free electrons in pristine ITIC and **im-ITIC** films is presented in **Figure 2.18a** and **Figure 2.18b**. In both cases, the transient absorption signal at 2050 cm^{-1} rises promptly following photoexcitation and then decays monotonically over time. Notably, within the 0–1000 ps time window, **im-ITIC** displays a longer carrier lifetime compared to ITIC. This extended lifetime is likely attributed to the smaller E_b of **im-ITIC**, which reduces the Coulombic attraction between electrons and holes, thereby suppressing charge recombination processes.

The decay dynamics of photoexcited carriers were further investigated in PBDB-T:**im-ITIC** and PBDB-T:ITIC blend films. Similar to their pristine counterparts, excitation of the acceptor components in the blends resulted in broad mid-IR absorption features (**Figure S2.11c** and **Figure S2.11d**), indicative of free electron generation. These observations confirm that free carriers are also present in the blend systems upon photoexcitation, consistent with the behavior observed in the neat acceptor films.

The transient absorption kinetics at 2050 cm^{-1} provide detailed insights into the generation and decay behavior of free electrons in the blend systems (**Figure 2.18c** and **Figure 2.18d**). As shown in **Figure 2.18c**, the ITIC-based blend exhibits a gradual increase in absorption during the initial 0–10 ps, indicating that charge separation is governed by hole transfer from photoexcited ITIC to the PBDB-T donor at the D/A interface. In contrast, the PBDB-T:**im-ITIC** blend demonstrates an immediate rise in free carrier absorption following photoexcitation, suggesting a significantly faster hole-transfer process for **im-ITIC** compared to ITIC. Despite this rapid charge separation, the free electron lifetime in the **im-ITIC** blend is notably shorter than that in the ITIC-based blend (**Figure 2.18d**). This observation is opposite to the trend observed in the pristine films, where **im-ITIC** exhibited longer-lived free carriers. These results are consistent with the photovoltaic results, in which PBDB-T:ITIC devices display higher J_{SC} than their **im-ITIC** counterparts.

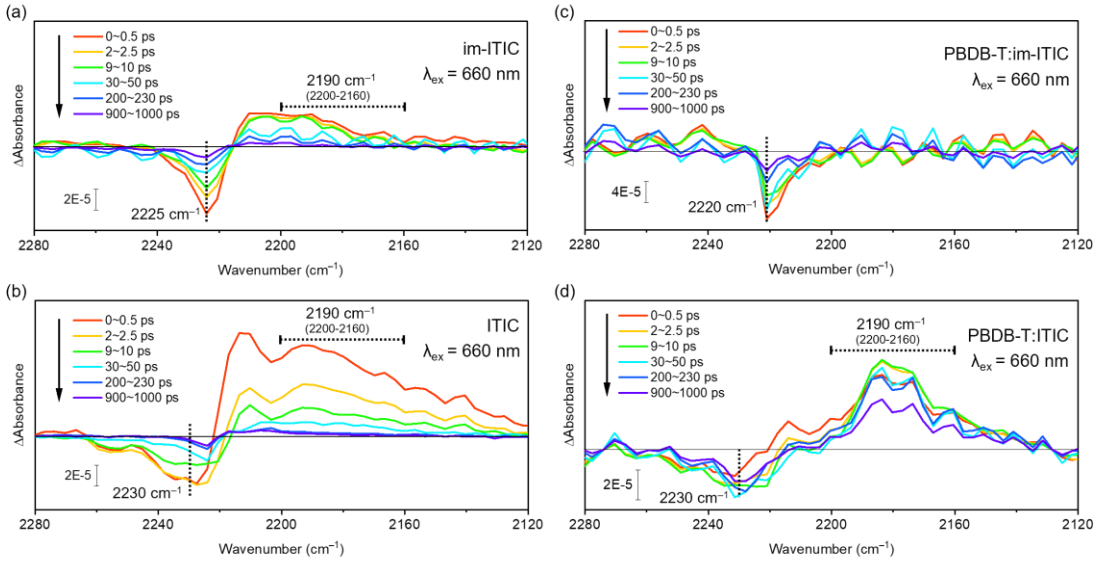

Figure 2.17. Differential vibrational spectra of cyano groups in NFAs upon 660 nm pump pulse excitation. (a, b) Spectra of pristine **im-ITIC** and ITIC films, respectively. (c, d) Corresponding spectra for the NFA domains in PBDB-T blend films under identical excitation conditions.

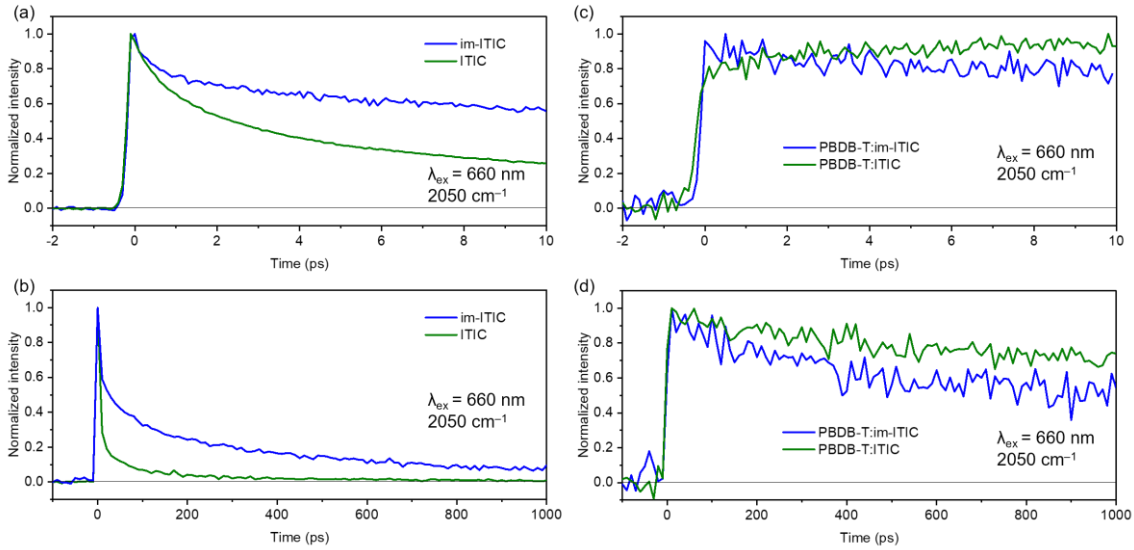

Figure 2.18. Time-resolved absorption profiles at 2050 cm^{-1} reflecting free electron dynamics in (a, b) pristine ITIC and **im-ITIC** films and (c, d) their corresponding PBDB-T blend films. The measurements were conducted by selectively photoexciting the NFA domains with a 660 nm pump pulse.

2.9 Molecular dynamic (MD) simulation

To investigate the origin of the V_{OC} difference, molecular dynamics (MD) simulations were performed for both **im-ITIC** and ITIC.[34-36] Representative snapshots from these simulations are shown in **Figure 2.19a** and **Figure 2.19b** for the pristine states, and in **Figure S2.12a** and **Figure S2.12b** for blends with a PBDB-T fragment. The ITIC molecules primarily exhibit tail-to-tail terminal stacking, while **im-ITIC** demonstrates both face-to-face H-aggregation and head-to-tail J-aggregation modes. These simulated packing patterns are consistent with the single-crystal structures observed earlier (**Figure 2.13**). Statistical analysis of the simulation data is presented in **Figure 2.19c** and **Figure S2.12c**, where radial distribution functions (RDFs) quantify the likelihood of locating a neighboring group at a given distance. A pronounced peak at approximately 3.5~3.8 Å is observed for **im-ITIC** in both pristine and blended states, indicating enhanced packing density through face-to-face π-π interactions. [37,38] Furthermore, the aggregation mode probabilities (**Figure 2.19d** and **Figure S2.12d**) clearly illustrate the distinct stacking behaviors of **im-ITIC** and ITIC, highlighting the structural basis for their differing photovoltaic properties.

To further explore the influence of processing additives on molecular packing, MD simulations were extended to **im-ITIC** with different additives in both pristine and blend states. As shown in **Figure S2.13**, the incorporation of DIO notably enhances the probability of face-to-face stacking in pristine **im-ITIC** systems. A similar trend was observed in the corresponding blend systems (**Figure S2.14**). RDF analysis (**Figure S2.13c** and **Figure S2.14c**) revealed a distinct peak around 4 Å for the CN-**im-ITIC** pair, whereas no such peak was found for DIO-**im-ITIC** interactions. This suggests that DIO does not engage in specific intermolecular interactions with **im-ITIC**, thereby facilitating tighter face-to-face π-π stacking compared to CN. Consequently, the presence of DIO promotes H-aggregation in **im-ITIC**, which plays a crucial role in achieving enhanced V_{OC} in organic solar cells.

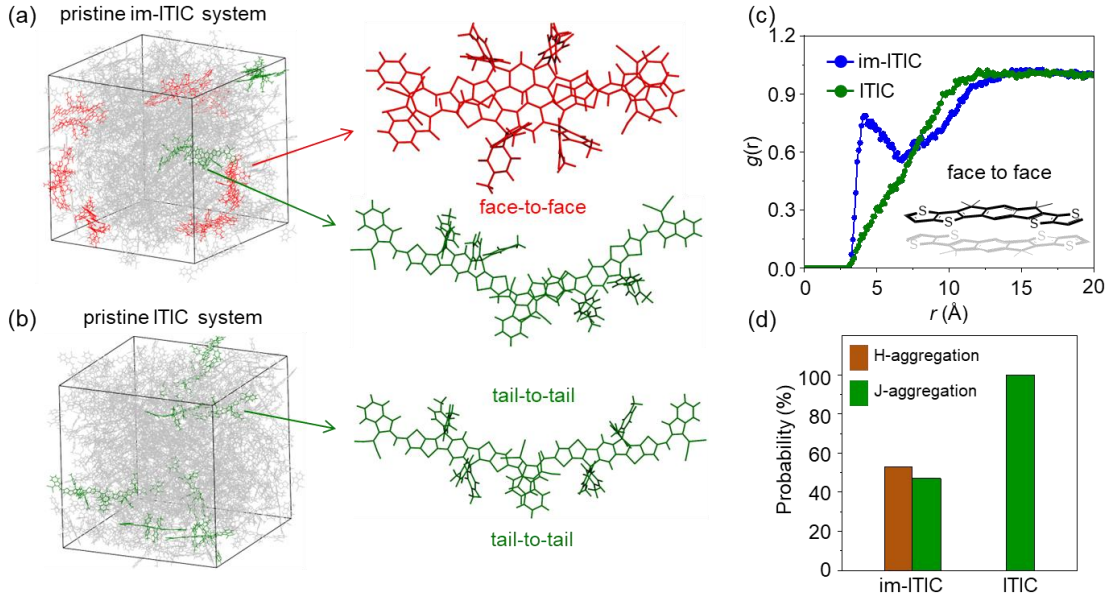

Figure 2.19. (a, b) Representative MD snapshots (left) and corresponding stacking configurations (right) for pristine **im-ITIC** and ITIC systems. (c) Radial distribution functions (RDFs) illustrating intermolecular packing tendencies. (d) Statistical probabilities of different aggregation modes. In the snapshots, face-to-face and tail-to-tail stacking arrangements are highlighted in red and green, respectively.

2.10 Excited state analysis

To elucidate the role of H-aggregation in enhancing the V_{OC}, time-dependent density functional theory (TD-DFT) calculations were performed using the ωB97XD/6-31G(d,p) level of theory on D:A clusters derived from MD-simulated stacking geometries.[17,37] **Figure 2.20** presents the spatial distributions of holes and electrons for the lowest CT and localized excited (LE) states in various aggregates formed between PBDB-T and either **im-ITIC** or ITIC. For **im-ITIC**-based clusters, the E_{CT} was calculated to be 2.06 eV for H-aggregates and 1.97 eV for J-aggregates. In comparison, the J-aggregate of the ITIC-based cluster showed a slightly lower E_{CT} of 1.94 eV. These results indicate that while J-aggregation yields similar CT states for both acceptors, H-aggregation in **im-ITIC** distinctly elevates the E_{CT} at the D/A interface. Moreover, the energy offset between the LE and CT states ($\Delta E_{LE\text{-}CT}$) was calculated to be 0.10 eV for **im-ITIC** H-aggregates, 0.12 eV for **im-ITIC** J-aggregates, and 0.21 eV for ITIC J-aggregates, suggesting that H-aggregation in **im-ITIC** may contribute to reduced energy loss.[39,40] In conclusion, the elevated E_{CT} associated with H-aggregation in **im-ITIC**—enabled by its asymmetric molecular design with steric hindrance on only one side—plays a key role in achieving higher V_{OC} in organic solar cells.

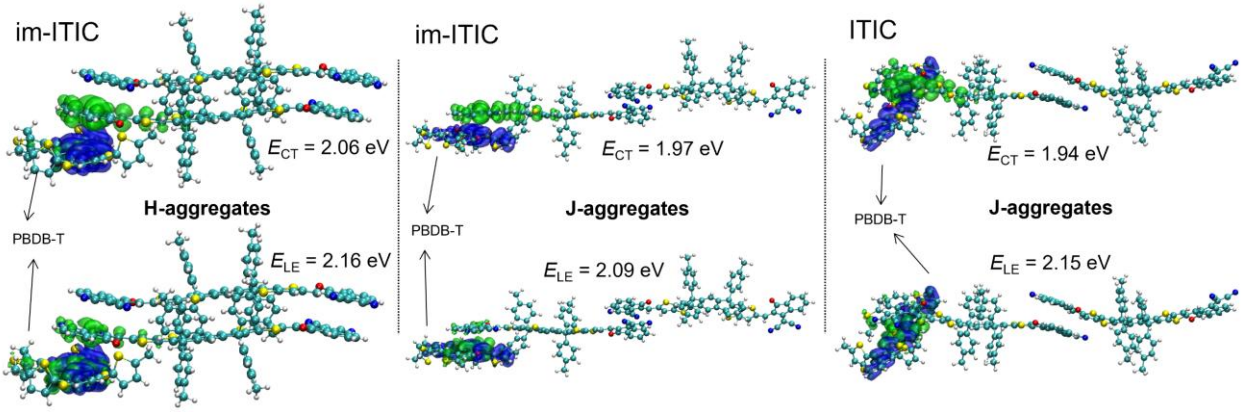

Figure 2.20. Spatial distributions of hole (blue) and electron (green) densities for various excited states in **im-ITIC** aggregates. The clusters were extracted from MD simulations, and the excited-state properties were calculated using the TD-DFT method at the ωB97XD/6-31G(d,p) level.

2.11 Conclusion

In summary, Chapter 2 investigates the influence of molecular aggregation on the V_{OC} in OSCs by designing a new ITIC isomer, **im-ITIC**, with C_{2v} symmetry through asymmetric side-chain substitution. The aggregation tendency of **im-ITIC** in solution was confirmed by concentration-dependent ^{1}H NMR measurements. LEIPS analyses revealed that the EA of pristine **im-ITIC** and ITIC films are nearly identical. Based on EA, IE, and E_g^{opt} values, the E_b values of **im-ITIC** were determined to be 0.04 eV lower than that of ITIC. Single-crystal X-ray diffraction showed that **im-ITIC** exhibits both H- and J-aggregation in the solid state. Devices based on PBDB-T:**im-ITIC** achieved a higher V_{OC} of 1.02 V, compared to 0.90 V for PBDB-T:ITIC. Furthermore, the V_{OC} of the **im-ITIC** device was further enhanced by using DIO as an additive. The E_{CT} of PBDB-T:**im-ITIC** and PBDB-T:ITIC films were determined to be 1.57 eV and 1.39 eV, respectively, showing a positive correlation with their V_{OC} values. TR-IR experiments revealed that **im-ITIC** exhibits a longer free carrier lifetime in its pristine form compared to ITIC, while its lifetime becomes shorter in the blend film, in agreement with the lower E_b and reduced J_{SC} in the corresponding device. MD simulations and TD-DFT calculations further demonstrated that H-aggregation in **im-ITIC** increases the E_{CT} at the D/A interface compared to J-aggregation, thereby contributing to the enhancement of V_{OC}. Overall, this study establishes a clear link between aggregation behavior and interfacial energetics in NFAs, providing valuable design guidelines for the development of high-V_{OC}, high-performance OSC materials.

2.12 Experimental Section

Supplementary Figures

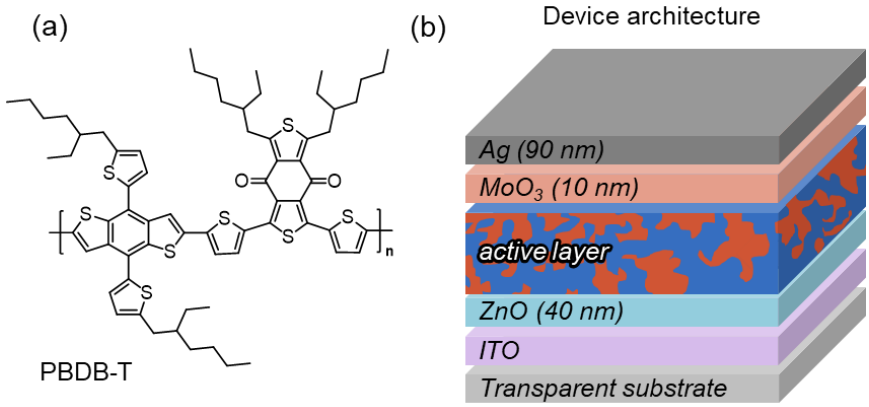

Figure S2.1. (a) Chemical structure of PBDB-T. (b) Device architecture of OSCs.

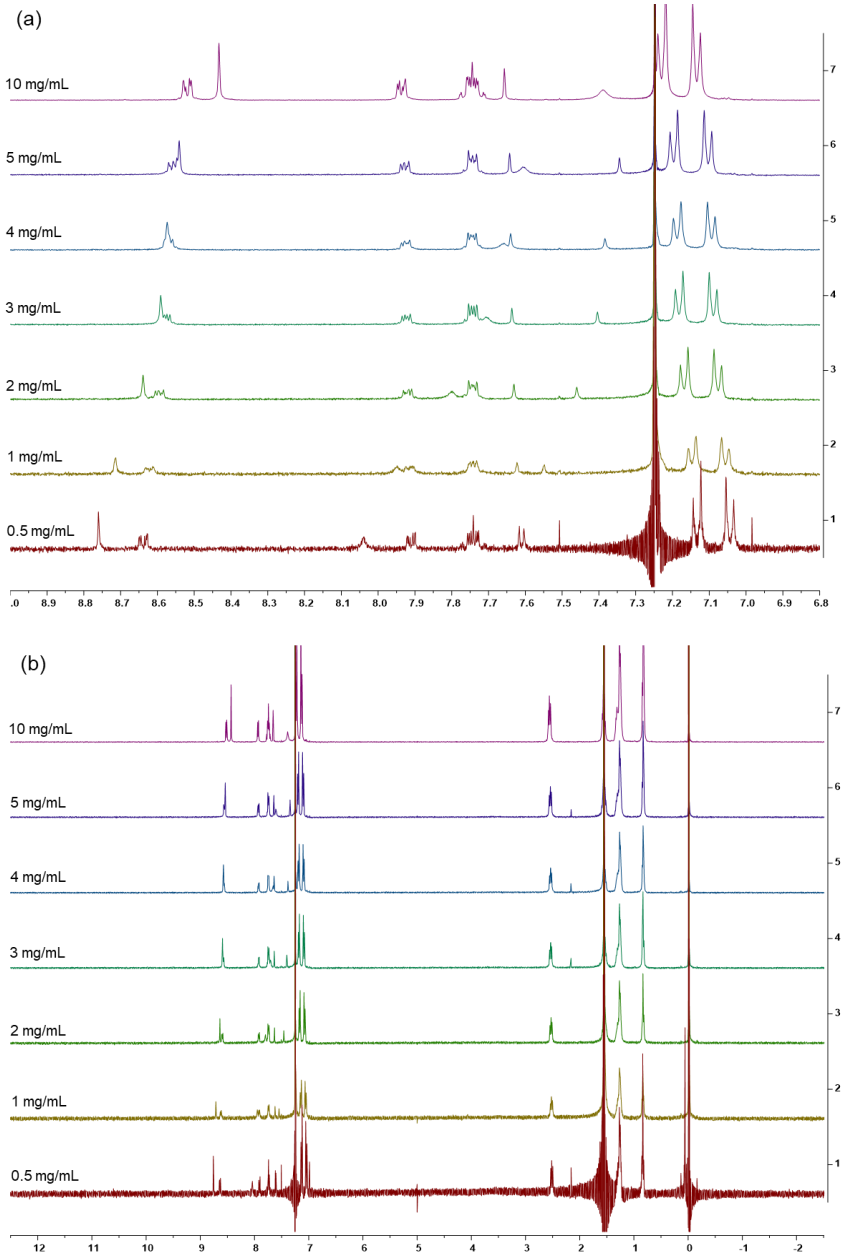

Figure S2.2. ^{1}H NMR (400 MHz, $CDCl_3$) spectra for different concentrations of **im-ITIC**.

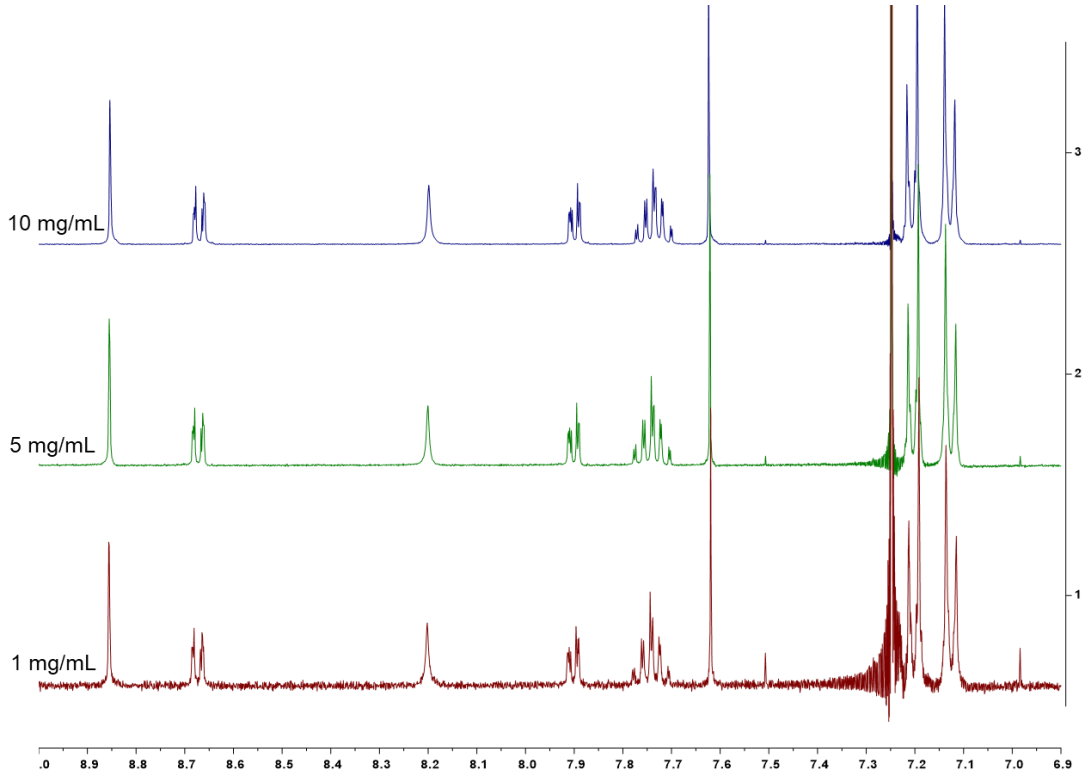

Figure S2.3. Concentration-dependent ^{1}H NMR spectra of the aromatic region for ITIC in $CDCl_3$ at 20 °C.

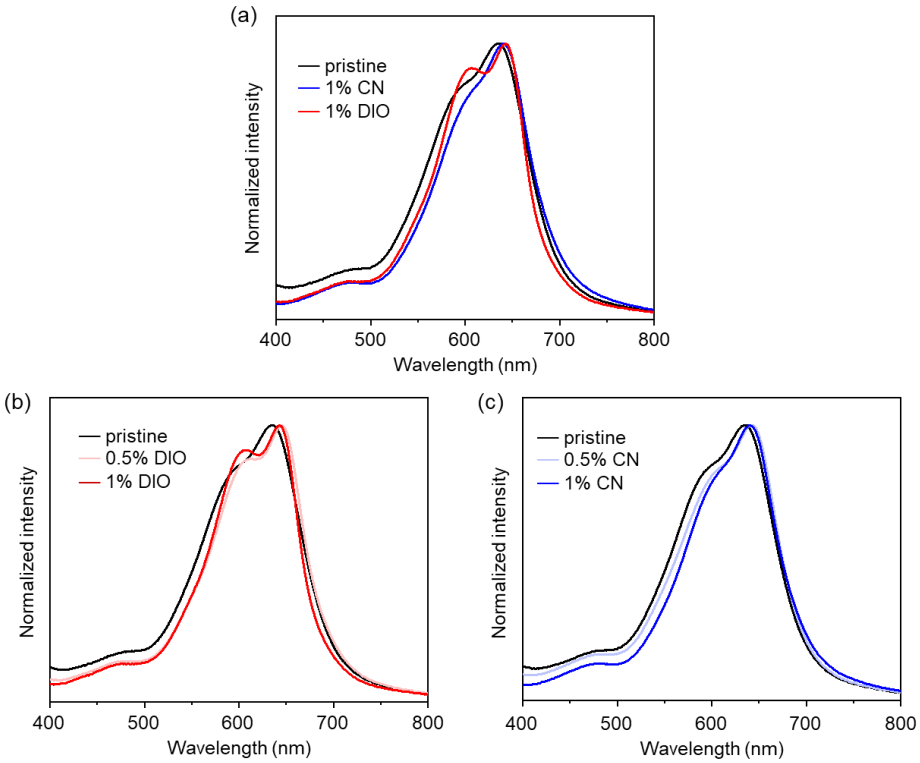

Figure S2.4. (a) UV-vis absorption spectra of **im-ITIC** without additive and with 1% CN or 1% DIO. (b) UV-vis absorption spectra of **im-ITIC** with different content of DIO. (c) UV-vis absorption spectra of **im-ITIC** with different content of CN.

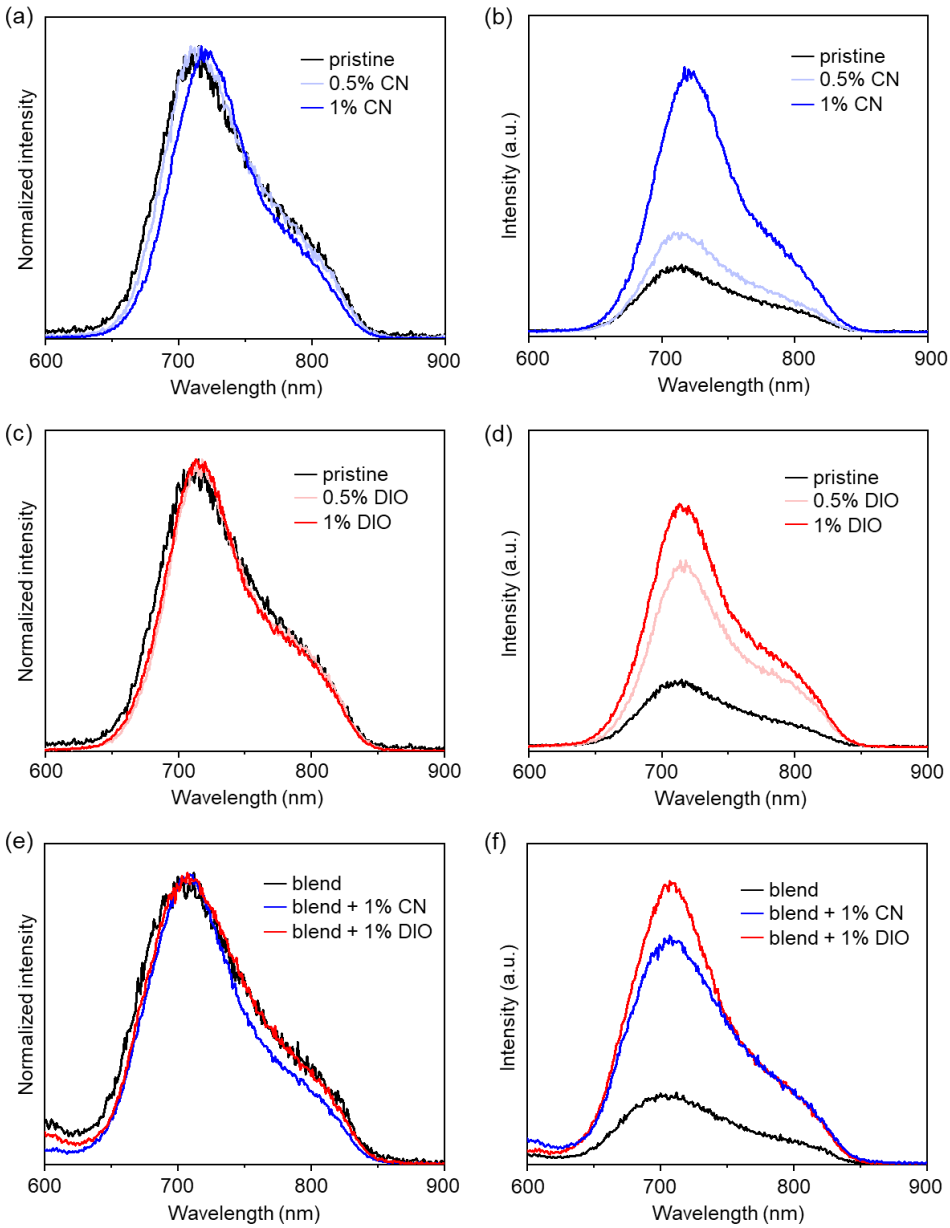

Figure S2.5. Photoluminescence spectra of **im-ITIC** films with different content of DIO (a and b) or CN (c and d). (e and f) Photoluminescence spectra of PBDB-T:**im-ITIC** blend films with different content of DIO or CN. Left: normalized intensity; Right: relative intensity.

Table S2.1. Hole and electron mobilities of the blend films with different additives.

	μ_h ($cm^2/V \cdot s$)[a]	μ_e ($cm^2/V \cdot s$)[b]
blend	2.51×10^{-5}	0.92×10^{-5}
blend + DIO	2.52×10^{-5}	0.99×10^{-5}
blend + CN	2.52×10^{-5}	0.97×10^{-5}

[a] ITO/PEDOT:PSS/PBDB-T:acceptor/MoO_3/Ag. [b] ITO/ZnO/PBDB-T:acceptor/Ca/Ag.

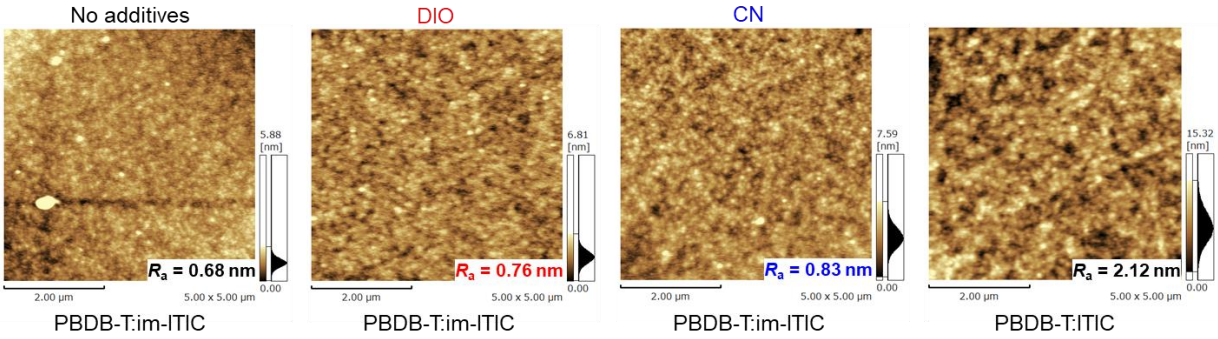

Figure S2.6. (a) AFM height images of PBDB-T:**im-ITIC** blend films with different additives. (b) and (c) Out-of-plane and in plane X-ray diffractograms of films with different additives.

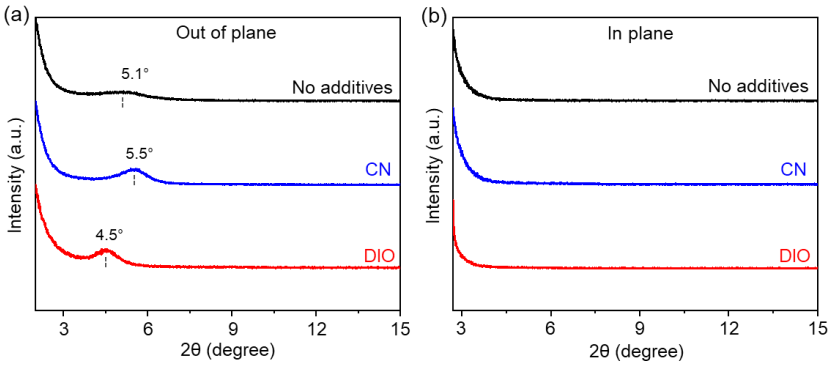

Figure S2.7. Out-of-plane (a) and in plane (b) X-ray diffractograms of films with different additives.

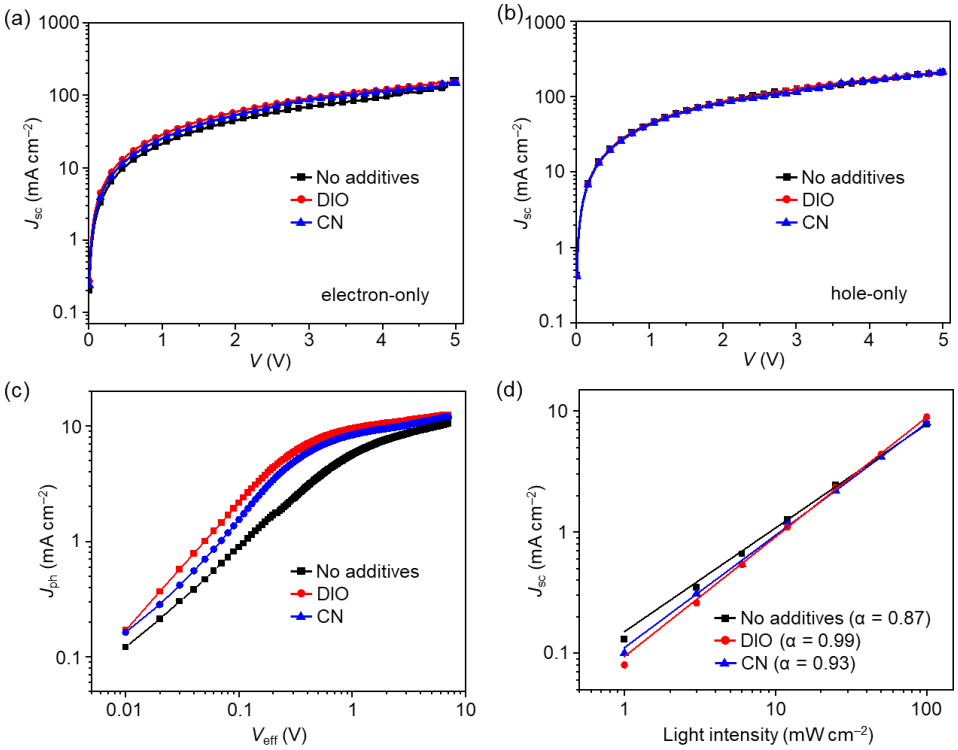

Figure S2.8. *J*–*V* plots of (a) electron-only and (b) hole-only devices based on PBDB-T:**im-ITIC** blend films with different additives; (c) $J_{ph} - V_{eff}$ curves of devices based on PBDB-T:**im-ITIC** blend films with different additives; (d) light intensity dependent J_{sc} of devices based on PBDB-T:**im-ITIC** with different additives.

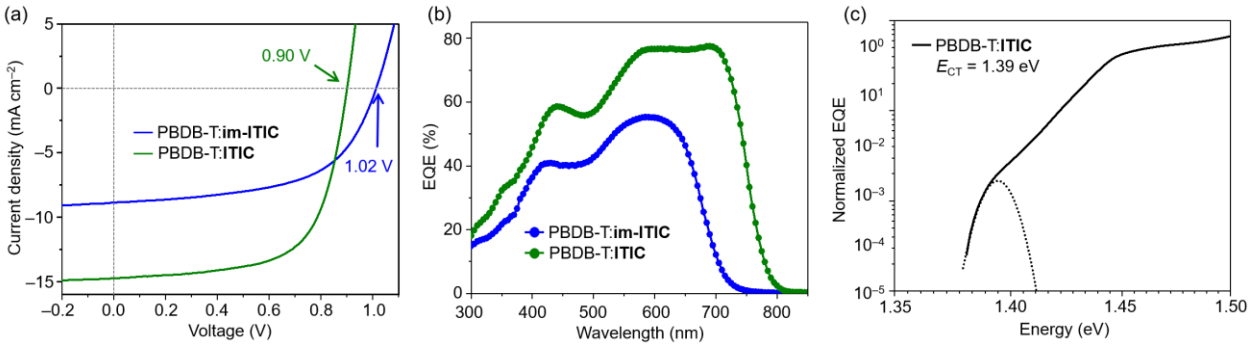

Figure S2.9. (a, b) *J–V* curves EQE spectra of best-performing OSCs of **im-ITIC** and ITIC**.** (c) Normalized EQE for the PBDB-T:ITIC blend film. The dashed plot indicates the fitting results to obtain E_{CT}.

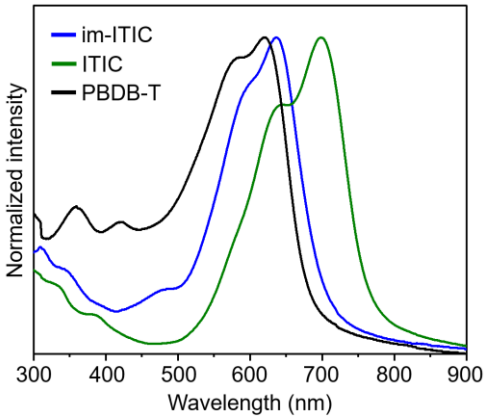

Figure S2.10. UV-vis absorption spectra of **im-ITIC**, ITIC and PBDB-T in pristine films.

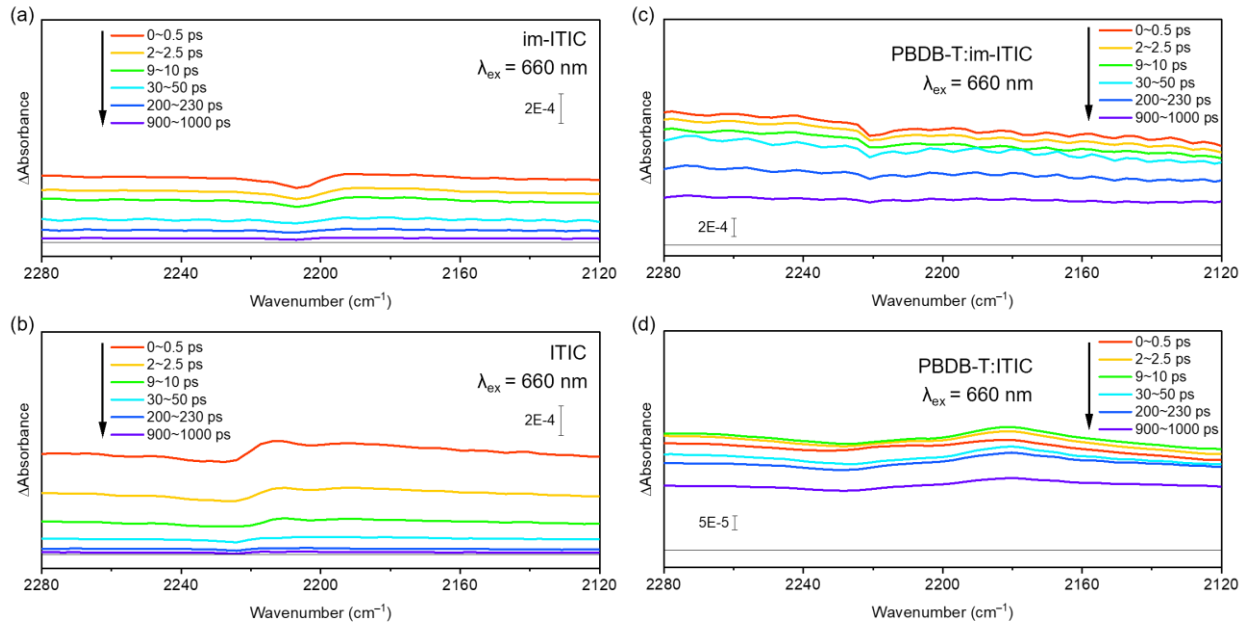

Figure S2.11. Transient IR spectra recorded for NFAs following excitation by a pump pulse. Panels (a) and (b) show results for pristine **im-ITIC** and ITIC, respectively. In panels (c) and (d), the NFA domains within PBDB-T blend films were excited using the same 660 nm pump pulse.

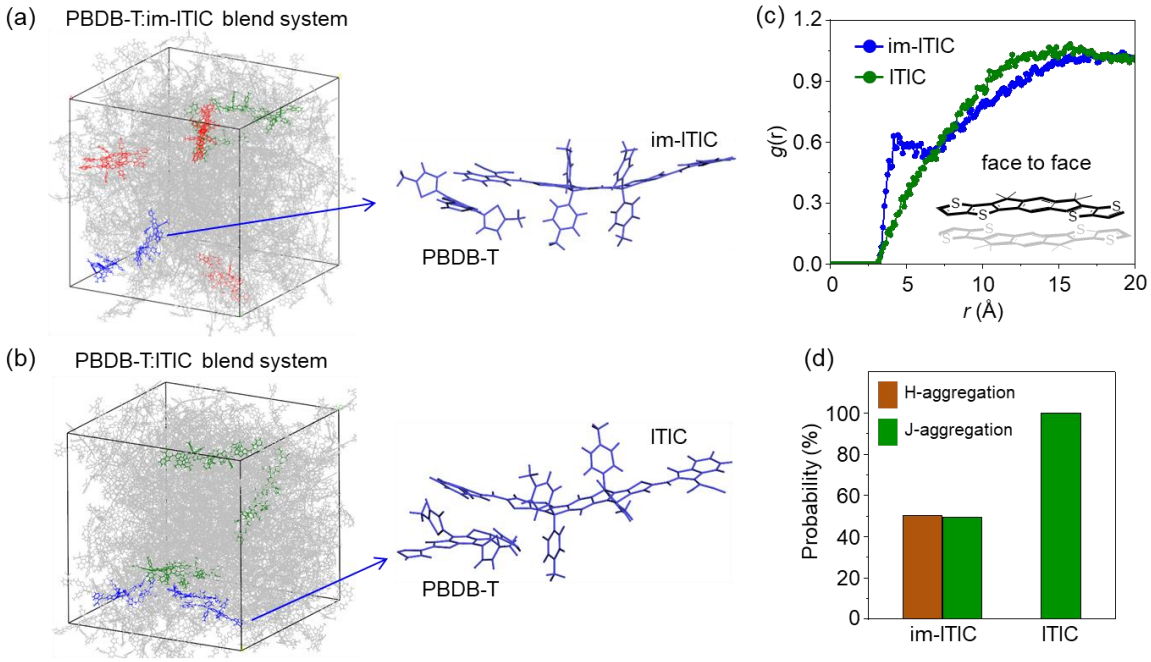

Figure S2.12. (a, b) Representative MD-derived snapshots (left) and corresponding stacking configurations (right) for blend films of PBDB-T with **im-ITIC** and ITIC. (c) RDF calculated for the respective blend systems. (d) Distribution probabilities of various aggregation types observed in the blends.

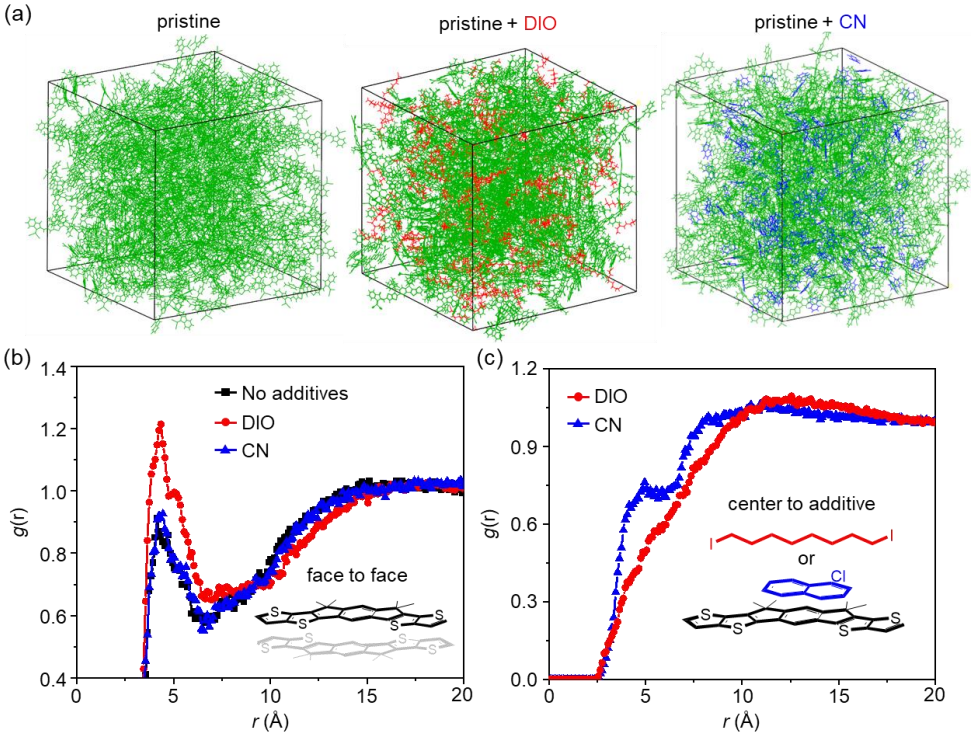

Figure S2.13. (a) Snapshots from the MD results of **im-ITIC**-based pristine systems with different additives. (b) and (c) Radial distribution function data for **im-ITIC**-based pristine systems.

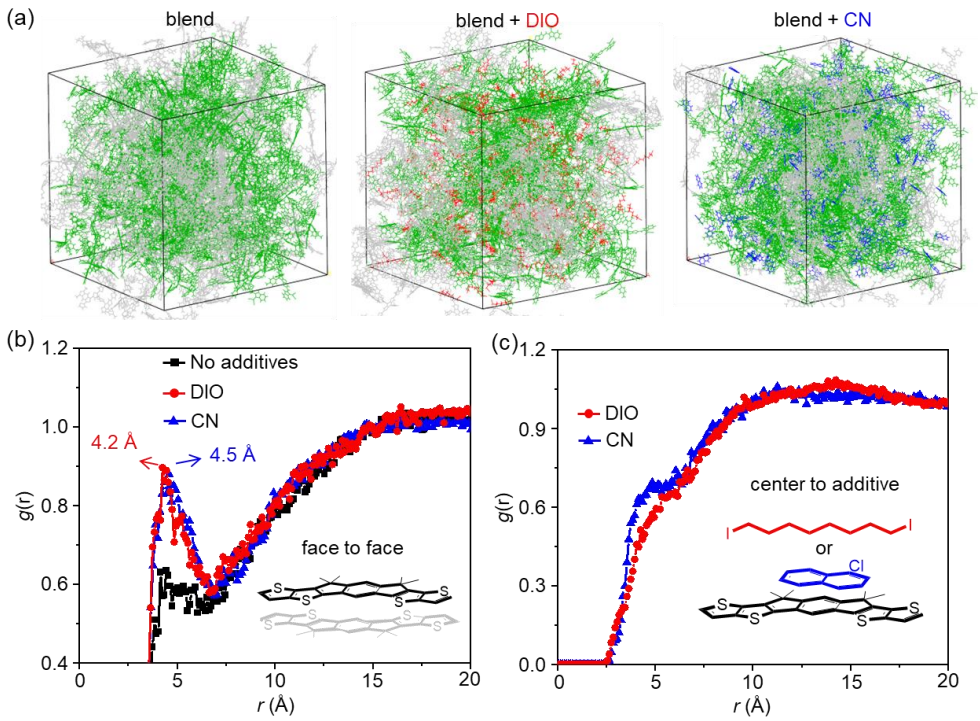

Figure S2.14. (a) Snapshots from the MD results of PBDB-T:**im-ITIC**-based blend systems with different additives. (b) and (c) Radial distribution function data for blend systems with different additives.

General Information

Nuclear magnetic resonance spectra for both ^{1}H and ^{13}C nuclei were acquired using a JEOL ECS-400 instrument, with chemical shifts (δ) expressed in ppm and signal types classified as s (singlet), d (doublet), t (triplet), m (multiplet), or br (broad). High-resolution mass spectrometric data were collected using the Thermo Scientific LTQ Orbitrap XL system operating under atmospheric pressure chemical ionization (APCI) conditions. TGA profiles were measured under N_2 atmosphere at a constant heating rate of 10 °C/min employing a Shimadzu TGA-50 analyzer. Optical absorption in the UV-vis range was evaluated with a Shimadzu UV-3600 spectrophotometer. Steady-state photoluminescence spectra were recorded using a Fluoromax-4 fluorometer in photon-counting mode, utilizing a Hamamatsu R928P detector. DPV were carried out on a BAS CV-620C voltammetric analyzer using a platinum disk as the working electrode, platinum wire as the counter electrode, and $Ag/AgNO_3$ as the reference electrode at a scan rate of 100 mV s^{-1}. PYS was performed by Bunkoukeiki BIP-KV202GD. LEIPS was performed by Ulvac-Phi, Inc. LEIPS system. AFM was obtained by Shimadzu SPM9600. Elemental analysis was performed on a Perkin Elmer LS-50B instrument by the Elemental Analysis Section of Comprehensive Analysis Center (CAC), SANKEN, The University of Osaka.

OSC device fabrication and evaluation

OSCs were fabricated with the device structure ITO/ZnO/active layer/MoO_3/Ag. ITO-coated glass substrates were cleaned sequentially by ultrasonication in acetone, deionized water, and 2-propanol for 15 minutes each, followed by ozone treatment for 1.5 hours. A ZnO layer was deposited by spin-coating a precursor solution of zinc acetate dihydrate (200 mg), ethanolamine (55 μL), and 2-methoxyethanol (2 mL) at 4000 rpm, followed by thermal annealing at 200 °C for 30 minutes in air. The active layer was spin-coated onto the ITO/ZnO substrates inside a nitrogen-filled glove box. MoO_3 (10 nm) and Ag (100 nm) top electrodes were thermally evaporated through a shadow mask under a vacuum of 10^{-5} Pa, defining an active area of 0.09 cm^2. After encapsulation, the photovoltaic performance was measured in air under simulated AM 1.5G illumination (100 mW cm^{-2}) using a solar simulator (SAN-EI ELECTRIC, XES-301S). *J-V* characteristics were recorded with a KEITHLEY 2400 source meter. External quantum efficiency (EQE) spectra were acquired using a Soma Optics S-9240 system. Film thicknesses of active layers were measured by a KLA Tencor Alpha-step IQ profilometer.

SCLC measurements

Hole-only and electron-only devices were fabricated with using the architectures ITO/PEDOT:PSS/active layer/MoO_3/Au and ITO/ZnO/active layer/Ca/Ag, respectively.[30] The active layers of PBDB-T:**im-ITIC** and PBDB-T:ITIC OSCs were prepared using the best-performing conditions. The carrier mobilities of these devices were calculated by the following equation:

$$J = \frac{9}{8}\varepsilon\varepsilon_0\mu\frac{V^2}{d^3}$$

where ε, ε_0, and d are the dielectric constant of the active layer, the permittivity of free space, the carrier mobility, and the measured thickness of active layer, respectively. We used the values of $\varepsilon = 3$, $\varepsilon_0 = 8.8 \times 10^{-12}$.

Single-Crystal X-ray Diffraction Analysis

Single crystals of **im-ITIC** were grown by the vaper diffusion method at room temperature. **im-ITIC** (3 mg) samples were dissolved in $CHCl_3$ (1 mL) in a 2 mL dram vial, and it were sealed by tinfoil then poked a few small holes in the tinfoil to control its diffusion speed. This vial was placed into a 20 mL dram vial containing methanol (~ 10 mL). The larger vial was then sealed tightly and left undisturbed at room temperature until crystal growth occurred (2 weeks).

Table S2.2. Crystal data and structure refinement for **im-ITIC**.

Parameters	Content
CCDC number	2427692
Empirical formula	C93H78Cl4N4O2S4
Formula weight	1568.17
Temperature / K	103
Crystal system	triclinic
Space group	$P\bar{1}$
a / Å	13.7559(2)
b / Å	22.3818(5)
c / Å	30.1984(5)
α/°	76.312(2)
β/°	84.506(1)
γ/°	74.959(2)
Volume / Å^3	8718.2(3)
Z	4
ρ_{calc} / mg mm^{-3}	1.195
μ / mm^{-1}	2.621
F(000)	3276
Crystal size / mm^3	0.318 ×0.165 × 0.066
2Θ range for data collection	2.176 to 75.716°
Index ranges	$-17 \leq h \leq 17$, $-27 \leq k \leq 20$, $-37 \leq l \leq 32$
Reflections collected	98009
Independent reflections	35185
Data/restraints/parameters	35185/907/2053
GooF	1.022
Final R indexes [I>2σ (I)]	R_1 = 0.0820, wR_2 = 0.2437
Final R indexes [all data]	R_1 = 0.0895, wR_2 = 0.2526
Largest diff. peak/hole / e Å^{-3}	1.55/−0.99

The fitting and calculation details for the E_{CT}

The E_{CT} value was estimated by fitting the normalized EQE spectra using following equation:

$$EQE(E) = \frac{f}{E\sqrt{4\pi\lambda_L k_B T}} exp(-\frac{(E_{CT} + \lambda_L - E)}{4\lambda_L k_B T})$$

Where k_B is the Boltzmann's constant, T is the absolute temperature, E_{CT} is the energy of CT states, and λ_L is related to the width of the CT absorbance band, with contributions from internal/environmental reorganization and/or energetic disorder.

Femtosecond transient IR absorption measurements

The TA measurements were performed using a pump-probe method with a Ti:sapphire regenerative amplifier (Spectra Physics, Solstice; 90 fs pulse duration, 1 kHz repetition rate) coupled with optical parametric amplifiers (OPAs; Spectra Physics, TOPAS Prime). A 660 nm excitation pulse from the OPA (0.1 μJ per pulse, 500 Hz) was used to selectively excite the acceptor layer. The beam diameter was approximately 200 μm, corresponding to a pump fluence of 3.18 μJ mm^{-2}. For the MIR measurements, probe pulses were generated through difference frequency generation between the signal and idler beams from the OPA in an $AgGaS_2$ crystal and detected using a 128-channel linear MCT array detector (Infrared Systems Development, FPAS-0144). The frequency shift of the cyano group in the acceptors was analyzed after subtracting the background signal attributed to free carrier absorption from the spectra, where the background in the narrow region was approximated as a linear baseline. The sample films for transient absorption (TA) measurements were prepared by drop-casting a chloroform solution containing ITIC, **im-ITIC**, and their blend with PBDB-T (1:1 by weight) onto a CaF_2 substrate. During the measurement, the film was placed in an IR cell filled with 20 torr of N_2.

Theological calculations

In the calculations, the alkyl chains in the acceptor molecules were replaced by methyl groups for simplification. In the calculation of the distribution of frontier molecular orbitals, structural optimization was calculated by density functional theory (DFT) calculations at B3LYP/6-31G(d,p). The geometry optimizations and frequency analyses of all the molecules were performed by using DFT for the ground state and anion/cation states on the long-range corrected (LRC) functional ωB97XD and 6-31G(d,p) basis set.

Molecular-dynamics (MD) simulations

The MD simulations were performed with the Gromacs 2024.2 software package based on the general AMBER force field (GAFF) with the RESP charges.[41-44] The Berendsen method was applied for the control of pressure, and the velocity rescaling method with a stochastic term (v-rescale) was applied for the control of temperature. All covalent hydrogen bonds were constrained using the LINCS algorithm and a cutoff range for the short-range electrostatics was set to 13 Å. For **im-ITIC** and ITIC, the molecular geometry was optimized at B3LYP/6-31G(d,p) level. For PBDB-T, 10 repeat units were used as a fragment of the polymer, then the molecular geometry was optimized at B3LYP/6-31G level. For pristine system, the initial cell was built by randomly placing total 200 molecules of **im-ITIC** or ITIC and 200 fragments of DIO or CN in a 20 × 20 × 20 nm^3 cubic box to generate an

initial geometry. For blend system, 30 fragments of PBDB-T, 200 fragments of **im-ITIC** or ITIC and 200 fragments of DIO or CN were randomly placed in a 30 × 30 × 30 nm^3 cubic box to generate an initial geometry. The simulation was carried out using the following procedure:[34,35] (1) 5 ns of simulation at 800 K and 100 bar to make molecules close together quickly; (2) 10 ns of simulation at 800 K and 1 bar, then cooling down to 300 K in 10 ns; (3) 30 ns of equilibration at 300 K and 1 bar for production. The final results were the average of three independent simulations. Radial distribution functions (RDF) were computed using the TRAVIS program.[45]

Preparation of materials

Commercially available reagents were used without purification. All reactions were carried out under a nitrogen atmosphere. Compounds 1[10] were prepared by the reported procedures.

Synthetic procedures and characterizations

Synthesis of diethyl 4,6-bis(5-(triisopropylsilyl)thieno[3,2-b]thiophen-2-yl)isophthalate (**2**): Compound 1 (0.9 g, 2.4 mmol), triisopropyl(5-(tributylstannyl)thieno[3,2-b]thiophen-2-yl)silane (3.5 g, 6.0 mmol), and $Pd(PPh_3)_4$ (138 mg, 0.12 mmol) were dissolved in 30 mL of toluene under inert atmosphere. The mixture was heated to 120 °C and stirred for 15 h. After the reaction, the system was allowed to cool to room temperature and then concentrated under reduced pressure. The crude product was purified by column chromatography on silica gel using *n*-hexane/chloroform (1:2) as eluent, yielding compound **2** as a yellow solid (1.6 g, 83%). ^{1}H NMR (400 MHz, $CDCl_3$): δ (ppm) 8.15 (s, 1H), 7.70 (s, 1H), 7.35 (s, 2H), 7.28 (s, 2H), 4.29-4.24 (m, 4H), 1.39-1.32 (m, 6H), 1.18-1.11 (m, 36H), 0.93-0.89 (t, *J* = 7.24 Hz, 6H).

Synthesis of **im-IDTT**: To a solution of 1-bromo-4-hexylbenzene (3.1 mL, 15.3 mmol) in THF (20 mL) at –78 °C, *n*-butyllithium solution (1.56 M in *n*-hexane, 9.9 mL, 15.3 mmol) was added dropwise and stirred for 1 H. The solution was kept at –78 °C, and a solution of compound **2** (1.6 g, 2.0 mmol) in THF (50 mL) was added dropwise. The mixture was slowly warmed up to room temperature and stirred for 16 h and then quenched by water. The solution was extracted by $CHCl_3$ and washed with water and brine. The organic phase was concentrated and purified by column chromatography on silica gel using *n*-hexane/$CHCl_3$/EtOAc (10/2/1, v/v/v) as an eluent to give 2a as yellow solid (1.6 g, 60%). This compound was subjected immediately to a solution of 50 mL acetic acid with 1 mL of concentrated sulfuric acid, and reflux for 4 h. After reaction, the mixture was washed with water and extracted by $CHCl_3$. The organic phase was concentrated and purified by column chromatography on silica gel using *n*-hexane/$CHCl_3$ (4/1, v/v) as an eluent to give **im-IDTT** as light orange solid (683 mg, 57%). ^{1}H NMR (400 MHz, $CDCl_3$): δ (ppm) 7.52 (s, 2H), 7.30-7.27 (m, 4H), 7.09-7.07 (d, *J* = 8.59 Hz, 8H), 6.97-6.95 (d, *J* = 8.59 Hz, 8H), 2.50-2.47 (m, 8H), 1.53-1.48 (m, 8H), 1.29-1.26 (m, 24H), 0.86-0.83 (t, *J* = 6.79 Hz, 12H). ^{13}C NMR (100 MHz, $CDCl_3$) *δ*: 151.41, 146.38, 142.85, 141.95, 141.65, 140.38, 137.53, 133.98, 128.34, 127.96, 126.67, 124.25, 120.45, 109.85, 63.13, 35.64, 31.80, 31.48, 29.24, 22.71, 14.19. HRMS (APCI) m/z calcd. for $C_{68}H_{75}S_4$ $[M+H]^+$: 1019.4673; found: 1019.4755 . Elemental Anal. Calcd. for $C_{68}H_{74}S_4$: C 80.11, H 7.32, N 0.00; found: C 80.05, H 7.19, N 0.00.

Synthesis of ***im-IDTT-CHO***: **im-IDTT** (300 mg, 0.29 mmol) was placed in a two-necked flask and dissolved in THF (25 mL). Lithium diisopropylamide (5.88 mL, 1.0 M in THF/*n*-hexane) was added to the mixture at –78 °C.

After stirring for 1 h at the temperature, *N*,*N*-dimethylformamide (0.9 mL, 11 mmol) was added. The mixture was gradually warmed up to room temperature and stirred for 12 h. The reaction was quenched by water and extracted by $CHCl_3$. After removal of the solvent under reduced pressure, the crude product was purified by column chromatography on silica gel using *n*-hexane/$CHCl_3$ (3/1, v/v) as an eluent to give **im-IDTT-CHO** as orange solid (277 mg, 88%). This compound was subjected immediately to the next reaction without further purification. ^{1}H NMR (400 MHz, $CDCl_3$): δ (ppm) 9.88 (s, 2H), 7.95 (s, 2H), 7.66 (s, 1H), 7.62 (s, 1H), 7.05-7.03 (d, *J* = 8.36 Hz, 8H), 6.99-6.97 (d, *J* = 8.29 Hz, 8H), 2.51-2.47 (m, 8H), 1.53-1.48 (m, 8H), 1.31-1.26 (m, 24H), 0.87-0.83 (t, *J* = 6.79 Hz, 12H).

Synthesis of ***im-ITIC***: Pyridine (0.5 mL) was added to the solution of ***im-IDTT-CHO*** (100 mg, 0.093 mmol) and 3-(dicyanomethylidene)indan-1-one (108 mg, 0.56 mmol) in $CHCl_3$ (15 mL) and the resulting mixture was stirred at 75 °C for 12 h. The reaction mixture was washed with water 3 times and the organic phase was concentrated. The crude product was purified by column chromatography on silica gel using *n*-hexane/$CHCl_3$ (2/1 to 1/2, v/v) as eluent, followed by further purification with reprecipitation using $CHCl_3$ and acetone to give **im-ITIC** as deep blue solid (96 mg, 72%). ^{1}H NMR (400 MHz, $CDCl_3$) *δ*: 8.66 (s, 2H), 8.61-8.59 (m, 2H), 7.93-7.91 (m, 2H), 7.84 (s, 2H), 7.76-7.73 (m, 4H), 7.63 (s, 1H), 7.49 (s, 1H), 7.17-7.15 (d, *J* = 8.41 Hz, 8H), 6.99-6.97 (d, *J* = 8.29 Hz, 8H), 2.55-2.51 (m, 8H), 1.53-1.50 (m, 8H), 1.32-1.25 (m, 24H), 0.85-0.82 (t, *J* = 6.50 Hz, 12H). ^{13}C NMR (100 MHz, $CDCl_3$) *δ*: 188.15, 159.64, 154.86, 152.51, 147.26, 146.67, 143.32, 142.71, 139.92, 139.24, 138.98, 137.81, 137.04, 136.82, 136.54, 135.25, 134.74, 128.92, 127.90, 125.22, 124.09, 122.33, 114.58, 114.25, 112.00, 69.37, 63.86, 35.65, 31.78, 31.54, 29.25, 22.71, 14.18. HRMS (APCI) m/z calcd. for $C_{94}H_{83}N_4O_2S_4$ $[M]^+$: 1428.5354; found: 1428.5428. Elemental Anal. Calcd. for $C_{94}H_{82}N_4O_2S_4$: C 79.07, H 5.79, N 3.92; found: C 78.78, H 5.89, N 3.84.

2.13 References

1 Deibel C., Strobel T., Dyakonov V., *Adv. Mater.* **2010**, *22*, 4097-4111.

2 Zhu X. Y., Yang Q., Muntwiler M., *Acc. Chem. Res.* **2009**, *42*, 1779-1787.

3 Zou Y. L., Holmes R. J., *Acs Applied Materials & Interfaces* **2015**, *7*, 18306-18311.

4 Deng Y. H., Yuan W., Jia Z., Liu G., *J. Phys. Chem. B* **2014**, *118*, 14536-14545.

5 Cai K., Xie J. J., Zhang D., Shi W. J., Yan Q. F., Zhao D. H., *J. Am. Chem. Soc.* **2018**, *140*, 5764-5773.

6 Zhao Q. Q., Lai H. J., Chen H., Li H., He F., *J. Mater. Chem. A* **2021**, *9*, 1119-1126.

7 Li S., Fu L. Y., Xiao X. X., Geng H., Liao Q., Liao Y., Fu H. B., *Angew. Chem. Int. Ed.* **2021**, *60*, 18059-18064.

8 Kim J. H., Schembri T., Bialas D., Stolte M., Würthner F., *Adv. Mater.* **2022**, *34*, 2104678.

9 Lin Y. Z., Wang J. Y., Zhang Z. G., Bai H. T., Li Y. F., Zhu D. B., Zhan X. W., *Adv. Mater.* **2015**, *27*, 1170-1174.

10 Pal T. K., Neogi S., Bharadwaj P. K., *Chem. Eur. J.* **2015**, *21*, 16083-16090.

11 Spano F. C., *Acc. Chem. Res.* **2010**, *43*, 429-439.

12 Yang J. P., Bussolotti F., Kera S., Ueno N., *J. Phys. D: Appl. Phys.* **2017**, *50*, 423002.

13 Yoshida H., *Chem. Phys. Lett.* **2012**, *539*, 180-185.

14 Yoshida H., *J. Electron. Spectrosc. Relat. Phenom.* **2015**, *204*, 116-124.

15 Liu J., Chen S. S., Qian D. P., Gautam B., Yang G. F., Zhao J. B., Bergqvist J., Zhang F. L., Ma W., Ade H., Inganäs O., Gundogdu K., Gao F., Yan H., *Nat. Energy* **2016**, *1*, 16089.

16 Mori H., Jinnai S., Hosoda Y., Muraoka A., Nakayama K., Saeki A., Ie Y., *Angew. Chem. Int. Edit.* **2024**, *63*, e202409964.

17 Wang K., Jinnai S., Urakami T., Sato H., Higashi M., Tsujimura S., Kobori Y., Adachi R., Yamakata A., Ie Y., *Angew. Chem. Int. Edit.* **2024**, *63*, e202412691.

18 Aldrich T. J., Matta M., Zhu W. G., Swick S. M., Stern C. L., Schatz G. C., Facchetti A., Melkonyan F. S., Marks T. J., *J. Am. Chem. Soc.* **2019**, *141*, 3274-3287.

19 Giannini S., Blumberger J., *Acc. Chem. Res.* **2022**, *55*, 819-830.

20 Zhao W. C., Li S. S., Yao H. F., Zhang S. Q., Zhang Y., Yang B., Hou J. H., *J. Am. Chem. Soc.* **2017**, *139*, 7148-7151.

21 Zheng Z., He E. F., Wang J., Qin Z. T., Niu T. Q., Guo F. Y., Gao S. Y., Ma Z. F., Zhao L. C., Lu X. H., Xue Q. F., Cao Y., Mola G. T., Zhang Y., *J. Mater. Chem. A* **2021**, *9*, 26105-26112.

22 Malliaras G. G., Salem J. R., Brock P. J., Scott J. C., *Phys. Rev. B* **1999**, *59*, 10371-10371.

23 Goh C., Kline R. J., McGehee M. D., Kadnikova E. N., Fréchet J. M. J., *Appl. Phys. Lett.* **2005**, *86*, 122110.

24 Dimitrov S. D., Durrant J. R., *Chem. Mater.* **2014**, *26*, 616-630.

25 Wu J. L., Chen F. C., Hsiao Y. S., Chien F. C., Chen P. L., Kuo C. H., Huang M. H., Hsu C. S., *ACS Nano* **2011**, *5*, 959-967.

26 Proctor C. M., Kim C., Neher D., Nguyen T. Q., *Adv. Funct. Mater.* **2013**, *23*, 3584-3594.

27 Vandewal K., Benduhn J., Nikolis V. C., *Sustain. Energy Fuels* **2018**, *2*, 538-544.

28 Yamakata A., Kato K., Urakami T., Tsujimura S., Murayama K., Higashi M., Sato H., Kobori Y., Umeyama T., Imahori H., *Chem. Sci.* **2024**, *15*, 12686-12694.

29 Wang K., Jinnai S., Urakami T., Sato H., Higashi M., Tsujimura S., Kobori Y., Adachi R., Yamakata A., Ie Y., *Angew. Chem. Int. Ed.* **2024**, e202412691.

30 Jinnai S., Murayama K., Nagai K., Mineshita M., Kato K., Muraoka A., Yamakata A., Saeki A., Kobori Y., Ie Y., *J. Mater. Chem. A* **2022**, *10*, 20035-20047.

31 Yamakata A., Ishibashi T., Onishi H., *Chem. Phys. Lett.* **2001**, *333*, 271-277.

32 Yamakata A., Kawaguchi M., Nishimura N., Minegishi T., Kubota J., Domen K., *J. Phys. Chem. C* **2014**, *118*, 23897-23906.

33 Pankove J. I., *Optical Processes in Semiconductors*, Dover, 1975.

34 Ye L., Hu H. W., Ghasemi M., Wang T. H., Collins B. A., Kim J. H., Jiang K., Carpenter J. H., Li H., Li Z. K., McAfee T., Zhao J. B., Chen X. K., Lai J. L. Y., Ma T. X., Bredas J. L., Yan H., Ade H., *Nat. Mater.* **2018**, *17*, 253-260.

35 Li Y. K., Guo Y., Chen Z., Zhan L. L., He C. L., Bi Z. Z., Yao N. N., Li S. X., Zhou G. Q., Yi Y. P., Yang Y., Zhu H. M., Ma W., Gao F., Zhang F. L., Zuo L. J., Chen H. Z., *Energy Environ. Sci.* **2022**, *15*, 855-865.

36 Han G. C., Yi Y. P., *Acc. Chem. Res.* **2022**, *55*, 869-877.

37 Zhang G. C., Chen X. K., Xiao J. Y., Chow P. C. Y., Ren M. R., Kupgan G., Jiao X. C., Chan C. C. S., Du X. Y., Xia R. X., Chen Z. M., Yuan J., Zhang Y. Q., Zhang S. F., Liu Y. D., Zou Y. P., Yan H., Wong K. S., Coropceanu V., Li N., Brabec C. J., Bredas J. L., Yip H. L., Cao Y., *Nat. Commun.* **2020**, *11*, 3943.

38 Coropceanu V., Chen X. K., Wang T. H., Zheng Z. L., Brédas J. L., *Nat. Rev. Mater.* **2019**, *4*, 689-707.

39 Zhan L. L., Li S. X., Li Y. K., Sun R., Min J., Chen Y. Y., Fang J., Ma C. Q., Zhou G. Q., Zhu H. M., Zuo L. J., Qiu H. Y., Yin S. C., Chen H. Z., *Adv. Energy Mater.* **2022**, *12*, 2201076.

40 Eisner F. D., Azzouzi M., Fei Z. P., Hou X. Y., Anthopoulos T. D., Dennis T. J. S., Heeney M., Nelson J., *J. Am. Chem. Soc.* **2019**, *141*, 6362-6374.

41 Hess B., *Abstr. Pap. Am. Chem. Soc.* **2009**, *237*, 435-447.

42 Bayly C. I., Cieplak P., Cornell W. D., Kollman P. A., *J. Phys. Chem.* **1993**, *97*, 10269-10280.

43 Wang J. M., Wolf R. M., Caldwell J. W., Kollman P. A., Case D. A., *J. Comput. Chem.* **2004**, *25*, 1157-1174.

44 Lu T., Chen F. W., *J. Comput. Chem.* **2012**, *33*, 580-592.

45 Brehm M., Thomas M., Gehrke S., Kirchner B., *J. Chem. Phys.* **2020**, *152*, 164105.

Chapter 3 Development of Ladder-Type Fused π-Conjugated Units Bearing Spiro units for Non-Fullerene Acceptors

3.1 Introduction

Focusing on NFAs has led to the utilization of fused structures in the central portion and electron-withdrawing functional groups at both terminal positions of conjugated frameworks, which has been established as an effective molecular design.[1-4] However, a molecular design based on the electronic structures should also be considered to further improve solar cell performance in terms of charge-carrier generation.

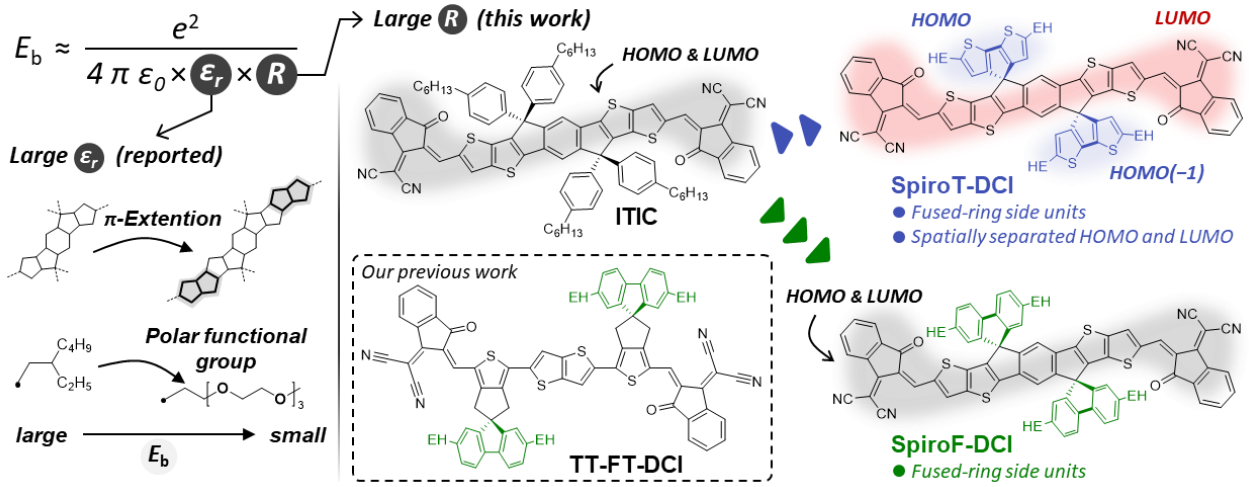

Figure 3.1. Molecular design to reduce the E_b of organic semiconductors and chemical structures of **SpiroT-DCI**, **SpiroF-DCI**, and ITIC

Organic semiconductors generally possess a relatively small dielectric constant (ε_r) and thus the hole-electron pairs formed by photoexcitation are tightly bound in a molecule via the force of Coulomb attraction.[5-8] The energy required to dissociate excitons into free-charge carriers is called the exciton binding energy (E_b). E_b is classically expressed with basic parameters by **Eq. (3.1)**[9]:

$$E_b \approx \frac{e^2}{4\pi\varepsilon_0\varepsilon_r R} \tag{3.1}$$

In this equation, e is the elementary charge, ε_0 is the vacuum dielectric constant, and R is the average electron–hole distance in the molecule. If the E_b of semiconductors can be reduced, excitons generated in BHJ OSCs will be more effectively dissociated due to a smaller donor/acceptor energy offset.[10-12] Therefore, reducing the E_b of organic semiconductors by increasing the ε_r and extending the conjugation or introduction of polarizable units is regarded as a rational approach (**Figure 3.1**, left).[13-17] Zhang *et al.* reported that enhancement of the hole/electron delocalization via polymerization of a small π-conjugated compound led to a reduction in the E_b.[15] Li et al. showed that asymmetric glycolate substitution onto Y6-based compounds, named Y6-4O, successfully reduced its E_b. Y6-4O showed an improved external quantum efficiency (EQE) of 1.4% in single-component (SC) OSCs.[17] On the other hand, according to the above equation, the E_b of organic semiconductors is also expected to decrease by increasing the R in the photoexcited state. Photoinduced charge separation in organic semiconductors is generally

mediated by the S_1 excited state, in which one electron is transitioned from the HOMO to the LUMO in a molecule. Therefore, we considered that the increased *R* can be attained by detaching the spatial distribution of the HOMO and LUMO of semiconductor molecules. However, the development of organic semiconductors with a tuned *R* in the S_1 state has not been reported.

Recently, our group has reported that the introduction of spiro-substituted biphenyl units has advantages that improve the OSC characteristics of a non-fused type NFA **TT-FT-DCI** (**Figure 3.1**).[18] The π-extended biphenyl unit adjusts the frontier molecular orbital energy level by modifying the chemical structure. Replacing the biphenyl unit with an electron-donating bithiophene unit tunes the shallow HOMO energy level, which leads to a shift in the electronic distribution of the HOMO from the conjugated backbone to the bithiophene unit. Therefore, we hypothesized that the tuning of *R* could be achieved by utilizing the structural feature of a perpendicular orientation in a spiro-substituted unit against a π-conjugated main framework. To investigate the effectiveness of this molecular design, we selected a representative fused-ring type of ITIC framework in this study.[1,2,19] Therefore, we designed new ITIC-based NFAs **SpiroT-DCI** and **SpiroF-DCI**, in which bithiophene and biphenyl skeletons are spiro-substituted into the ITIC (**Figure 3.1**, right). In this study, the effect of electronic structures on *R*, E_b, and OSC characteristics were investigated.

3.2 Theory investigation

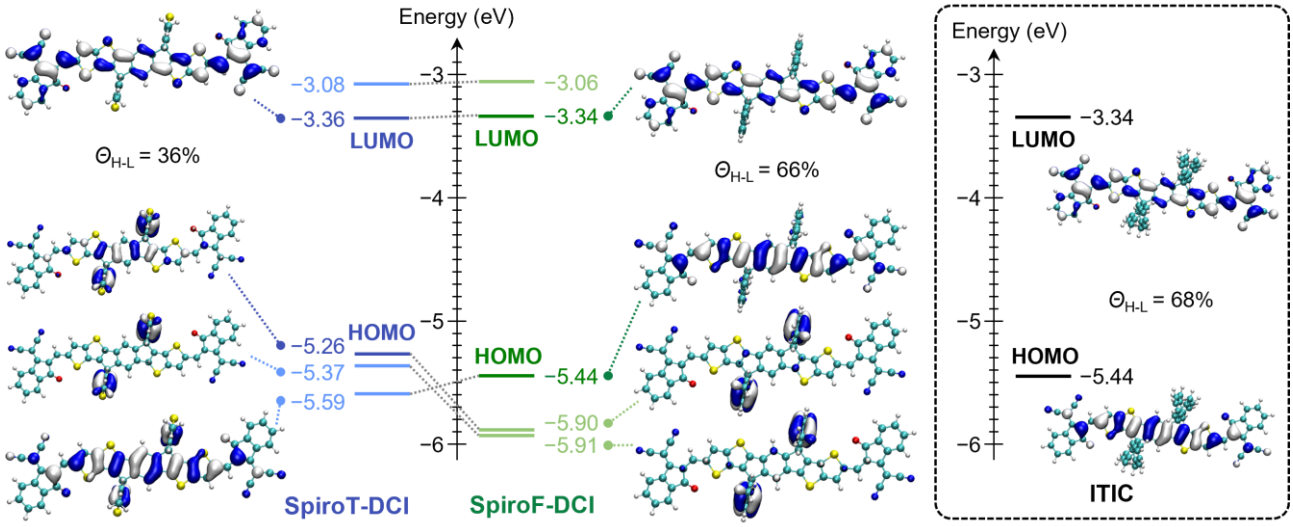

Figure 3.2. Distribution and energy level of molecular orbitals. $\Theta_{H\text{-}L}$ = the percentage of HOMO and LUMO overlap.

To gain insight into the effect that spiro-substituted units exert on electronic structures, theoretical calculations using DFT and TD-DFT methods were performed. Ground-state and excited-state geometries were optimized by B3LYP and ω-tuned ωB97XD functions, respectively, using a 6-31G(d,p) basis set.[20,21] As shown in **Figure S3.1**, the conjugated backbones of **SpiroT-DCI** and **SpiroF-DCI** showed similar planarity to that of ITIC. The bithiophene and biphenyl units in **SpiroT-DCI** and **SpiroF-DCI** are perpendicularly oriented to the indacenodithenothiophene (IDTT) backbone due to the sp^3 hybridized spiro carbon atom. As shown in **Figure 3.2**, **SpiroF-DCI** and ITIC showed overlapped HOMO/LUMO distributions on the IDTT backbone. By contrast,

SpiroT-DCI exhibited detached HOMO/LUMO distributions with the HOMO localized mainly on the bithiophene and the LUMO localized on the IDTT and dicyanomethylideneindanone (DCI) terminal units. In addition, **SpiroT-DCI** showed a much lower HOMO and LUMO overlap ($\Theta_{H\text{-}L}$) of 36% than that of 66% for SpiroF-DCI and 68% for ITIC. The different HOMO distributions between **SpiroT-DCI** and **SpiroF-DCI** stem from the difference in the HOMO energy levels of bithiophene and biphenyl: The HOMO energy level of bithiophene is shallower than that of the ITIC backbone, whereas biphenyl possesses a deeper HOMO energy than that of the ITIC backbone. As a result, the electron orbital distribution corresponding to the HOMO of **SpiroF-DCI** appeared at the HOMO−2 of **SpiroT-DCI**. Reflecting this HOMO distribution, the HOMO energy level (E_{HOMO}) of **SpiroT-DCI** was calculated to be −5.26 eV, which is obviously upshifted compared with those of **SpiroF-DCI** (−5.44 eV) and ITIC (−5.46 eV). On the other hand, the LUMO energy levels (E_{LUMO}) for these compounds are almost identical values of around −3.35 eV.

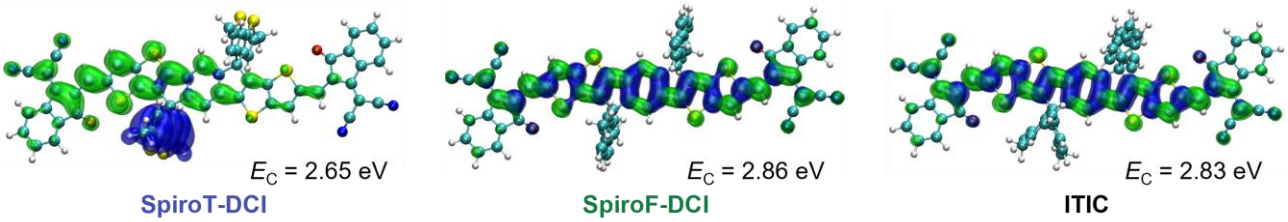

Figure 3.3. Distributions of the hole (blue) and electron (green) for S_1 state.

To further understand the difference in electronic structure caused by structural variations, the hole and electron distributions for the S_1 state were analysized. **Figure 3.3** shows the isosurfaces of the hole and electron distributions in the S_1 state.[21,22] Notably, the hole and electron of **SpiroT-DCI** were separately populated on the bithiophene units and on the IDTT backbone, respectively. By contrast, both the hole and the electron of **SpiroF-DCI** and ITIC dominantly populated the IDTT backbone. The distance between hole and electron centroids was calculated to be 3.612 Å for **SpiroT-DCI**, 0.002 Å for **SpiroF-DCI**, and 0.052 Å for ITIC, indicating that **SpiroT-DCI** forms S_1 state with larger R compared to the other compounds. These results indicate that the exciton in the S_1 of **SpiroT-DCI** is more favorable to the formation of a CT state rather than a LE state. Furthermore, the Coulomb attraction energies (E_C) based on these distributions for **SpiroT-DCI**, **SpiroF-DCI**, and ITIC were calculated to be 2.65, 2.86 and 2.83 eV, respectively.[23] The apparently smaller E_C for **SpiroT-DCI** suggests that charge separation in the excited state might be more facile compared with that of either **SpiroF-DCI** or ITIC, which is likely beneficial for the photon-to-current conversion process in OSCs.

3.3 Synthesis of compounds

The synthetic routes to **SpiroT-DCI** and **SpiroF-DCI** are shown in **Scheme 3.1**. The starting material **1** was prepared using a previously reported procedure.[24] Compound **2a** was obtained in a 65% yield via the nucleophilic addition of a lithiated bithiophene derivative of **1**. Treatment of compounds **2a** with boron tribromide (BBr_3) gave **SpiroT** in an 86% yield. In this cyclization reaction, after condition screening, the BBr_3/dichloromethane system obtained the highest yield, while other classic dehydration condensation conditions such as H_2SO_4 or HCl/AcOH or

PPA, etc., could only obtain a yield of less than 20%. The formylation of **2a** afforded **SpiroT-CHO**, which was subjected to Knoevenagel condensation with 1-(dicyanomethylene)-3-indanone to give **SpiroT-DCI**. Compound **SpiroF-DCI** was synthesized in the same manner. Due to the presence of 2-ethylhexyl groups, both compounds showed sufficient solubility in typical process solvents such as 1,2-dichlorobenzene, chlorobenzene, and chloroform.

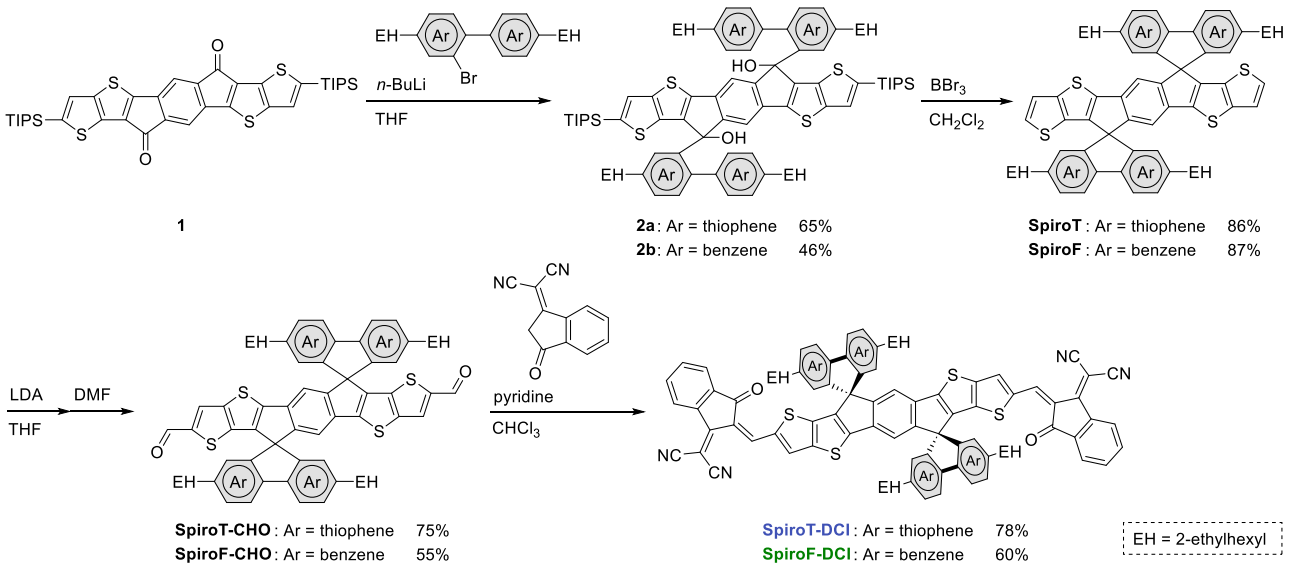

Scheme 3.1. Synthetic routes to **SpiroT-DCI** and **SpiroF-DCI**.

The thermal properties of **SpiroT-DCI** and **SpiroF-DCI** were evaluated using thermogravimetric analysis (TGA) under a nitrogen atmosphere. As shown in **Figure 3.4**, the thermal decomposition temperatures (T_d) at a 5% weight loss of **SpiroT-DCI** and **SpiroF-DCI** are 319 and 338 °C, respectively. These T_d values indicate that these compounds possess sufficient thermal stabilities for application to OSCs.

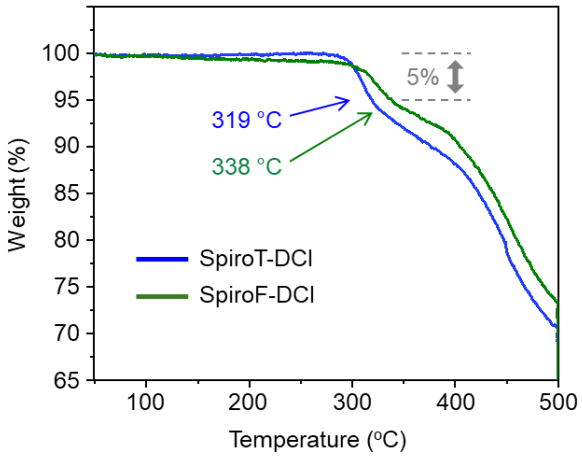

Figure 3.4. TGA profiles of **SpiroT-DCI** and **SpiroF-DCI**.

3.4 Single-crystal X-ray analysis

To understand the molecular interactions and packing difference from structural varieties, single-crystal X-ray diffraction measurements were performed. However, due to the high disorder of the branched side chains of 2-ethylhexyl, the single crystal data of both **SpiroT-DCI** and **SpiroF-DCI** was hard to obtain. Fortunately, complete single crystal data of **SpiroT-DCI** from a harsh condition of −30 °C was obtained. As shown in **Figure 3.5**, the distance of the S···O interaction was found to be 2.75 Å. From the side view, the **SpiroT-DCI** molecule showed a generally planar structure with a distortion around 21° for the DCI unit. In addition, as shown in **Figure S3.2**, the π–π stacking distance was found to be 3.39 and 3.48 Å. The distance between the S···S atom in the spiro-bithiophene groups in the two closest molecules is about 3.63 Å, which suggests that there exist weak intermolecular interactions between the flat side chain groups in **SpiroT-DCI**. Interestingly, **SpiroT-DCI** and **SpiroF-DCI** exhibit a V-type stacking mode at room temperature, and the corresponding raw single crystal packing diagram are shown in **Figure S3.3**.

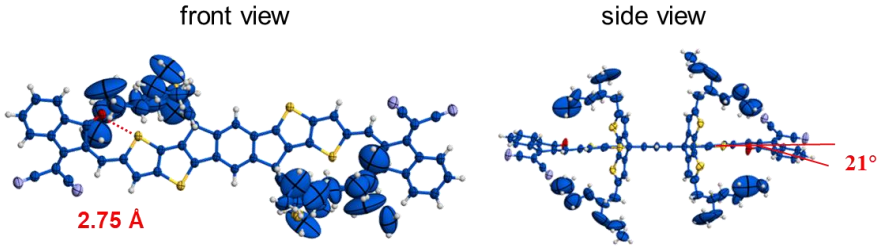

Figure 3.5. Configurations of **SpiroF-DCI** monomer in single crystal data from front and side views.

3.5 Electrochemical and photophysical properties

The electrochemical properties of **SpiroT-DCI** and **SpiroF-DCI**, as well as reference compound ITIC, were investigated using DPV. As shown in **Figure 3.6a**, these molecules exhibited a similar reduction pattern, where the first reduction peaks of **SpiroT-DCI**, **SpiroF-DCI**, and ITIC were 0.95, 0.95, and 0.92 V, respectively, vs. the Fc/Fc^+ couple. As shown by the oxidation peaks in **Figure 3.6b**, **SpiroT-DCI** (0.56 V) possesses a lower oxidation potential than that of either **SpiroF-DCI** (0.74 V) or ITIC (0.76 V). The E_{HOMO} and E_{LUMO} values of **SpiroT-DCI**, **SpiroF-DCI**, and ITIC were calculated from the oxidation and reduction peaks to be −5.37/−3.83, −5.54/−3.83, and −5.54/−3.85 eV, respectively. These parameters are summarized in **Table 3.1**. These values are qualitatively consistent with the DFT results shown in **Figure 3.2**, and experimentally demonstrate the upshifted HOMO energy level of **SpiroT-DCI**.

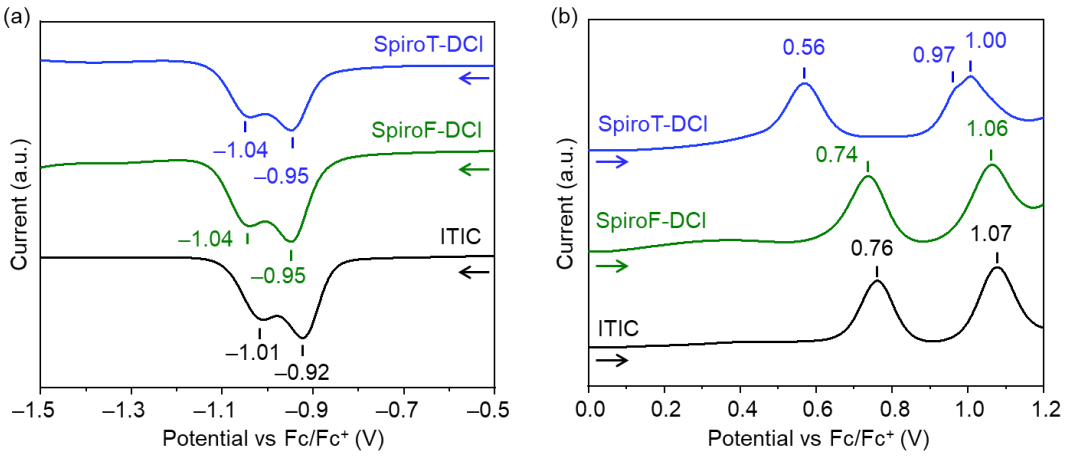

Figure 3.6. DPVs of **SpiroT-DCI**, **SpiroF-DCI**, and ITIC for (a) negative and (b) positive scans in acetonitrile containing 0.1 M $TBAPF_6$.

Table 3.1. Physical properties of **SpiroT-DCI**, **SpiroF-DCI**, and ITIC.

Compounds	λ_{max}^{sol} (nm)[a]	λ_{max}^{film} (nm)	λ_{onset}^{film} (nm)	E_g^{opt} (eV)[b]	E_{HOMO} (eV)[c]	E_{LUMO} (eV)[c]	IP (eV)[d]	EA (eV)[e]	E_b (eV)
SpiroT-DCI	693	709	785	1.58	–5.37	–3.83	5.75	3.85	0.32
SpiroF-DCI	680	695	764	1.62	–5.54	–3.83	5.88	3.86	0.40
ITIC	679	697	765	1.62	–5.54	–3.85	5.88	3.85	0.41

[a] Measured in chloroform solution. [b] E_g^{opt} was calculated using the equation: 1240 / λ_{onset}^{film}. [c] Values obtained from DPV. [d] Estimated from PYS. [e] Determined by LEIPS.

Low-energy inverse photoemission spectroscopy (LEIPS)[25-27] and photoelectron yield spectroscopy (PYS)[28] were conducted to determine the electron affinity (EA) and ionization energy (IE) of **SpiroT-DCI**, **SpiroF-DCI**, and ITIC in films. As shown in **Figures 3.7a** and **3.7b**, the EA values of these molecules were similar — approximately 3.85 eV. The IE values for **SpiroT-DCI**, **SpiroT-DCI**, and ITIC were found to be 5.75, 5.88 and 5.88 eV, respectively (**Table 3.1**). This result indicates that the presence of the bithiophene units could effectively raise the HOMO energy level while leaving the LUMO energy level unaffected, which is consistent with the electrochemical results and DFT calculations. The cyclic voltammograms (CV) in solid state were also measured to check the energy levels. As shown in **Figure S3.4**, the oxidation and reduction potentials of **SpiroT-DCI**, **SpiroF-DCI**, and ITIC were determined to be −5.44/−3.90, −5.63/−3.91, and −5.66/−3.93 eV, respectively. The trend is similar to LEIPS and PYS measurements. Based on the EA value of 3.18 eV for PBDB-T determined by the same method (**Figure S3.5**), the EA offsets between these NFAs and PBDB-T were calculated to be around 0.7 eV, which meets the energy level offset requirement for efficient charge separation at D/A interfaces.[29,30]

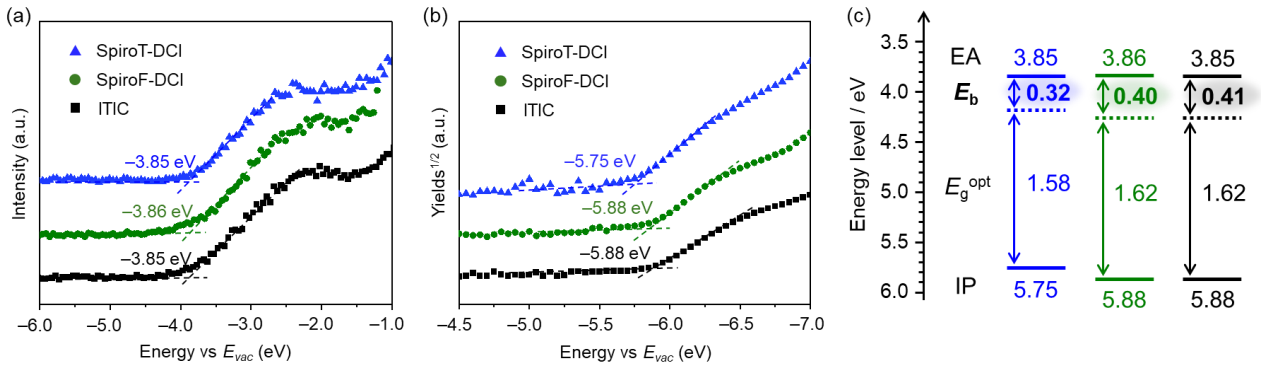

Figure 3.7. (a) LEIPS and (b) PYS of **SpiroT-DCI**, **SpiroF-DCI**, and ITIC in thin film state. (c) Energy level diagrams of **SpiroT-DCI**, **SpiroF-DCI**, and ITIC.

The UV-vis absorption spectra of **SpiroT-DCI**, **SpiroF-DCI**, and ITIC in chloroform solutions and films appear in **Figure 3.8**. In the solution spectra, **SpiroF-DCI** and ITIC showed absorption bands at almost an identical wavelength with maximum absorption peaks (λ_{max}^{sol}) at 680 and 679 nm, respectively. By contrast, **SpiroT-DCI** exhibited a red-shifted absorption band with a λ_{max}^{sol} at 693 nm. The molar extinction coefficients (ε) of **SpiroT-DCI**, **SpiroF-DCI**, and ITIC were found to be 1.40×10^5, 1.95×10^5, and 2.12×10^5 L mol^{-1} cm^{-1}, respectively. The relatively smaller ε value for **SpiroT-DCI** was consistent with the TD-DFT results (**Table S3.1**). All the compounds in films exhibited a red-shift of more than 15 nm, indicating the appearance of intermolecular interactions in the solid state. The optical energy gap (E_g^{opt}) based on the onset of the absorption spectra in films was estimated to be 1.58 eV for **SpiroT-DCI**, 1.62 eV for **SpiroF-DCI**, and 1.62 eV for ITIC (**Table 3.1**). As shown in **Figure S3.6**, the photoluminescence (PL) spectra of **SpiroT-DCI** exhibited lower PL intensities compared with those of either **SpiroF-DCI** or ITIC in both solutions and films. The Stoke's shifts of **SpiroT-DCI**, **SpiroF-DCI**, and ITIC in solution were calculated to be 930, 820, and 820 cm^{-1}, respectively. The observed phenomena of **SpiroT-DCI** are explained as typical characteristics of CT excited states.[31-33]

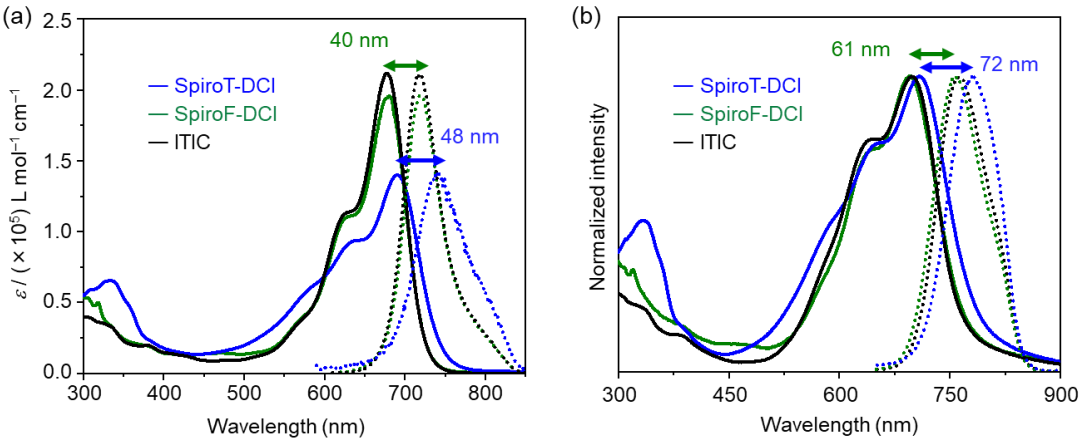

Figure 3.8. UV-vis absorption spectra (solid lines) and fluorescence spectra (dotted lines) of of **SpiroT-DCI**, **SpiroF-DCI**, and ITIC in chloroform solutions (a) and films (b). Fluorescence spectra are unified to the same intensity as the absorption spectra for direct comparison.

Based on the EA, IE, and E_g^{opt} values, the E_b values for **SpiroT-DCI**, **SpiroF-DCI**, and ITIC in films were estimated by **Eq. (1.1)**:

$$E_b = IE - EA - E_g^{opt}$$

As shown in **Figure 3.7c**, **SpiroT-DCI** possesses a smaller E_b value of 0.32 eV compared with that of either **SpiroF-DCI** (0.40 eV) or ITIC (0.41 eV). This qualitatitve trend was consistent with the calculated E_C values (**Figure 3.3**). This result indicates that excitons derived from **SpiroT-DCI** tend to form a charge-separated state, making the CT state more favorable. This is beneficial for accelerating the photon-to-current conversion.

3.6 Photovoltaic properties

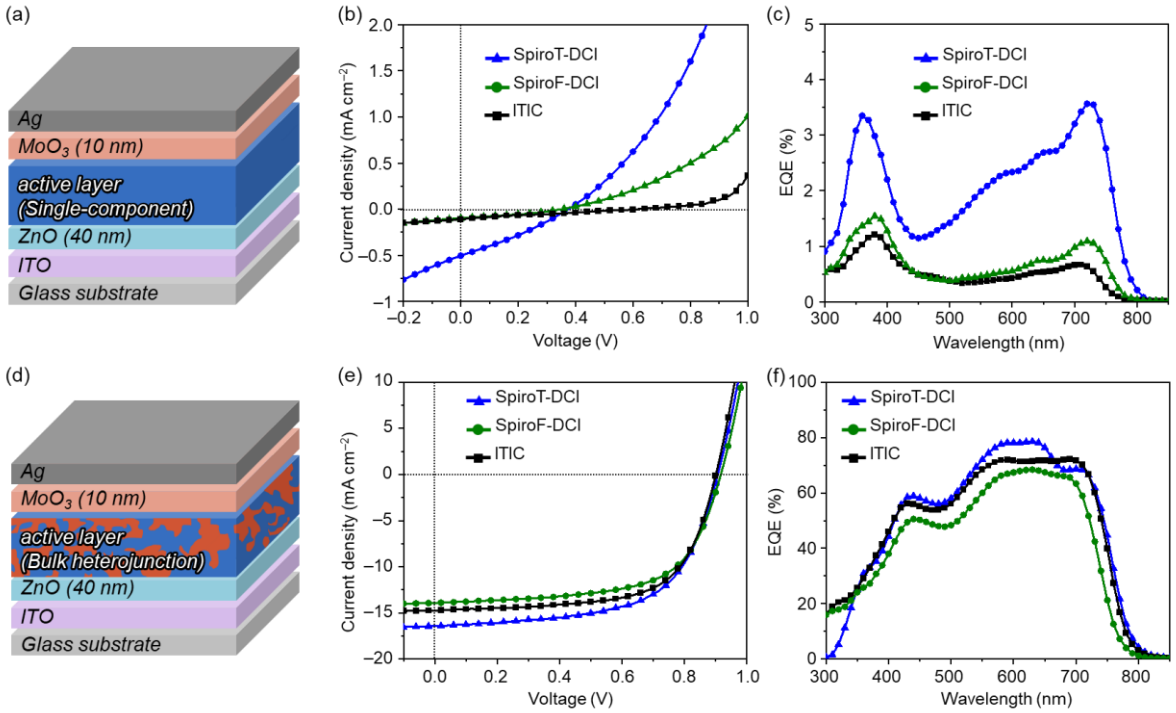

Figure 3.9. (a) Device structure, (b) *J–V* curves, and (c) EQE spectra for SC-OSC devices. d) Device structure, (e) *J–V* curves, and (f) EQE spectra for BHJ-OSC devices.

To examine the influence of the E_b values on device performance, we first investigated the photon-to-current conversion function using SC-OSC devices by utilizing **SpiroT-DCI**, **SpiroF-DCI**, or ITIC as the active layer (**Figure 3.9a**). The current *J–V* characteristics of SC-OSCs under an air mass of 1.5G using a solar simulator lamp (100 mW cm^{-2}) are shown in **Figure 3.9b**. The SC-OSCs based on **SpiroT-DCI** showed a PCE of 0.06% with a J_{SC} of 0.51 mA cm^{-2}. By contrast, a **SpiroF-DCI**- and ITIC-based device showed significantly lower PCE and J_{SC} values (**Table S3.2**). As shown in **Figure 3.9c**, the EQE_{max} of **SpiroT-DCI** was found to be 3.6%, which is higher than those of **SpiroF-DCI** (0.7%), ITIC (0.6%), or Y6-4O (1.4%).[17] This result indicates that **SpiroT-DCI** has a higher level of photocarrier generation characteristics, compared with those of either **SpiroF-DCI** or ITIC.

The photovoltaic characteristics of BHJ-OSCs with **SpiroT-DCI** and **SpiroF-DCI** as acceptors were investigated using an inverted configuration of ITO/ZnO/PBDB-T[34] (CAS Registry No. 1415929-80-4):acceptor/MoO_3/Ag

(**Figure 3.9d**), where the donor polymer of PBDB-T was selected due to its complemental absorption with these acceptors. The details of the fabrication conditions and device characteristics are provided in **Tables S3.3–S3.7**. **Figure 3.9e** shows the *J–V* characteristics of the best-performing BHJ-OSCs, and the key OSC parameters are summarized in **Table 3.2**. The best PCEs of the PBDB-T:**SpiroT-DCI**, PBDB-T:**SpiroF-DCI**, and PBDB-T:ITIC films were 9.08, 8.28, and 8.62%, respectively. As expected, the PBDB-T:**SpiroT-DCI**-based device showed a higher PCE value compared with those of either PBDB-T:**SpiroF-DCI** or PBDB-T:ITIC, which was due mainly to the increased J_{SC}. The EQE spectra of the PBDB-T:**SpiroT-DCI**-based device showed EQE responses between 400 and 800 nm, which were higher than those of PBDB-T:**SpiroF-DCI** and PBDB-T:ITIC. The PBDB-T:**SpiroT-DCI**-based device attained an EQE_{max} of 79% at 630 nm (**Figure 3.9f**). The integrated current densities from the EQE curves match well with the integrated current density values from the *J–V* tests (within a 5% error range), which indicates the good accuracy and reliability of the proposed performance parameters. These results indicate that **SpiroT-DCI** has potential for use as an organic semiconductor for OSCs.

Table 3.2. BHJ-OSC characteristics of **SpiroT-DCI**, **SpiroF-DCI**, and ITIC.

Active layer	PCE (%)	J_{SC} (mA cm^{-2})	V_{oc} (V)	FF (%)	EQE_{max} (%)
PBDB-T:**SpiroT-DCI**	9.08 (8.93 ± 0.13)	16.39 (16.47 ± 0.29)	0.91 (0.90 ± 0.01)	61 (60 ± 1)	78.6
PBDB-T:**SpiroF-DCI**	8.04 (7.78 ± 0.16)	13.93 (13.34 ± 0.39)	0.92 (0.92 ± 0.00)	63 (63 ± 1)	68.4
PBDB-T:ITIC	8.62 (8.41 ± 0.13)	14.73 (14.33 ± 0.28)	0.90 (0.90 ± 0.01)	65 (65 ± 1)	72.2

The values in parentheses indicate the mean and standard deviation of five independent devices in **Tables S3.5–S3.7**.

To estimate the hole and electron mobilities of the blend films, the space-charge limited current (SCLC) was investigated.[35-37] The *J–V* characteristics for the PBDB-T:**SpiroT-DCI**, PBDB-T:**SpiroF-DCI**, and PBDB-T:ITIC films are shown in **Figure S3.7**. Based on Child's law, the hole and electron mobilities (μ_h and μ_e) were calculated and are listed in **Table S3.8**. The relatively small differences between μ_h and μ_e among blend films indicate that the carrier transport characteristics make only limited contributions to the photocurrent.

To investigate the exciton dissociation and charge generation efficiencies of BHJ-OSCs, the J_{ph} against the V_{eff} were plotted.[38,39] As shown in **Figure S3.8**, the J_{ph} for the PBDB-T:**SpiroT-DCI**-based device was higher than that of either the PBDB-T:**SpiroF-DCI** or PBDB-T:ITIC devices, indicating that the overall photo-charge generation efficiency for PBDB-T:**SpiroT-DCI** was higher than that of the other blend films. The J_{ph} showed saturation when V_{eff} exceeded ~1 V for all devices. Based on the equation $P_{coll} = J_{SC}/J_{sat}$, the charge carrier collection probabilities (P_{coll}) were estimated to be 84% for PBDB-T:**SpiroT-DCI**, 84% for PBDB-T:**SpiroF-DCI**, and 86% for PBDB-T:ITIC. The almost identical P_{coll} values indicate limited differences in the charge-transport and collection processes under short-circuit conditions.

The surface morphologies of the optimized PBDB-T:**SpiroT-DCI**, PBDB-T:**SpiroF-DCI**, and PBDB-T:ITIC films were investigated via atomic force microscopy (AFM). **Figure S3.9** shows that all the blend films exhibited a uniform and relatively smooth surface morphology, and lists arithmetical mean deviation (R_a) surface roughness values of 2.2, 1.7, and 2.0 nm for PBDB-T:**SpiroT-DCI**, PBDB-T:**SpiroT-DCI**, and PBDB-T:ITIC, respectively. The crystallinities were investigated using X-ray diffraction (XRD) measurements. As shown in **Figure S3.10**, all

the blend films exhibited weak diffraction peaks between 2θ = 4–5° (corresponds to a lattice spacing of 1.8–2.2 nm) in both out-of-plane and in-plane directions. The diffraction peaks approximate to the longitudinal length of the acceptor molecules, which indicates that all the blend films have an isotropic lamellar arrangement for acceptors.

To gain further insight into the arrangement of acceptors, molecular dynamics (MD) simulations were performed for **SpiroT-DCI**, **SpiroF-DCI**, and ITIC. The computational details of the MD simulations are provided in the SI. **Figure 3.10** shows the radial distribution functions (RDFs) between acceptor sites. The RDFs of **SpiroT-DCI**, **SpiroF-DCI**, and ITIC are similar. The large peaks at ~4 Å indicate the stacking between acceptor-acceptor (A-A) sites, which is consistent with previous studies of ITIC films.[40,41] Next, the distributions of the distances between electron-donating IDTT sites in the A-A stacking structures were analyzed (**Figure 3.10b**). The largest peaks at ~20 Å correspond to J-type molecular stacking, and indicate that J-type molecular stacking is dominant in **SpiroT-DCI**, **SpiroF-DCI**, and ITIC films. The short distance between donor sites corresponds to a V-type stacking structure. The distribution for ITIC is broader than those for either **SpiroT- DCI** or **SpiroF-DCI** due to the flexible side chains of ITIC. The rigid side chains of **SpiroT-DCI** and **SpiroF-DCI** preferably adopt a specific V-type stacking structure, which also reflected in the single crystal packing at room temerpature (**Figure S3.3**). The similar distribution between **SpiroT-DCI** and **SpiroF-DCI** indicates that the higher PCE of **SpiroT-DCI** could originate from the difference in electronic structures.

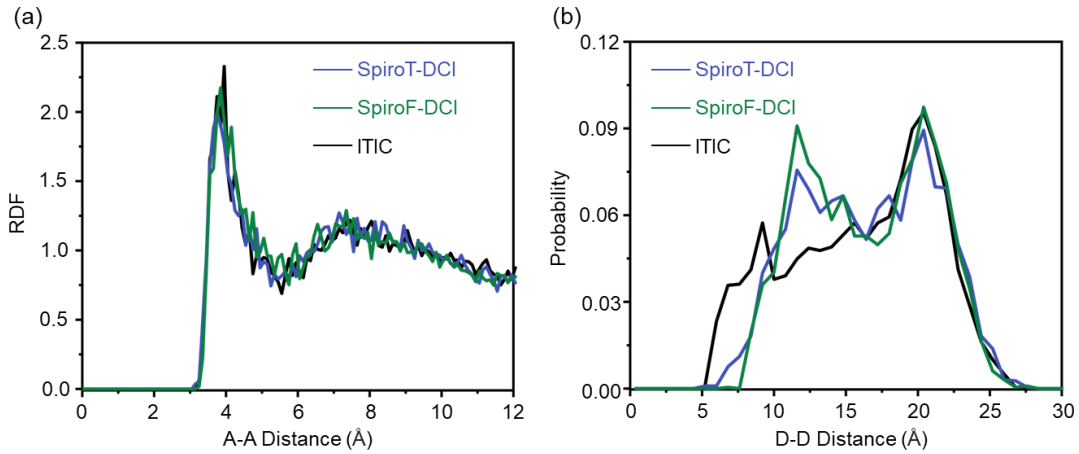

Figure 3.10. Results of MD simulations. (a) The radial distribution functions between acceptor-acceptor sites. (b) The distribution of electron-donating IDTT-IDTT distance in the acceptor-acceptor stacking structures.

3.7 Time-resolved analyses of exciton dynamics for pristine films

To elucidate the photoinduced responses of **SpiroT-DCI** and **SpiroF-DCI** relative to ITIC, transient IR absorption (TR-IR) measurements were conducted (**Figure 3.11** and **3.12**).[42,43] This method is particularly effective for studying intra- and inter-molecular charge transfer processes and for elucidating the behavior of free carriers that contribute to electrical conductivity. This effectiveness arises because intra- and inter-molecular charge transfer processes alter the local electron density within NFA molecules, which changes molecular vibrational frequencies such as those of cyano (CN) groups. Additionally, free carriers provide a broad, structureless absorption in the

infrared region. Therefore, TR-IR is a crucial tool for investigating intra- and inter-molecular charge transfer and the behavior of free carriers.

As shown in **Figure 3.11a**, the photoexcitation of a neat ITIC film leads to a negative peak at 2,225 cm^{-1} and two positive peaks at 2,205 and 2,175 cm^{-1}. Previously, our group has reported that the negative peak is associated with the ground state bleaching of parent CN groups, and the two positive peaks correspond to the S_1 state of ITIC and the anionic ITIC molecules resulting from intra- and inter-molecular charge separations, respectively.[18] The emergence of these red-shifts in CN indicates an increase in electron density around CN due to photoexcitation, and confirms that intermolecular charge separation occurs even in the absence of a donor layer.

Similar red-shifts were observed for **SpiroT-DCI** (**Figure 3.11b**), and although the relative peak intensities at 2,205 and 2,175 cm^{-1} differed significantly, the intensity of 2,175 cm^{-1} is markedly greater than that of 2,205 cm^{-1}, which suggests that intermolecular charge separation is more efficient in **SpiroT-DCI** compared with that in ITIC. Analogous results for **SpiroF-DCI** indicate that intermolecular charge separation also occurs (**Figure 3.11c**). However, the relative peak intensity at 2,175 cm^{-1} is considerably smaller than at 2,205 cm^{-1}, which indicates a less-frequent intermolecular charge separation in **SpiroF-DCI**, compared with that in either **SpiroT-DCI** or ITIC. By considering the peak intensity ratios of 2,175 to 2,205 cm^{-1}, the order for the efficiency of intermolecular charge transfer would be **SpiroT-DCI** > ITIC > **SpiroF-DCI**.

To examine how the E_b contributes to photoinduced charge-transfer and charge-separation kinetic behavior in pristine films, we observed time-resolved photoluminescence (PL) decay at room temperature. **Figure 3.13** shows the time-resolved PL spectra (a, c) and time profiles (b, d) for the **SpiroT-DCI** and **SpiroF-DCI** neat films, respectively. Although the PL spectrum shapes are similar between these NFAs, which is characteristic of broad CT band emissions, the PL intensity of the **SpiroT-DCI** film is much weaker than that of the **SpiroF-DCI** film, which indicates that the more efficient charge-separation may significantly reduce emissions following photoirradiation. Accordingly, the quicker PL decay in **SpiroT-DCI** (**Figure 3.13b**) than in **SpiroF-DCI** (**Figure 3.13d**) suggests efficient charge generation from the S_1 exciton. Based on the above transient absorption results (**Figure S3.11**) where free carriers are created in the pristine films, we performed analysis of the time-traces of the PL data as shown by the red lines in **Figure 3.13b** and **3.13d** by solving coupled-rate equations, as detailed in **Scheme 3.2** and Equation **S1**.

As listed in **Table 3.3**, the quicker decay in **SpiroT-DCI** (**Figure 3.13b**) is explained by k_{CS1} = 2.8 ns^{-1}, while the minor second decay component is rationalized by the thermally activated delayed fluorescence with k_{B2} = 0.7 ns^{-1}, which results in a free energy change of $\Delta G_{CS} = -0.07$ eV by using $\Delta G = -k_B T \cdot \ln(k_{CS1}/k_{B2})$. On the other hand, the single exponential decay in **Figure 3.13c** denotes that the CS rate constant is much smaller in **SpiroF-DCI** — estimated to be k_{CS1} = 0.3 ns^{-1} (**Table 3.3**). This is explained by the large exciton binding energy (0.40 eV) in **SpiroT-DCI** and is consistent with a small EQE in the SC-OSCs (**Figure 3.9c**). Overall, the exergonic CS behavior in the **SpiroT-DCI** neat film is consistent with the small E_b of 0.32 eV for the charge-generation in the neat film.

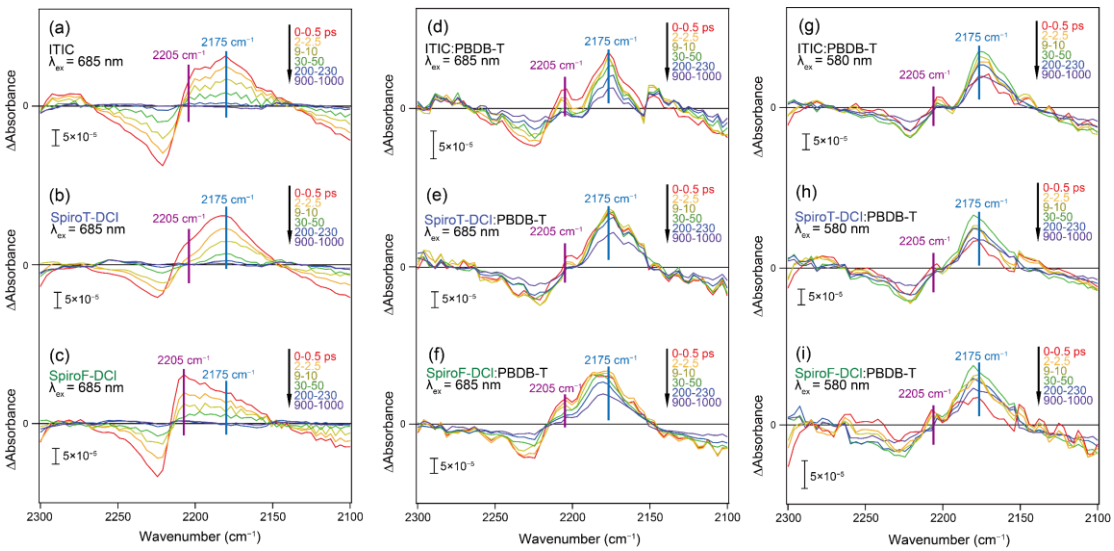

Figure 3.11. Pump-induced changes in the vibrational signatures of CN groups in NFAs. Panels (a–c) present the transient vibrational responses of pure ITIC, **SpiroT-DCI**, and **SpiroF-DCI** films upon 685 nm photoexcitation. In contrast, panels (d–f) illustrate the vibrational behavior of the NFA components within PBDB-T-based blend films under the same excitation wavelength. Selective excitation of the PBDB-T phase at 580 nm was performed for the samples shown in panels (g–i).

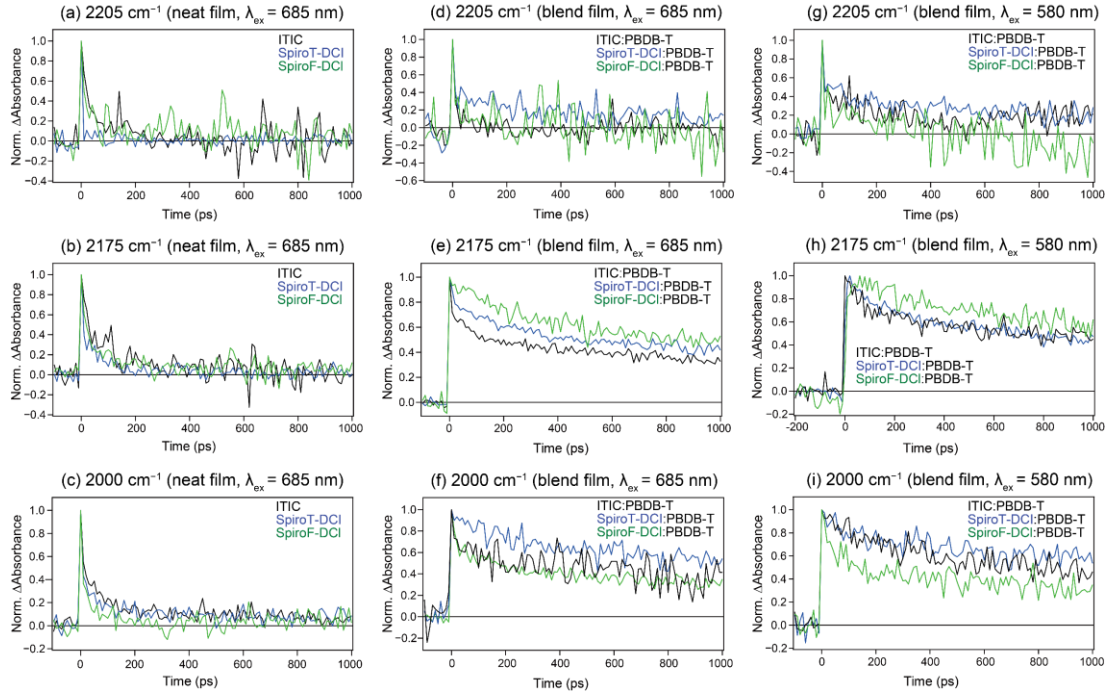

Figure 3.12. Time profiles for the locally excited (LE) state of NFAs, anionic NFAs, and free electrons in neat and blend films are presented. These profiles were obtained by photoexciting the neat NFA film with a 685 nm pump pulse and measuring at 2,205, 2,175, and 2,000 cm^{-1}, respectively (panels a–c). The NFA domain (panels d–f) and the PBDB-T domain (panels g ~ i) on the blend film with PBDB-T were also selectively photoexcited by a 685 nm and 580 nm pump pulses, respectively. The peak heights at 2,205 and 2,175 cm^{-1} were calculated after subtracting the broad absorptions by free electrons to extract the change of CN vibrations (**Figure 3.11**) and those of free electrons were estimated from **Figure S3.11**.

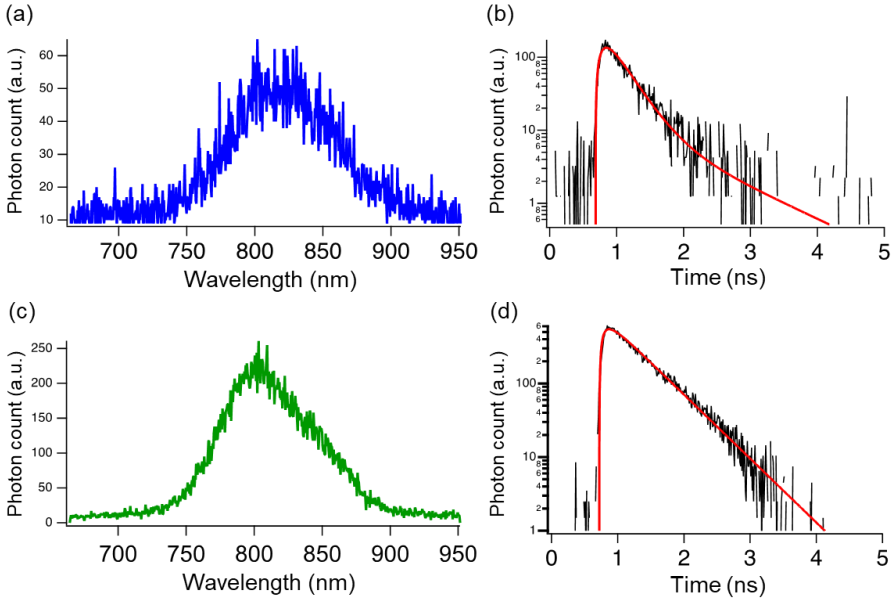

Figure 3.13. Time-resolved photoluminescence data of neat films of a,b) **SpiroT-DCI** and c,d) **SpiroF-DCI** obtained at room temperature. The spectra in the left panels were obtained by accumulating photon counts at 1 ns with a width of 200 ps.

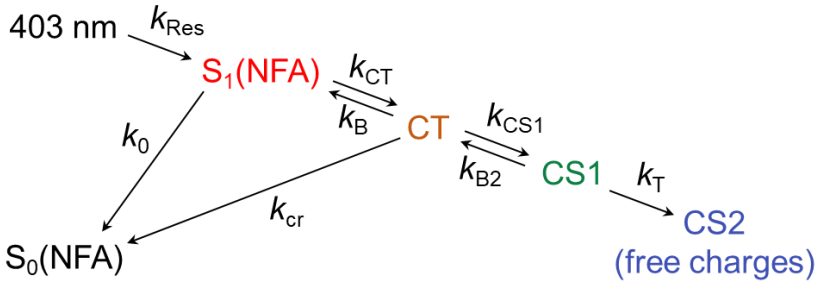

Scheme 3.2. Kinetic model for analyzing the transient PL profiles after the 403 nm light.

Table 3.3. Excited state kinetic parameters estimated for neat films of **SpiroT-DCI** and **SpiroF-DCI**.

Film	k_{CT} (ps^{-1})	k_B (ps^{-1})	k_{CS1} (ns^{-1})	k_{B2} (ns^{-1})	k_T (ns^{-1})
SpiroT-DCI	1.0	0.24	2.8	0.7	0.9
SpiroF-DCI	1.1	1.1	0.3	-	-

k_{Res} = 10 ns^{-1}, k_0 = 2.8 ns^{-1} and k_{CR} = 1.0 ns^{-1} are applied. See the experimental section.

3.8 Time-resolved analyses of exciton dynamics for blend films

TR-IR measurements were extended to the blend films with PBDB-T. In these experiments, only the acceptor molecules (ITIC, **SpiroT-DCI**, or **SpiroF-DCI**) were excited using 685 nm laser pulses. As shown in **Figure 3.11d**, two positive peaks appeared at 2,205 and 2,175 cm^{-1}, which is similar to the observations in pristine ITIC films.

However, the decay of the peak at 2,205 cm^{-1} is accelerated, and the lifetime of the peak at 2,175 cm^{-1} is extended. These findings indicate that intermolecular charge separation is more efficiently facilitated at the D/A interface.

Consistent observations were made for **SpiroT-DCI** and **SpiroF-DCI**, as shown in **Figure 3.11e** and **3.11f**. The lifetime of the peak at 2,175 cm^{-1} in these films also increased, further confirming the enhanced charge separation efficiency due to the formation of the D/A interface. This result suggests a more effective interaction and charge-transfer dynamics at the interfaces in blend films, compared with that in the pristine films of the acceptors.

The interfacial charge separation was further analyzed by photoexciting the PBDB-T donor layers with a 580 nm pump pulse and monitoring the C-N stretching mode in the NFA layers. In the PBDB-T:ITIC blend film, as illustrated in **Figure 3.11g**, a negative peak and a positive peak were observed at 2,225 cm^{-1} and 2,175 cm^{-1}, respectively, with a small shoulder at 2,205 cm^{-1}. The small peaks at 2,205 cm^{-1} are attributed to the partial photoexcitation of the ITIC layer by the 580 nm pump pulse. More critically, the presence of the 2,175 cm^{-1} peak confirms that electron injection occurs from the PBDB-T layer to the ITIC layer, which results in the formation of anionic ITIC molecules. Similar electron injections from the donor to acceptor layers were observed for **SpiroT-DCI** and **SpiroF-DCI**, which indicates that charge separation occurs at the D/A interface.

To better understand the decay kinetics of photoexcited charge carriers at the D/A interface, changes in intensity at 2,205; 2,175; and 2,300 cm^{-1} are presented in **Figure 3.12**. As shown in **Figure 3.12a**, the S_1 state of neat ITIC, which is induced by intramolecular charge transfer, exhibits an absorption peak at 2,205 cm^{-1} that diminishes within approximately 100 ps. The anionic ITIC state, which is characterized by an absorption peak at 2,175 cm^{-1}, also was diminished within ~100 ps (**Figure 3.12b**). However, via the formation of a heterojunction, its lifetime was extended — exceeding 1,000 ps (**Figure 3.12e**). This duration is notably longer than that observed in a neat ITIC film. These findings indicate that the formation of a donor/acceptor heterojunction extends the lifetime of the anionic ITIC state, by comparison with the S_1 state. A similar extension in lifetime for the anionic state is observed in **SpiroT-DCI** and **SpiroF-DCI**, with the lifetimes increasing on the order of **SpiroF-DCI** > **SpiroT-DCI** > ITIC. Comparable trends are noted for donor photoexcitation, where the lifetime sequence is **SpiroF-DCI** > **SpiroT-DCI** ≈ ITIC. However, the lifetime of these anionic states does not consistently correlate with the PCEs since anions do not participate directly in the charge-carrier transport that is necessary for current flow; instead, electrons remain bound within the molecules and thus are immobile. Conversely, free carriers, which are essential for generating photocurrent, can be analyzed by observing their broad, structureless absorption in the mid-IR region, particularly at 2,000 cm^{-1}, which is an absorption peak that is off-resonant to the C-N vibration. As depicted in **Figure 3.12c**, the lifetimes of free electrons generated by the photoexcitation of neat NFAs follow the order of **SpiroT-DCI** > ITIC > **SpiroF-DCI**. A similar sequence is observed for the blend films, where the lifetimes of photoexcited electrons in the NFAs follow the same order, regardless of whether the photoexcitation occurs in the acceptor (**Figure 3.12f**) or the donor (**Figure 3.12i**). The PCEs of the assembled BHJ-OSCs are ranked as **SpiroT-DCI** > ITIC > **SpiroF-DCI**, reflecting consistent results in the decay kinetics of free carriers. Consequently, the superior PCE of **SpiroT-DCI** could also be attributed to the prolonged lifetime of these free carriers.

3.9 Conclusion

In summary, to investigate the effect that the electronic structures of NFAs exert on the E_b and on OSC characteristics, novel ITIC-based NFAs with spiro-substituted bithiophene or biphenyl units as side groups were designed and synthesized. Theoretical calculations indicated that the HOMO and LUMO of **SpiroF-DCI** and ITIC are distributed in the main π-conjugated framework. By contrast, when electron-donating bithiophene units were introduced into **SpiroT-DCI**, they adopted a HOMO distribution, which led to detached HOMO and LUMO distributions. Electrochemical and photophysical measurements of **SpiroT-DCI** showed an upshifted HOMO energy level and a narrower E_g^{opt}, respectively, compared with those of **SpiroF-DCI** and ITIC. Based on the results of EA, IE, and E_g^{opt} in films, the **SpiroT-DCI** showed an E_b of 0.32 eV, which is smaller than that of either **SpiroF-DCI** (0.40 eV) or ITIC (0.41 eV). MD simulations indicated that **SpiroT-DCI** and **SpiroF-DCI** tend to adopt similar intermolecular configurations. Based on this result, the small E_b for **SpiroT-DCI** was attributed to the separated distribution of FMOs. This phenomenon shows that **SpiroT-DCI**-based SC-OSC were significantly improved compared with those of **SpiroF-DCI**- and ITIC-based devices. Furthermore, BHJ-OSCs based on PBDB-T and **SpiroT-DCI** achieved a maximum PCE of 9.08%. Time-resolved IR absorption spectroscopy and PL decay of the pristine films revealed that intermolecular charge separation of **SpiroT-DCI** is more efficient than that of **SpiroF-DCI**. In the time-resolved IR absorption spectroscopy measurements of the blend films with PBDB-T, **SpiroT-DCI** showed a lifetime of free carriers that was longer than that of either **SpiroF-DCI** or ITIC. These results demonstrate that tuning FMOs to increase the electron–hole distance in the molecule is an effective molecular design for reducing the E_b of organic semiconductors, which could pave the way to the development of higher-performing OSCs.

3.10 Experimental Section

Supplementary Figures

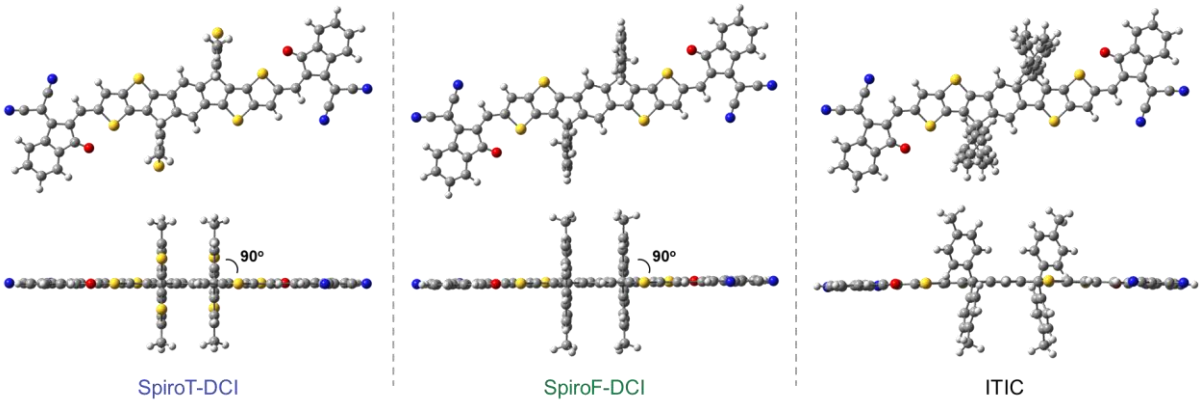

Figure S3.1. Optimized geometries of model structures for **SpiroT-DCI**, **SpiroF-DCI**, and ITIC.

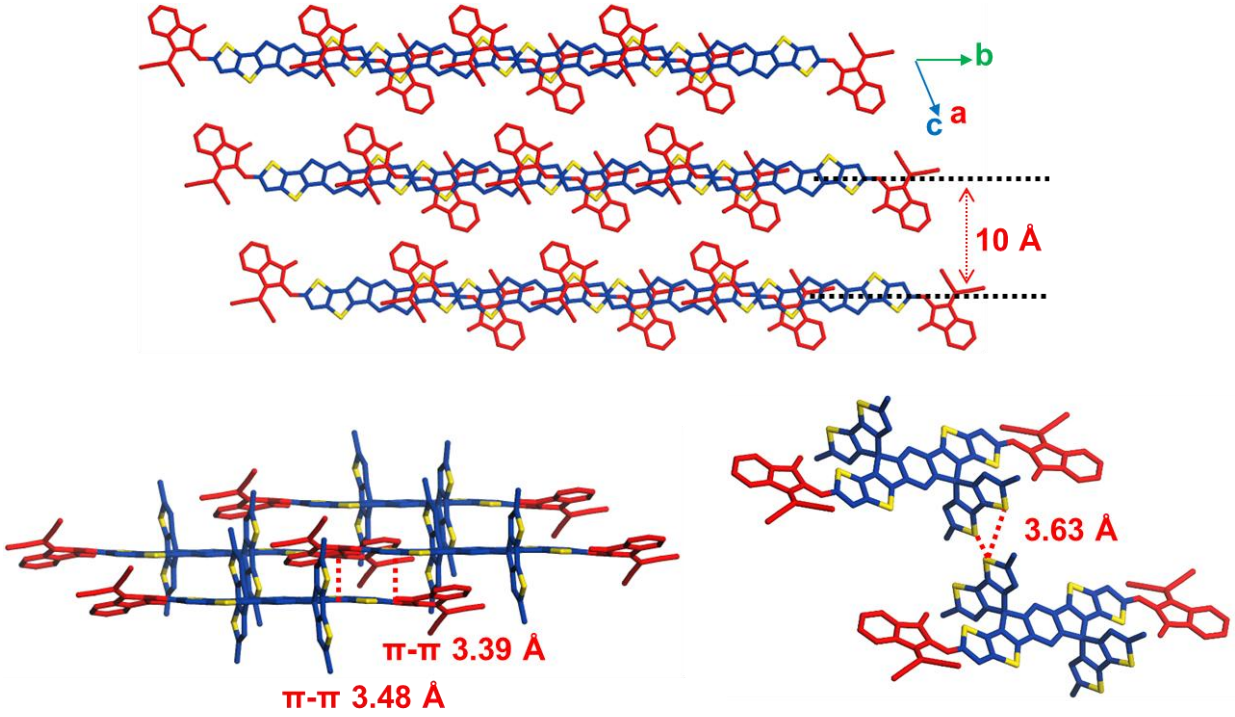

Figure S3.2. Single-crystal packing diagrams for **SpiroT-DCI**. All the side chains are removed or simplified for clarity. Key parameters for the crystal: $P\bar{1}$, a = 13.3059(5) Å, b = 14.0711(5) Å, c = 15.7650(6) Å, α = 70.235(4)°, β = 69.438(4)°, γ = 74.586(3)°, Z = 2, GooF = 1.076, R_1 = 7.68%, wR_2 = 25.12%.

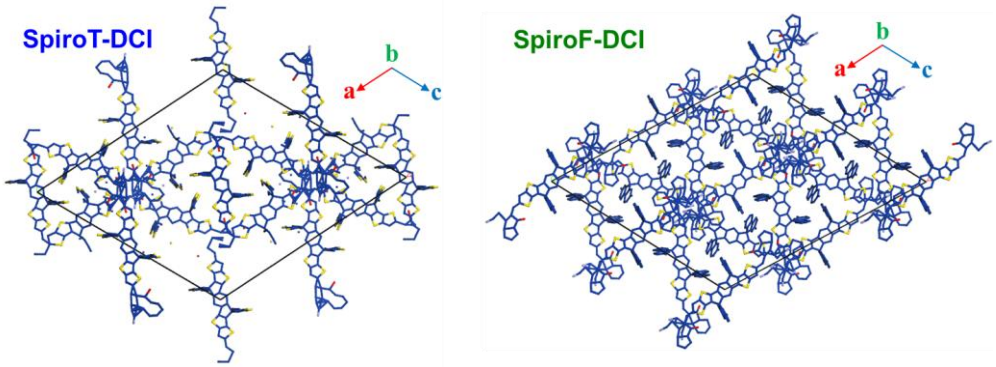

Figure S3.3. Single-crystal packing diagrams for **SpiroT-DCI** and **SpiroF-DCI** from the raw data by room temperature growth.

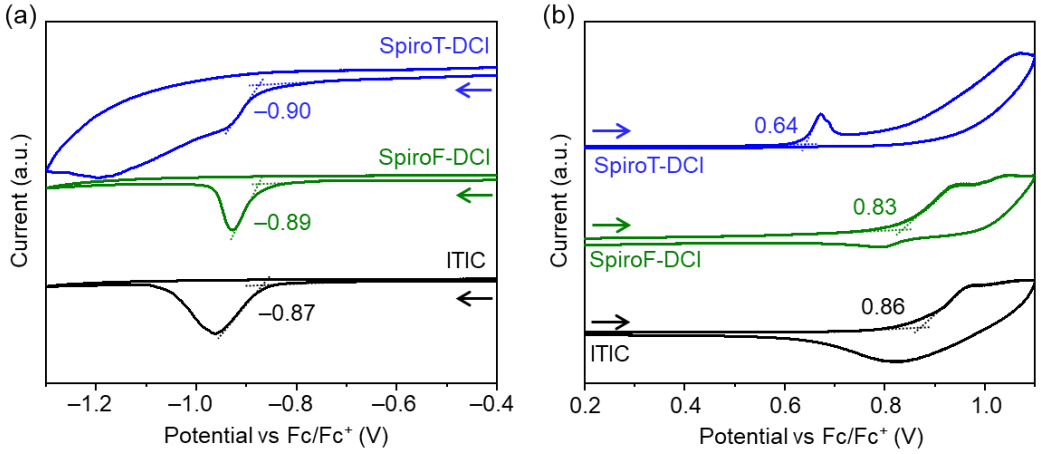

Figure S3.4. Cyclic voltammograms (CV) of **SpiroT-DCI**, **SpiroF-DCI**, and ITIC in the solid state for (a) negative and (b) positive scans in acetonitrile containing 0.1 M $TBAPF_6$.

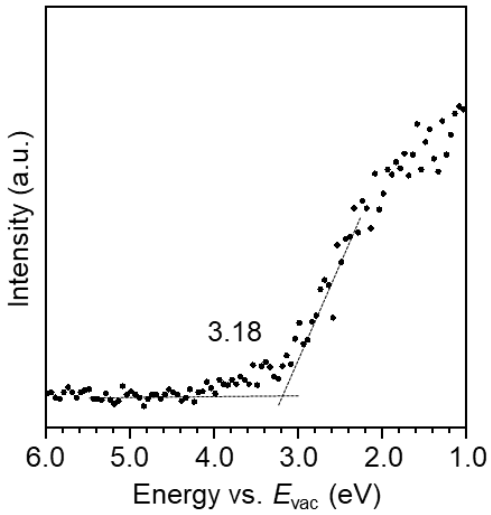

Figure S3.5. LEIPS of PBDB-T in pristine film.

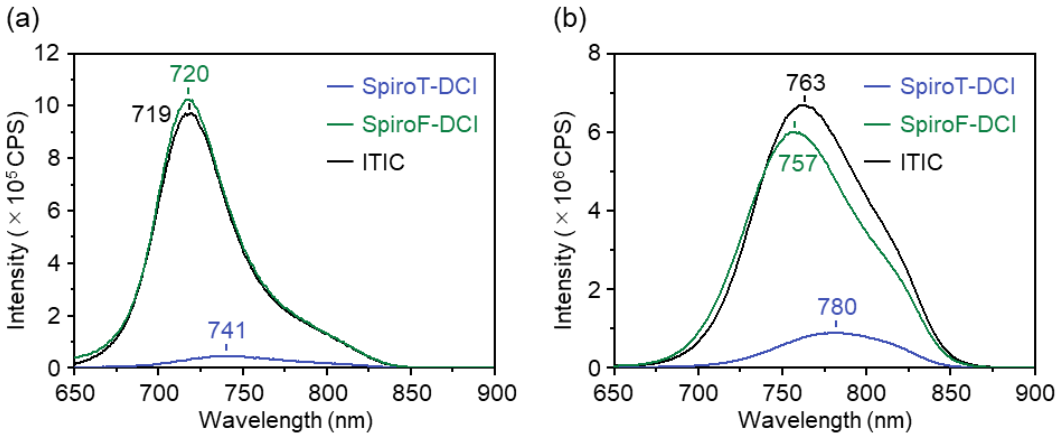

Figure S3.6. (a) Fluorescence spectra of **SpiroT-DCI**, **SpiroF-DCI**, and ITIC in 5 μM $CHCl_3$ solutions. Excitation wavelength is 580 nm for **SpiroT-DCI** and 600 nm for **SpiroF-DCI** and ITIC. The slit widths for excitation and detection were set to 4 nm. (b) Fluorescence spectra of films formed on quartz plate. Excitation wavelength is 600 nm for all the samples. The slit widths for excitation and detection were set to 10 nm.

Table S3.1. TD-DFT results and hole-electron analysis of singlet states.

	state	transition	E (eV)[a]	f[b]	D_idx (Å)[c]	Sr[d]	t_idx[e]	E_C (eV)
SpiroT-DCI	S1	HOMO → LUMO (81%) HOMO−1 → LUMO+1 (9%) HOMO → LUMO+2 (3%)	2.11	0.98	3.612	0.22	2.41	2.65
	S3	HOMO−2 → LUMO (79%) HOMO−3 → LUMO+1 (9%) HOMO−1 → LUMO+1 (5%)	2.43	2.66	–	–	–	–
SpiroF-DCI	S1	HOMO → LUMO (86%) HOMO−3 → LUMO+1 (7%)	2.28	3.41	0.006	0.76	−7.03	2.86
ITIC	S1	HOMO → LUMO (86%) HOMO−1 → LUMO+1 (9%)	2.28	3.52	0.052	0.77	−0.78	2.83

[a]Transition energy. [b]Oscilator strength. [c]The distance of hole-electron centroid. [d]Hole-electron overlap integral. [e]CT character.

Table S3.2. SC-OSC characteristics of **SpiroT-DCI**, **SpiroF-DCI**, and ITIC.

Active layer	PCE (%)	J_{SC} (mA cm^{-2})	V_{oc} (V)	FF (%)	EQE_{max} (%)
SpiroT-DCI	0.06	0.51	0.37	30	3.6
SpiroF-DCI	0.01	0.10	0.35	34	0.7
ITIC	0.02	0.11	0.62	25	0.6

Table S3.3. OSC fabrication conditions and characteristics of PBDB-T:**SpiroT-DCI**-based devices.

D:A[a]	solvent[b]	conc. / mg mL^{-1}	DIO / vol%	rotation / rpm	PCE / %	J_{sc} / mAcm^{-2}	V_{oc} / V	FF / %
1.5:1	CB	20	0.5	1000	4.85	11.71	0.89	46
1:1	CB	20	0.5	1000	5.99	12.39	0.89	54
1:1.5	CB	20	0.5	1000	5.36	11.58	0.89	52
1:1	DCB	20	0.5	1000	6.38	11.93	0.91	59
1:1	CF	10	0.5	1000	5.22	10.19	0.87	59
1:1	CB	20	-	1000	4.98	11.26	0.89	50
1:1	DCB	20	-	1000	5.65	10.68	0.91	58
1:1	CF	10	-	1000	6.33	12.20	0.90	57
1:1	CB	20	0.5	2000	7.10	12.81	0.89	62
1:1	DCB	20	0.5	2000	5.28	9.26	0.91	63
1:1	CB	30	0.5	2000	5.70	12.49	0.90	51
1:1	CB	30	0.5	3000	6.33	12.56	0.90	56
1:1	CB	30	0.5	4000	6.56	12.97	0.90	56
1:1	**CB**	**30**	**0.5**	**5000**	**8.82**	**16.67**	**0.89**	**59**
1:1	CB	25	0.5	5000	7.83	14.19	0.90	61
1:1	CB	35	0.5	5000	6.32	12.58	0.90	56
1:1	CB	40	0.5	5000	5.24	11.90	0.89	50

[a] Weight ratio of PBDB-T (D) and **SpiroT-DCI** (A). [b] Process solvent (CB = chlorobenzene, DCB = 1,2-dichlorobenzene, CF = chloroform). [b] Thermal annealing temperature under N_2 for 10 min.

Table S3.4. OSC fabrication conditions and characteristics of PBDB-T:**SpiroF-DCI**-based devices.

D:A[a]	solvent[b]	conc. / mg mL^{-1}	DIO / vol%	rotation / rpm	PCE / %	J_{sc} / mAcm^{-2}	V_{oc} / V	FF / %
1.5:1	CB	20	0.5	2000	6.62	12.71	0.92	57
1:1	CB	20	0.5	2000	7.55	13.37	0.92	62
1:1.5	CB	20	0.5	2000	5.28	12.07	0.87	50
1:1	DCB	20	0.5	2000	7.07	12.15	0.93	63
1:1	CF	10	0.5	2000	7.22	12.87	0.90	62
1:1	CB	20	-	2000	5.94	11.94	0.89	56
1:1	CB	20	0.5	3000	7.94	13.86	0.91	63
1:1	CB	20	0.5	4000	7.18	13.41	0.91	59
1:1	CB	20	0.5	5000	7.00	11.65	0.92	65
1:1	CB	15	0.5	3000	6.51	10.57	0.92	67
1:1	CB	25	0.5	3000	7.14	13.28	0.91	59

[a] Weight ratio of PBDB-T (D) and **SpiroF-DCI** (A). [b] Process solvent (CB = chlorobenzene, DCB = 1,2-dichlorobenzene, CF = chloroform). [b] Thermal annealing temperature under N_2 for 10 min.

Table S3.5. OSC characteristics of optimized PBDB-T:**SpiroT-DCI**-based devices.

Run	PCE / %	J_{SC} / mA cm^{-2}	V_{OC} / V	FF / %
1	9.05	16.22	0.90	62
2	8.76	16.15	0.89	61
3	8.82	16.67	0.89	59
4	8.95	16.92	0.89	59
5	**9.08**	**16.39**	**0.91**	**61**
average	8.93 ± 0.13	16.47 ± 0.29	0.90 ± 0.01	60 ± 1

Table S3.6. OSC characteristics of optimized PBDB-T:**SpiroF-DCI**-based devices.

Run	PCE / %	J_{SC} / mA cm^{-2}	V_{OC} / V	FF / %
1	7.66	12.99	0.92	64
2	7.90	13.46	0.92	64
3	7.72	13.49	0.92	62
4	7.59	12.85	0.92	64
5	8.04	13.93	0.92	63
average	7.78 ± 0.16	13.34 ± 0.39	0.92 ± 0.00	63 ± 1

Table S3.7. OSC characteristics of optimized PBDB-T:ITIC-based devices.

Run	PCE / %	J_{SC} / mA cm^{-2}	V_{OC} / V	FF / %
1	8.46	14.31	0.91	65
2	8.31	13.87	0.91	66
3	8.44	14.42	0.90	65
4	8.62	14.73	0.90	65
5	8.24	14.34	0.90	64
average	8.41 ± 0.13	14.33 ± 0.28	0.90 ± 0.005	65 ± 0.6

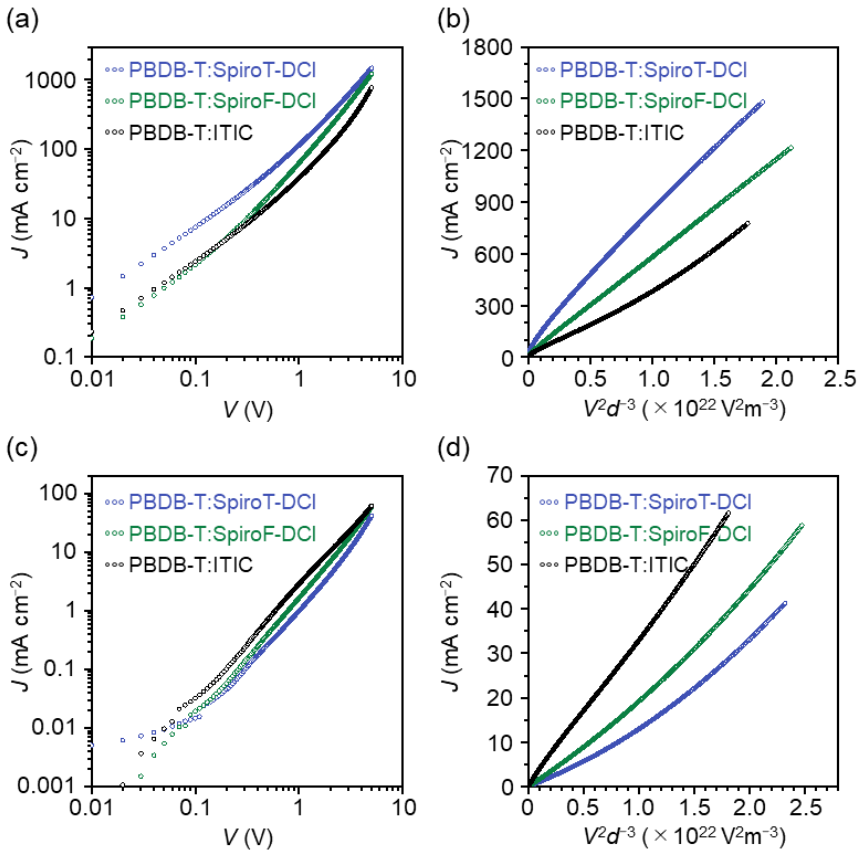

Figure S3.7. *J*–*V* plots and *J*–V^2d^{-3} plots for (a, b) hole only devices and (c, d) electron only devices.

Table S3.8. Hole and electron mobilities of the blend films.

D:A	μ_h (cm²/V·s)[a]	μ_e (cm²/V·s)[b]
PBDB-T:**SpiroT-DCI**	2.3×10^{-4}	7.7×10^{-6}
PBDB-T:**SpiroF-DCI**	1.9×10^{-4}	9.7×10^{-6}
PBDB-T:ITIC	1.8×10^{-4}	1.2×10^{-5}

[a] ITO/PEDOT:PSS/PBDB-T:acceptor/MoO_3/Ag. [b] ITO/ZnO/PBDB-T:acceptor/Ca/Ag.

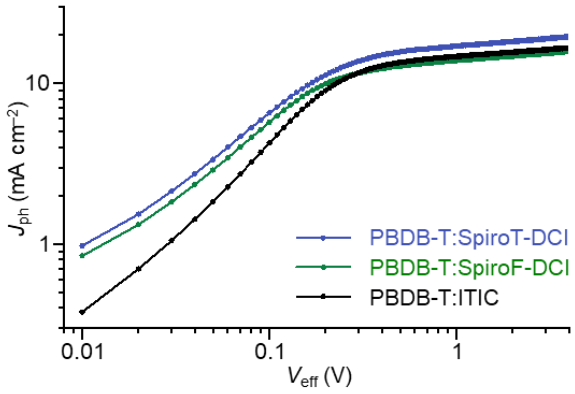

Figure S3.8. J_{ph} plotted against V_{eff} for the best BHJ-OSC devices.

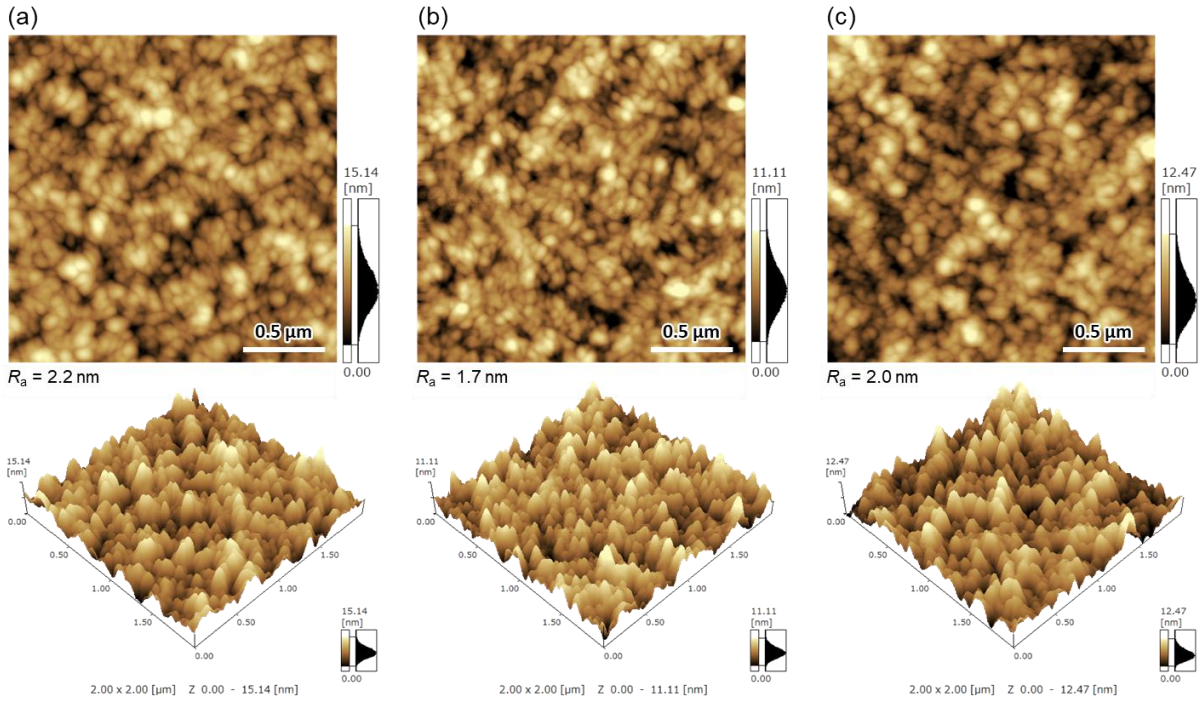

Figure S3.9. AFM height images of (a) PBDB-T:**SpiroT-DCI**, (b) PBDB-T:**SpiroF-DCI**, and (c) PBDB-T:ITIC blend films.

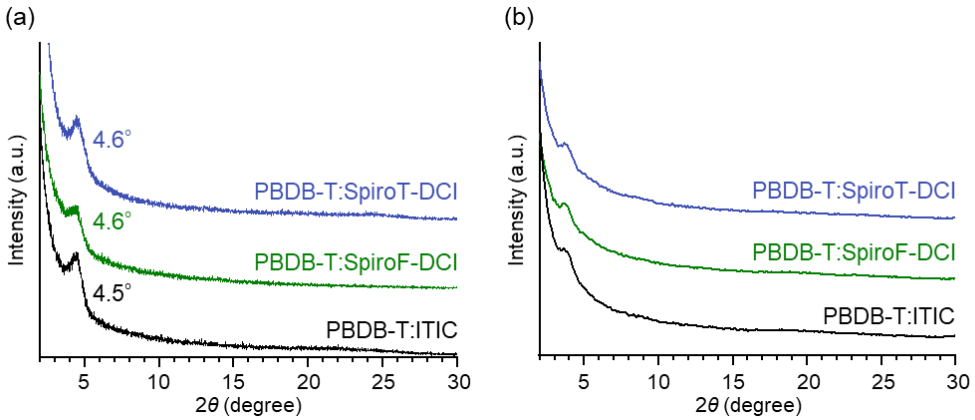

Figure S3.10. X-ray diffractograms of blend films for (a) out-of-plane and (b) in-plane scans.

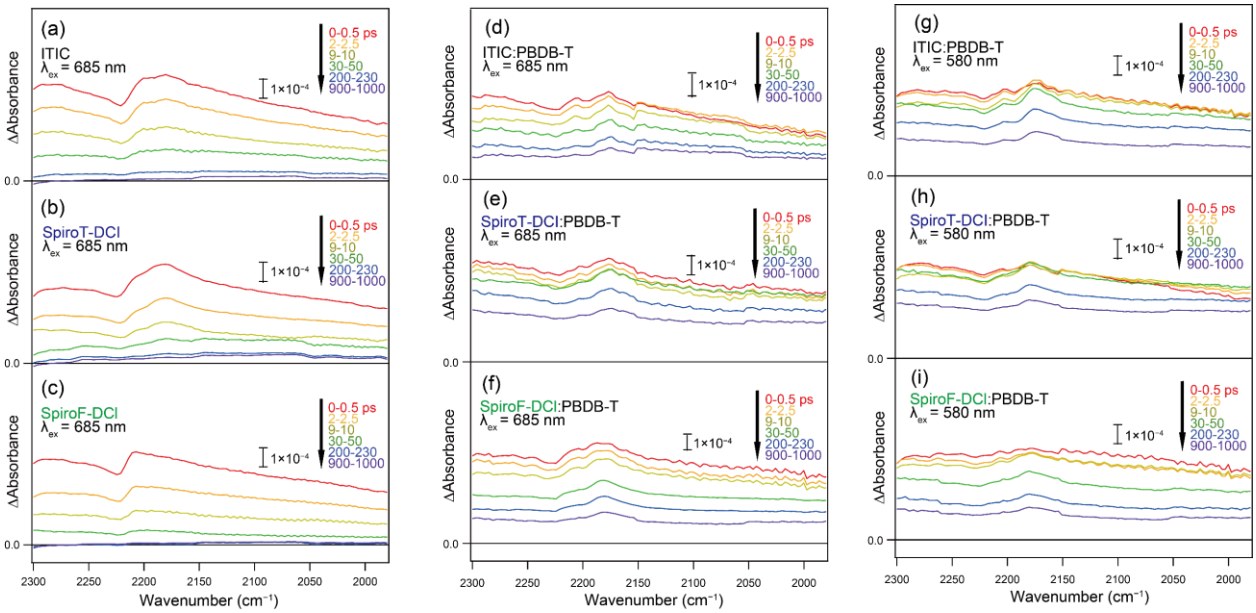

Figure S3.11. Transient IR spectra of NFAs under pulsed excitation. Panels (a–c) display the time-resolved IR spectra of neat ITIC, **SpiroT-DCI**, and **SpiroF-DCI** following excitation with a 685 nm pump pulse. Panels (d–f) show the corresponding signals from the NFA domains in PBDB-T-based blend films irradiated with the same excitation wavelength. In panels (g–i), the donor component PBDB-T is selectively excited using a 580 nm pump. Across both neat and blended samples, a broad absorption feature ranging from 2300 to 1950 cm^{-1} remains detectable even after the decay of the 2175 cm^{-1} peak at 1000 ps, indicating the presence of free charge carriers with lifetimes exceeding that of the charge-transfer (CT) state.

General information

Column chromatography was carried out using KANTO Chemical silica gel 60N (40–50 μm). Thin-layer chromatography was monitored under UV light. Preparative gel-permeation chromatography (GPC) was performed on a Japan Analytical Industry LC-918 system equipped with JAI-GEL 1HH/2HH columns. ^{1}H and ^{13}C NMR spectra were recorded on JEOL ECS-400 or ECA-600 spectrometers. Chemical shifts (δ) are reported in ppm with multiplicities indicated as s, d, t, m, or br, and coupling constants in Hz. Mass spectra were obtained using a Shimadzu GCMS-QP-5050 or AXIMA-TOF instrument. High-resolution mass spectra (HRMS) were measured by atmospheric pressure chemical ionization (APCI) on a Thermo Scientific LTQ Orbitrap XL. Thermogravimetric analysis (TGA) was performed on a Shimadzu TGA-50 under nitrogen at a heating rate of 10 °C min^{-1}. UV–vis absorption spectra were recorded with a Shimadzu UV-3600 spectrophotometer, and emission spectra were collected using a Fluoromax-4 spectrometer equipped with a Hamamatsu R928P photomultiplier in photon-counting mode. All spectroscopic measurements were performed in spectroscopic-grade solvents. PYS was performed using a Bunkoukeiki BIP-KV202GD system. LEIPS was carried out on a system from Ulvac-Phi, Inc. Surface morphology of organic films was examined by AFM using a Shimadzu SPM9600. Elemental analysis was conducted with a PerkinElmer LS-50B instrument by the Comprehensive Analysis Center (CAC), SANKEN, The University of Osaka.

Electrochemical measurements

Differential pulse voltammetry (DPV) and Cyclic voltammetry (CV) was performed in 1,2-dichlorobenzene (*o*-DCB)/acetonitrile (5:1 by volume ratio) containing 0.1 M tetrabutylammonium hexafluorophosphate ($TBAPF_6$) as a supporting electrolyte. All the voltammograms were recorded at a scan rate of 100 mV s^{-1} using a platinum disk as the working electrode, a platinum wire as the counter electrode, and an $Ag/AgNO_3$ as the reference electrode. The solid samples of **SpiroT-DCI**, **SpiroF-DCI**, and ITIC were fabricated onto the working electrode by drop-casting using 10 mg/mL solution in chloroform at ambient condition.

SC-OSC device and BHJ-OSC device fabrications and evaluations

SC-OSC and BHJ-OSC devices were fabricated using an inverted structure of ITO/ZnO/active layer/MoO_3/Ag.[44] ITO-coated glass substrates were sequentially cleaned by ultrasonication in acetone, deionized water, and 2-propanol for 15 min each, followed by ozone treatment for 1 h. A ZnO layer was deposited by spin-coating a precursor solution containing zinc acetate dihydrate (200 mg), ethanolamine (55 μL), and 2-methoxyethanol (2 mL) at 4000 rpm, followed by thermal annealing at 200 °C for 30 min in air. The active layer was spin-coated onto the ITO/ZnO substrate inside a nitrogen-filled glove box. MoO_3 (10 nm) and Ag (80 nm) top electrodes were thermally evaporated through a shadow mask under a vacuum of 10^{-5} Pa. Film thicknesses were monitored using a quartz crystal microbalance, and the device active area was defined as 0.09 cm^2. After encapsulation, the photovoltaic performance was evaluated under simulated AM 1.5G illumination (100 mW cm^{-2}) using a solar simulator (SAN-EI ELECTRIC, XES-301S). *J–V* characteristics were measured with a KEITHLEY 2400 source meter, and EQE spectra were acquired using a Soma Optics S-9240 system. Active layer thicknesses were determined by a KLA Tencor Alpha-step IQ profilometer.

X-ray diffraction measurements

X-ray diffraction (XRD) measurements were conducted using a Rigaku SmartLab diffractometer equipped with a zero-dimensional scintillation counter (SC-70), operating in Bragg–Brentano geometry with CuKα (λ = 1.5418 Å) at 45 kV and 200 mA. Out-of-plane and in-plane diffraction patterns were acquired using 2θ and $2\theta\chi$ scan modes, respectively, over the range of 2°-30°, with a step size of 0.02°, under a fixed grazing incidence angle (ω) of 0.2°.

SCLC measurements

Hole-only and electron-only devices were prepared with a structure of ITO/PEDOT:PSS/active layer/MoO_3/Ag and ITO/ZnO/active layer/Ca/Ag, respectively.[36,37] The active layers of PBDB-T:**SpiroT-DCI**, PBDB-T:**SpiroF-DCI**, and PBDB-T:ITIC were prepared using the optimized fabrication conditions for BHJ-OSCs. The carrier mobilities of these devices were calculated by the following equation:

$$J = \frac{9}{8}\varepsilon\varepsilon_0\mu\frac{V^2}{d^3}$$

where ε, ε_0, μ, and d are the dielectric constant of the active layer, the permittivity of free space, the carrier mobility, and the measured thickness of active layer, respectively. We used the values of $\varepsilon = 3$, $\varepsilon_0 = 8.8 \times 10^{-12}$.

Photocurrent density (J_{ph})–effective applied voltage (V_{eff}) plots

Photocurrent density (J_{ph})–effective applied voltage (V_{eff}) plots were measured using the best BHJ-OSCs of PBDB-T:**SpiroT-DCI**, PBDB-T:**SpiroF-DCI**, and PBDB-T:ITIC. The J_{ph} is calculated using the equation $J_{ph} = J_L - J_D$, where J_L and J_D are the current densities under illumination and dark conditions, respectively, whereas $V_{eff} = V_0 - V$, where V_0 is the compensation voltage, at which $J_{ph} = 0$ and V is the applied bias.[38,39]

Computational details of molecular dynamics (MD) simulations

The MD simulations were performed using the AMBER program package.[45] **SpiroT-DCI, SpiroF-DCI**, and ITIC were treated by the general AMBER force field. To obtain the film states, several steps of NPT-MD simulations were carried out as the previous studies.[40] First, 512 molecules were placed at equal intervals with random orientations in a cubic box with the periodic boundary condition. Next, an NPT-MD simulation for 30 ns was performed at 650 K and 1 atm. The Langevin thermostat and Berendsen barostat were used to control the temperature and pressure. Then, the temperature was gradually decreased from 650 K to 300 K at 1 atm in a 100-ns MD simulation. Finally, an NPT-MD simulation for 30 ns was performed at 1 atm and 300 K. The final structures of 10 independent MD simulations were employed for analysis of each molecule..

Transient absorption spectroscopy

Thin films for transient absorption (TA) measurements were prepared by drop-casting chloroform solutions of **SpiroT-DCI**, **SpiroF-DCI**, ITIC, and their 1:1 (w/w) blends with PBDB-T onto CaF_2 substrates. During measurement, the films were mounted in an IR cell filled with 20 torr of N_2. TA spectra were acquired using a pump–probe setup based on a Ti:sapphire regenerative amplifier (Spectra Physics, Solstice; 90 fs pulse width, 1 kHz repetition rate) coupled with optical parametric amplifiers (Spectra Physics, TOPAS Prime). The samples were photoexcited with 685 nm (acceptor excitation) or 580 nm (donor excitation) pump pulses at 2 μJ cm^{-2} per pulse and a repetition rate of 500 Hz. For mid-infrared (MIR) probing, the probe pulse was generated via difference frequency generation between the signal and idler outputs of the OPA in an $AgGaS_2$ crystal and detected using a 128-channel linear MCT array detector (Infrared Systems Development, FPAS-0144). Spectral analysis of the cyano (C-N) stretching region in the acceptors was performed after subtracting background signals attributed to free carrier absorption.

Time-resolved photoluminescence (PL) measurements and analysis of PL profiles

A streak scope C4334 with imaging spectrograph C5094 (Hamamatsu photonics, Ltd.) was employed for the time-resolved photoluminescence (PL) measurements. For the light excitation, a ps light pulser (C10196) was used. Excitation wavelength was 403 nm and pulse length was 100 ps.

From Scheme 3.2, the following coupled differential equation is obtained as a matrix form, as follows:

$$\dot{\boldsymbol{\rho}} = \boldsymbol{A}\boldsymbol{\rho} \tag{3.2}$$

where,

$$\boldsymbol{A} = \begin{pmatrix} -k_{\mathrm{Res}} & & & & \\ k_{\mathrm{Res}} & -k_0 - k_{\mathrm{CT}} & k_{\mathrm{B}} & & \\ & k_{\mathrm{CT}} & -k_{\mathrm{B}} - k_{\mathrm{CS1}} - k_{\mathrm{CR}} & k_{\mathrm{B2}} & \\ & & k_{\mathrm{CS1}} & -k_{\mathrm{T}} - k_{\mathrm{B2}} & \\ & & & k_{\mathrm{T}} & -k_{\mathrm{d}} \end{pmatrix}$$

$\boldsymbol{\rho}$ denotes vertical vector composed of ([Source], [S_1], [CT], [CS1], [CS2]), where [Source] represents source of the exciton generated by the 100 ps laser pulse. Thus, k_{Res} = 10 ns^{-1} is applied as the response rate for generating S_1 by the light irradiation.

From Eq. (3.2), $\boldsymbol{\rho} = \boldsymbol{S}\cdot\exp(\boldsymbol{k}t)\cdot\boldsymbol{S}^{-1}\boldsymbol{\rho}_0$ is computed by diagonalizing the matrix $\boldsymbol{A}$, where $\boldsymbol{S}$ and $\boldsymbol{k}$ represent the matrices of eigenvectors and eigenvalues, respectively. $[\mathrm{Source}]_0$ = 1 is considered in $\boldsymbol{\rho}_0$, while the other concentrations are set to be zero at the initial condition. Time dependences of [S_1] are plotted by the red lines in **Figure 3.13**.

Considering the peak intensity ratios at 2180 to 2205 cm^{-1} in the transient IR spectra, we assume that the quick equilibrium between S_1 and CT states is achieved to result in [S_1]:[CT] = 1:4 in **SpiroT-DCI** and [S_1]:[CT] = 1:1 in **SpiroF-DCI** by applying k_{CT} = 1.0 ps^{-1} and k_{B} = 0.24 ps^{-1} in **SpiroT-DCI** and k_{CT} = 1.1 ps^{-1} and k_{B} = 1.1 ps^{-1} in **SpiroF-DCI**. Deactivation rate constants (k_0 and k_{CR}) from the S_1 and CT1 states are obtained to be k_0 = 2.8 ns^{-1} and k_{CR} = 1.0 ns^{-1}, respectively, by fitting the decay profile in **Figure 3.13d**, assuming that the charge-separation from CT to CS1 is minor (k_{CS1} = 0.3 ns^{-1}) in **SpiroF-DCI** because of the dominant single exponential decay in **Figure 3.13**. To reproduce the double exponential behavior in **SpiroT-DCI**, k_0 = 2.8 ns^{-1} and k_{CR} = 1.0 ns^{-1} are fixed to determine the k_{CS1}, k_{B2} and k_{T}, as shown in **Table 3.3**.

Preparation of materials

Commercially available reagents were used without purification. All reactions were carried out under a nitrogen atmosphere. Compounds **1** was prepared by the reported procedures.[24]

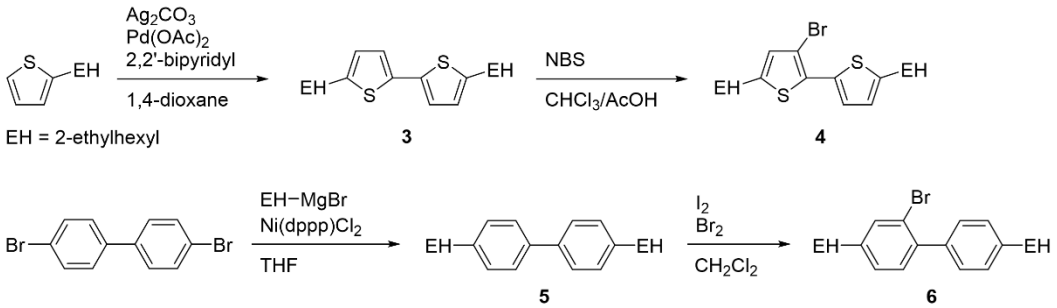

Scheme S3.1. Synthetic route of compounds **4** and **6**.

Synthetic procedures and characterizations

Synthesis of 5,5'-bis(2-ethylhexyl)-2,2'-bithiophene (**3**): Ag_2CO_3 (9.3 g, 34 mmol), palladium acetate (303 mg, 1.35 mmol), and 2,2'-bipyridyl (211 mg, 1.35 mmol) were mixed in 30 mL 1,4-dioxane under inert atmosphere, then heated to 60 °C for 30 min. 2-(2-ethylhexyl)thiophene (4.4 g, 22 mmol) was added then heated the mixture to 120 °C and stirred for 24 h. After reaction, the mixture was filtered, and the solvent was removed by reduced pressure. The crude product was purified by column chromatography on silica gel using *n*-hexane/chloroform (30/1, v/v) as an eluent to yield **3** as a colorless oil (4.2 g, 95% yield). The ^{1}H and ^{13}C NMR were the same as reported in the literature.[46]

*Synthesis of 3-bromo-5,5'-bis(2-ethylhexyl)-2,2'-bithiophene (**4**)*: 5'-bis(2-ethylhexyl)-2,2'-bithiophene (2.0 g, 5.1 mmol) was dissolved in a mixture of $CHCl_3$ (50 mL) and acetic acid (25 mL) at 0 °C. *N*-bromosuccinimide (0.9 g, 5.1 mmol) was added to the mixture over 30 min. The mixture was stirred at 0 °C for 1 h, and then at room temperature for 1 h. The reaction mixture was washed by water and brine, then dried over Na_2SO_4. The organic phase was concentrated and purified by column chromatography on silica gel using *n*-hexane as an eluent to give **4** as colorless oil (2.4 g, 99%). ^{1}H NMR (400 MHz, $CDCl_3$) δ: 7.16 (d, J = 3.60 Hz, 1H), 6.68 (d, J = 3.60 Hz, 1H), 6.63 (s, 1H), 2.73-2.71 (d, J = 6.78 Hz, 2H), 2.66-2.65 (d, J = 6.78 Hz, 2H), 1.59-1.52 (m, 2H), 1.36-1.27 (m, 16H), 0.90-0.84 (m, 12H). ^{13}C NMR (100 MHz, $CDCl_3$) δ:145.07, 142.80, 132.51, 130.45, 129.56, 125.73, 125.33, 105.78, 41.47, 41.22, 34.18, 34.09, 32.44, 32.39, 28.94, 25.59, 25.51, 23.12, 23.07, 14.26, 14.25, 10.92, 10.89. HRMS (APCI) m/z calcd. for $C_{24}H_{38}BrS_2$ $[M + H]^+$: 469.1578; found: 469.1589.

*Synthesis of 4,4'-bis(2-ethylhexyl)-1,1'-biphenyl (**5**)*: To a solution of 4,4'-dibromobiphenyl (2.0 g, 6.4 mmol) and Ni(dppp)Cl_2 (104 mg, 0.19 mmol) in THF (15 mL), 2-ethyhexylmagnesium bromide solution (prepared by 2-ethylhexyl bromide (5.5 mL, 32 mmol), magnesium (933 mg, 38 mmol), and diethyl ether (25 mL)) was added dropwise at 0 °C. The mixture was then allowed to reflux for 6 hr. After cooling to room temperature, the reaction was quenched by water and washed by water and brine. The organic phase was concentrated and purified by column chromatography on silica gel using *n*-hexane/$CHCl_3$ (20/1, v/v) as an eluent to give **5** as colorless oil (1.0 g, 42%).

^{1}H NMR (400 MHz, $CDCl_3$) δ: 7.50-7.47 (d, J = 8.25 Hz, 4H), 7.20-7.17 (d, J = 8.25 Hz, 4H), 2.59-2.50 (m, 4H), 1.62-1.53 (m, 2H), 1.34-1.24 (m, 16H), 0.89-0.85 (m, 12H). ^{13}C NMR (100 MHz, $CDCl_3$) δ: 140.77, 138.43, 129.66, 126.68, 41.20, 39.83, 32.46, 28.98, 25.52, 23.18, 14.29, 10.92. HRMS (APCI) m/z calcd. for $C_{28}H_{43}$ $[M + H]^+$: 379.3365; found: 379.3352.

*Synthesis of 2-bromo-4,4'-bis(2-ethylhexyl)-1,1'-biphenyl (**6**)*: 4,4'-bis(2-ethylhexyl)-1,1'-biphenyl (630 mg, 1.66 mmol) and a piece of iodine grain was dissolved in $CHCl_3$ (10 mL) at 0 °C, and stirred for 30 min. Then, bromine (0.1 mL, 2 mmol) was added dropwise, and the mixture was stirred at room temperature for 12 h. The solution was washed with water, $NaHCO_3$ solution, and brine. The organic phase was concentrated and purified by column chromatography on silica gel using *n*-hexane/$CHCl_3$ (30/1, v/v) as an eluent to give **6** as colorless oil (721 mg, 95%). ^{1}H NMR (400 MHz, $CDCl_3$) δ: 7.43 (s, 1H), 7.31-7.29 (d, J = 7.84 Hz, 2H), 7.22-7.17 (m, 3H), 7.11-7.09 (d, J = 7.97 Hz, 1H), 2.57-2.50 (m, 4H), 1.61-1.52 (m, 2H), 1.30-1.28 (m, 16H), 0.89-0.86 (m, 12H); ^{13}C NMR (100 MHz, $CDCl_3$) δ: 142.79, 141.16, 139.80, 138.35, 133.66, 131.02, 129.27, 128.79, 128.35, 122.38, 41.10, 41.06, 40.00, 39.45, 32.47, 32.36, 28.97, 28.91, 25.56, 25.43, 23.14, 14.27, 10.91, 10.85. HRMS (APCI) m/z calcd. for $C_{28}H_{42}Br$ $[M + H]^+$: 457.2470; found: 457.2420.

*Synthesis of **2a***: To a solution of **4** (980 mg, 2.08 mmol) in THF (40 mL) at –78 °C, *n*-butyllithium solution (2.69 M in *n*-hexane, 0.77 mL, 2.08 mmol) was added dropwise and stirred for 30 min. The solution was kept at –78 °C, and a solution of compound **1** (500 mg, 0.70 mmol) in THF (30 mL) was added dropwise. The mixture was slowly warmed up to 0 °C and stirred for 7 h and then quenched by water. The solution was extracted by $CHCl_3$ and washed with water and brine. The organic phase was concentrated and purified by column chromatography on silica gel using *n*-hexane/$CHCl_3$/EtOAc (10/2/1, v/v/v) as an eluent to give 2a as yellow solid (678 mg, 65%). This compound was subjected immediately to the next reaction without further purification. ^{1}H NMR (400 MHz, $CDCl_3$) δ: 7.32-7.30 (m, 2H), 7.27 (s, 2H), 7.09 (s, 2H), 6.17 (s, 2H), 6.04 (t, J = 4.05 Hz, 2H), 2.76 (m, 4H), 2.37 (m, 4H), 1.64-1.54 (m, 2H), 1.43-1.30 (m, 22H), 1.23-1.09 (m, 48H), 0.93-0.83 (m, 18H), 0.77-0.71 (m, 6H).

*Synthesis of **2b***: **2b** was synthesized from **1** (322 mg, 0.45 mmol) and **6** by following the procedure for **2a**. Yield: 304 mg (46%). This compound was subjected immediately to the next reaction without further purification. Yellow solid. ^{1}H NMR (400 MHz, $CDCl_3$) δ: 8.25 (s, 2H), 7.28-7.25 (m, 2H), 7.12-7.09 (d, J = 7.67 Hz, 2H), 6.80-6.77 (dd, J = 2.05, 7.54 Hz, 2H), 6.69-6.67 (m, 2H), 6.45-6.41 (m, 4H), 6.13-6.11 (t, J = 7.54 Hz, 2H), 5.90-5.86 (q, J = 6.60 Hz, 2H), 2.76 (m, 4H), 2.40-2.23 (m, 4H), 1.78 (m, 2H), 1.42-1.28 (m, 28H), 1.11-1.07 (m, 42H), 1.01-0.90 (m, 30H).

*Synthesis of **SpiroT***: To a solution of **2a** (1.5 g, 1.0 mmol) in CH_2Cl_2 (100 mL), BBr_3 solution (1 M in CH_2Cl_2, 6 mL) was added at 0 °C. The mixture was stirred at 0 °C for 3 h and quenched by water. The organic phase was concentrated and purified by column chromatography on silica gel using *n*-hexane/$CHCl_3$ (4/1, v/v) as an eluent to give **SpiroT** as light brown solid (1.0 g, 86%). ^{1}H NMR (400 MHz, $CDCl_3$) δ: 7.18-7.16 (d, J = 5.27 Hz, 2H), 7.12-7.11 (d, J = 5.12 Hz, 2H), 7.00 (s, 2H), 6.21 (s, 4H), 2.66-2.61 (m, 8H), 1.50-1.48 (m, 4H), 1.29-1.16 (m, 32H), 0.83-0.72 (m, 24H). ^{13}C NMR (100 MHz, $CDCl_3$) δ: 148.43, 147.50, 145.30, 144.83, 141.68, 140.11, 137.66, 137.36,

132.46, 126.43, 120.14, 119.76, 114.40, 59.36, 41.70, 35.09, 32.31, 28.69, 25.92, 22.95, 14.12, 11.08. HRMS (APCI) m/z calcd. for $C_{68}H_{79}S_8$ $[M + H]^+$: 1151.3947; found: 1151.3937. Elemental Anal. Calcd. for $C_{68}H_{78}S_8$: C 70.91, H 6.83, N 0.00; found: C 70.65, H 6.96, N 0.00.

Synthesis of ***SpiroF***: **SpiroF** was synthesized from **2b** (301 mg, 0.22 mmol) by following the procedure for **SpiroT**. Yield: 200 mg (87%). Yellow solid. ^{1}H NMR (400 MHz, $CDCl_3$) δ: 7.79-7.77 (d, J = 7.75 Hz, 4H), 7.19-7.17 (d, J = 7.80 Hz, 4H), 7.14-7.13 (d, J = 4.99 Hz, 2H), 7.03-7.02 (d, J = 5.01 Hz, 2H), 6.87 (s, 2H), 6.57 (s, 4H), 2.47-2.29 (m, 8H), 1.37 (m, 4H), 1.25 (m, 2H), 1.14-1.01 (m, 32H), 0.70 (t, J = 7.24 Hz, 12H), 0.65-0.60 (m, 12H). ^{13}C NMR (100 MHz, $CDCl_3$) δ: 151.50, 145.00, 143.03, 141.80, 141.53, 141.43, 139.78, 137.71, 132.45, 129.17, 126.13, 124.68, 120.10, 119.66, 114.55, 63.00, 41.07, 40.28, 31.94, 28.43, 25.69, 22.99, 14.09, 10.90. HRMS (APCI) m/z calcd. for $C_{76}H_{87}S_4$ $[M + H]^+$: 1127.5691; found: 1127.5679. Anal. Calcd for $C_{76}H_{86}S_4$: C 80.94, H 7.69, N 0.00; found: C 80.49, H 7.83, N 0.00.

Synthesis of ***SpiroT-CHO***: **SpiroT** (330 mg, 0.29 mmol) was placed in a two-necked flask and dissolved in THF (25 mL). Lithium diisopropylamide (5.72 mL, 1.0 M in THF/*n*-hexane) was added to the mixture at –78 °C. After stirring for 1 h at the temperature, *N*,*N*-dimethylformamide (0.9 mL, 11 mmol) was added. The mixture was gradually warmed up to room temperature and stirred for 12 h. The reaction was quenched by water and extracted by $CHCl_3$. After removal of the solvent under reduced pressure, the crude product was purified by column chromatography on silica gel using *n*-hexane/$CHCl_3$ (5/1, v/v) as an eluent to give **SpiroT-CHO** as orange solid (260 mg, 75%). This compound was subjected immediately to the next reaction without further purification. ^{1}H NMR (400 MHz, $CDCl_3$) δ: 9.80 (s, 2H), 7.85 (s, 2H), 7.14 (s, 2H), 6.15 (s, 4H), 2.70-2.57 (m, 8H), 1.51-1.48 (m, 4H), 1.31-1.15 (m, 32H), 0.83-0.78 (q, J = 7.30 Hz, 12H), 0.75-0.70 (m, 12H).

Synthesis of ***SpiroF-CHO***: **SpiroF-CHO** was synthesized from **SpiroF** (146 mg, 0.13 mmol) by following the procedure for **SpiroT-CHO**. This compound was subjected immediately to the next reaction without further purification. Yield: 84 mg (55%). Orange solid. ^{1}H NMR (400 MHz, $CDCl_3$) δ: 9.73 (s, 2H), 7.80 (s, 4H), 7.79 (s, 2H), 7.22-7.20 (d, J = 7.85 Hz, 4H), 7.03 (s, 2H), 6.54 (s, 4H), 2.49-2.28 (m, 8H), 1.37 (m, 4H), 1.15-0.99 (m, 32H), 0.72-0.69 (t, J = 7.34 Hz, 12H), 0.63-0.58 (m, 12H).

Synthesis of ***SpiroT-DCI***: Pyridine (1 mL) was added to the solution of **SpiroT-CHO** (260 mg, 0.22 mmol) and 3-(dicyanomethylidene)indan-1-one (250 mg, 1.29 mmol) in $CHCl_3$ (15 mL) and the resulting mixture was stirred at 75 °C for 12 h. The reaction mixture was washed by water for 3 times and the organic phase was concentrated. The crude product was purified by column chromatography on silica gel using *n*-hexane/$CHCl_3$ (2/1 to 1/2, v/v) as eluent, followed by further purification with reprecipitation using $CHCl_3$ and acetone to give **SpiroF-DCI** as deep blue solid (261 mg, 78%). ^{1}H NMR (400 MHz, $CDCl_3$) δ: 8.75 (s, 2H), 8.66-8.64 (d, J = 6.94 Hz, 2H), 8.23 (s, 2H), 7.88-7.86 (d, J = 7.19 Hz, 2H), 7.72 (m, 4H), 7.10 (s, 2H), 6.17 (s, 4H), 2.70-2.63 (m, 8H), 1.53-1.50 (m, 4H), 1.28-1.10 (m, 32H), 0.83-0.77 (q, J = 7.11 Hz, 12H), 0.73-0.65 (m, 12H). ^{13}C NMR (100 MHz, $CDCl_3$) : ^{13}C NMR (100 MHz, $CDCl_3$) δ: 160.48, 156.64, 154.15, 146.72, 146.21, 143.87, 143.48, 141.83, 140.07, 139.73, 138.34, 138.16, 138.05, 137.00, 136.26, 135.06, 134.42, 125.28, 123.79, 123.08, 122.76, 119.12, 115.72, 114.51, 69.50,

59.15, 41.69, 35.20, 32.37, 28.68, 25.98, 22.86, 13.94, 10.98. HRMS (APCI) m/z calcd. for $C_{94}H_{86}N_4O_2S_8$ $[M]^+$: 1559.4550; found: 1559.4581. Elemental Anal. Calcd. for $C_{94}H_{86}N_4O_2S_8$: C 72.36, H 5.56, N 3.59; found: C 72.20, H 5.83, N 3.42.

*Synthesis of **SpiroF-DCI***: **SpiroF-DCI** was synthesized from **SpiroF-CHO** (70 mg, 0.06 mmol) by following the procedure for **SpiroT-DCI**. Yield: 73 mg (60%). Deep blue solid. ^{1}H NMR (400 MHz, $CDCl_3$) δ: 8.71 (s, 2H), 8.63-8.61 (d, J = 7.43 Hz, 2H), 8.19 (s, 2H), 7.86-7.84 (d, J = 7.78 Hz, 4H), 7.81-7.79 (d, J = 6.24 Hz, 2H), 7.73-7.65 (m, 4H), 7.23 (s, 2H), 6.96 (s, 2H), 6.54 (s, 4H), 2.50-2.27 (m, 8H), 1.36 (m, 4H), 1.18-0.98 (m, 32H), 0.71-0.98 (t, J = 7.13 Hz, 12H), 0.59-0.53 (m, 12H). ^{13}C NMR (100 MHz, $CDCl_3$) δ: 187.71, 160.39, 145.74, 144.03, 141.89, 141.82, 140.05, 139.95, 139.62, 138.31, 138.04, 136.92, 136.36, 135.04, 134.36, 129.83, 129.75, 125.27, 124.27, 123.70, 122.88, 120.43, 120.40, 115.96, 114.59, 114.48, 69.42, 63.04, 41.14, 40.40, 32.10, 28.57, 25.80, 22.94, 13.90, 10.85. HRMS (APCI) m/z calcd. for $C_{102}H_{95}N_4O_2S_4$ $[M + H]^+$: 1535.6293; found: 1535.6351. Elemental Anal. Calcd. for $C_{102}H_{94}N_4O_2S_4$: C 79.75, H 6.17, N 3.65; found: C 79.52, H 6.29, N 3.52.

3.11 References

1 Wang J. Y., Zhan X. W., *Acc. Chem. Res.* **2021**, *54*, 132-143.

2 Wang H. T., Cao J. R., Yu J. S., Zhang Z. H., Geng R. Y., Yang L. Q., Tang W. H., *J. Mater. Chem. A* **2019**, *7*, 4313-4333.

3 Murugan P., Hu T., Hu X. T., Chen Y. W., *J. Mater. Chem. A* **2022**, *10*, 17968-17987.

4 Forti G., Nitti A., Osw P., Bianchi G., Po R., Pasini D., *Int. J. Mol. Sci.* **2020**, *21*, 8085.

5 Scharber M. C., Koppe M., Gao J., Cordella F., Loi M. A., Denk P., Morana M., Egelhaaf H. J., Forberich K., Dennler G., Gaudiana R., Waller D., Zhu Z. G., Shi X. B., Brabec C. J., *Adv. Mater.* **2010**, *22*, 367-370.

6 Forrest S. R., *Philos. T. R. Soc. A* **2015**, *373*, 20140320.

7 Meng R. X., Li Y., Li C., Gao K., Yin S., Wang L. X., *Phys. Chem. Chem. Phys.* **2017**, *19*, 24971-24978.

8 Gledhill S. E., Scott B., Gregg B. A., *J. Mater. Res.* **2005**, *20*, 3167-3179.

9 Nayak P. K., *Synthetic Met.* **2013**, *174*, 42-45.

10 Menke S. M., Ran N. A., Bazan G. C., Friend R. H., *Joule* **2018**, *2*, 25-35.

11 Huang T. Y., Bai Y. M., Wang J., Wang F. Z., Dai M. L., Han F., Du S. X., *Sol. Energy* **2021**, *230*, 628-634.

12 Carsten B., Szarko J. M., Son H. J., Wang W., Lu L. Y., He F., Rolczynski B. S., Lou S. J., Chen L. X., Yu L. P., *J. Am. Chem. Soc.* **2011**, *133*, 20468-20475.

13 Knupfer M., *Appl. Phys. A* **2003**, *77*, 623-626.

14 Zhu Y. F., Zhao F. W., Wang W., Li Y. W., Zhang S. M., Lin Y. Z., *Adv. Energy Sustainability Res.* **2022**, *3*, 2100184.

15 Leenaers P. J., Maufort A. J. L. A., Wienk M. M., Janssen R. A. J., *J. Phys. Chem. C* **2020**, *124*, 27403-27412.

16 Zhang J. Y., Guan J. X., Zhang Y. G., Qin S. C., Zhu Q. Y., Kong X. L., Ma Q., Li X. J., Meng L., Yi Y. P., Zheng J. R., Li Y. F., *J. Phys. Chem. Lett.* **2022**, *13*, 8816-8824.

17 Li T. F., Wang K., Cai G. L., Li Y. W., Liu H., Jia Y. X., Zhang Z. Z., Lu X. H., Yang Y., Lin Y. Z., *JACS Au* **2021**, *1*, 1733-1742.

18 Jinnai S., Murayama K., Nagai K., Mineshita M., Kato K., Muraoka A., Yamakata A., Saeki A., Kobori Y., Ie Y., *J. Mater. Chem. A* **2022**, *10*, 20035-20047.

19 Zhong S. H., Huang Z. G., Lin X. X., Zeng Y., Ma Y. C., Shen W. Z., *Adv. Mater.* **2015**, *27*, 555-561.

20 Shi Y. A., Chang Y. L., Lu K., Chen Z. H., Zhang J. Q., Yan Y. J., Qiu D. D., Liu Y. A., Adil M. A., Ma W., Hao X. T., Zhu L. Y., Wei Z. X., *Nat. Commun.* **2022**, *13*, 3256.

21 Tang X., Cui L. S., Li H. C., Gillett A. J., Auras F., Qu Y. K., Zhong C., Jones S. T. E., Jiang Z. Q., Friend R. H., Liao L. S., *Nat. Mater.* **2020**, *19*, 1332-1338.

22 Le Bahers T., Adamo C., Ciofini I., *Journal of Chemical Theory and Computation* **2011**, *7*, 2498-2506.

23 Kraner S., Prampolini G., Cuniberti G., *J. Phys. Chem. C* **2017**, *121*, 17088-17095.

24 Wang J. L., Zhang H. J., Liu S., Liu K. K., Liu F., Wu H. B., Cao Y., *Sol. Rrl* **2018**, *2*, 1800108.

25 Yoshida H., *Chem. Phys. Lett.* **2012**, *539*, 180-185.

26 Yoshida H., *Anal. Bioanal. Chem.* **2014**, *406*, 2231-2237.

27 Yoshida H., *J. Electron. Spectrosc. Relat. Phenom.* **2015**, *204*, 116-124.

28 Yang J. P., Bussolotti F., Kera S., Ueno N., *J. Phys. D: Appl. Phys.* **2017**, *50*, 423002.

29 Tamai Y., Shirouchi R., Saito T., Kohzuki K., Natsuda S., *J. Mater. Chem. A* **2023**, *11*, 17581-17593.

30 Scharber M. C., Wühlbacher D., Koppe M., Denk P., Waldauf C., Heeger A. J., Brabec C. L., *Adv. Mater.* **2006**, *18*, 789-794.

31 Peng X. J., Song F. L., Lu E., Wang Y. N., Zhou W., Fan J. L., Gao Y. L., *J. Am. Chem. Soc.* **2005**, *127*, 4170-4171.

32 Benniston A. C., Harriman A., Lawrie D. J., Mayeux A., *Phys. Chem. Chem. Phys.* **2004**, *6*, 51-57.

33 Wu Y. Y., Chen Y., Gou G. Z., Mu W. H., Lv X. J., Du M. L., Fu W. F., *Org. Lett.* **2012**, *14*, 5226-5229.

34 Qian D. P., Ye L., Zhang M. J., Liang Y. R., Li L. J., Huang Y., Guo X., Zhang S. Q., Tan Z. A., Hou J. H., *Macromolecules* **2012**, *45*, 9611-9617.

35 Malliaras G. G., Salem J. R., Brock P. J., Scott C., *Phys. Rev. B* **1998**, *58*, 13411-13414.

36 Goh C., Kline R. J., McGehee M. D., Kadnikova E. N., Fréchet J. M. J., *Appl. Phys. Lett.* **2005**, *86*, 122110.

37 Dimitrov S. D., Durrant J. R., *Chem. Mater.* **2014**, *26*, 616-630.

38 Wu J. L., Chen F. C., Hsiao Y. S., Chien F. C., Chen P. L., Kuo C. H., Huang M. H., Hsu C. S., *ACS Nano* **2011**, *5*, 959-967.

39 Proctor C. M., Kim C., Neher D., Nguyen T. Q., *Adv. Funct. Mater.* **2013**, *23*, 3584-3594.

40 Kupgan G., Chen X. K., Brédas J. L., *Mater. Today Adv.* **2021**, *11*, 100154.

41 Han G. C., Guo Y., Song X. X., Wang Y., Yi Y. P., *J. Mater. Chem. C* **2017**, *5*, 4852-4857.

42 Mani T., Grills D. C., Newton M. D., Miller J. R., *J. Am. Chem. Soc.* **2015**, *137*, 10979-10991.

43 Song Y., Liu X., Li Y. X., Nguyen H. H., Duan R., Kubarych K. J., Forrest S. R., Ogilvie J. P., *J. Phys. Chem. Lett.* **2021**, *12*, 3410-3416.

44 Zhao W. C., Li S. S., Yao H. F., Zhang S. Q., Zhang Y., Yang B., Hou J. H., *J. Am. Chem. Soc.* **2017**, *139*, 7148-7151.

45 Case D. A., Darden T. A., Cheatham T. E. I., Simmerling C. L., Wang J., Duke R. E., Luo R., Merz K. M., Pearlman D. A., Crowley M., Walker R. C., Zhang W., Wang B., Hayik S., Roitberg A., Seabra G., Wong K. F., Paesani F., Wu X., Brozell S., Tsui V., Gohlke H., Yang L., Tan C., Mongan J., Hornak V., Cui G., Beroza P.,

Mathews D. H., Schafmeister C., Ross W. S., Kollman P. A., *AMBER*, University of California, San Francisco, 2016.

46 An C. B., Puniredd S. R., Guo X., Stelzig T., Zhao Y. F., Pisula W., Baumgarten M., *Macromolecules* **2014**, *47*, 979-986.

Conclusion

This dissertation presents a comprehensive investigation into the relationship between molecular structure, electronic properties, E_b, and device performance in ITIC-based NFAs for organic solar cells.

In Chapter 1, a novel ITIC isomer, **io-ITIC**, was designed and synthesized to examine the effect of molecular configuration on photophysical and photovoltaic properties. Electrochemical analyses revealed a lower HOMO energy level in solution and a slightly higher ionization energy in the solid state relative to ITIC, resulting in a reduced E_b. Molecular dynamics simulations suggested that the V-shaped molecular backbone promotes multiple stacking modes, thereby contributing to the reduction of E_b and offering valuable insights into NFA design strategies.

Chapter 2 focused on the impact of aggregation behavior on V_{OC} using **im-ITIC**, a C_{2v} symmetric isomer featuring side-chain arrangement on one side of the core. Concentration-dependent NMR and single-crystal X-ray diffraction confirmed the coexistence of H- and J-aggregates in the solid state. Compared to ITIC, **im-ITIC** exhibited a smaller E_b, prolonged free carrier lifetimes in pristine films, and a notably higher V_{OC} in OSC devices. Time-resolved infrared spectroscopy and TD-DFT calculations revealed that the presence of H-aggregation at the D/A interface elevates the E_{CT}, correlating with the observed V_{OC} enhancement. These findings underscore the critical role of aggregation behavior, induced by molecular design, in modulating electronic interactions and device performance.

In Chapter 3, the role of frontier molecular orbital distribution was elucidated using ITIC derivatives incorporating spiro-substituted bithiophene or biphenyl units. Introduction of electron-donating bithiophene units in **SpiroT-DCI** resulted in spatially decoupled HOMO and LUMO distributions, leading to an ultralow E_b of 0.32 eV, as compared to **SpiroF-DCI** and ITIC. **SpiroT-DCI**-based OSCs exhibited significantly improved charge separation efficiency, prolonged free carrier lifetimes, and a maximum PCE of 9.08%. These results demonstrate that precise modulation of FMO distribution offers an effective strategy to minimize E_b and enhance device performance.

Overall, this dissertation establishes a fundamental understanding of how molecular configuration, aggregation behavior, and electronic structure govern exciton dynamics and photovoltaic properties in NFAs. The insights gained herein provide clear design principles for the development of next-generation high-efficiency OSC materials.

List of Publications

1 A V-shaped analogue of ITIC with a small exciton binding energy
Wang, K.; Jinnai, S.; Ie, Y.
Chem. Lett. **2024**, *53*, upae220.

2 A *meta*-linked isomer of ITIC: influence of aggregation patterns on open-circuit voltage in organic solar cells
Wang, K.; Jinnai, S.; Uesaka, K.; Yamakata, A.; Ie, Y.
J. Mater. Chem. A, **2025**, *13*, 17720-17729.

3 Nonfullerene Acceptors Bearing Spiro-Substituted Bithiophene Units in Organic Solar Cells: Tuning the Frontier Molecular Orbital Distribution to Reduce Exciton Binding Energy
Wang, K.; Jinnai, S.; Urakami, T.; Sato, H.; Higashi, M.; Tsujimura, S.; Kobori, Y.; Adachi, R.; Yamakata, A.; Ie, Y.
Angew. Chem. Int. Ed. **2024**, *63*, e202412691.

(List of Supplementary Publications)

1 Benzothiadiazole-Based Fused-Ring Electron Acceptors for Green-Light Wavelength-Selective Organic Solar Cells
Jinnai, S.; Shiono, Y.; Wang, K.; Iimuro, Y.; Watanabe, Y.; Kato, S.; Ie, Y.
J. Photopolym. Sci. Technol., **2025**, *38*, 285-290.

2 Novel Core-substituted Naphthalene Diimide-based Conjugated Polymers for Electrochromic Applications
Wang, K.; Zhu, L.; Hu, X. L.; Han, M. X.; Lin, J. Y.; Guo, Z. Y.; Zhan, H. B.
J. Mater. Chem. C **2021**, *9*, 16959-16965.

3 Diversified AIE and Mechanochromic Luminescence Based on Carbazole Derivative Decorated Dicyanovinyl Groups: Effects of Substitution Sites and Molecular Packing
Wang, K.; Xiao, H.; Qian L.; Han, M. X.; Wu, X. F.; Guo, Z. Y.; Zhan, H. B.
CrystEngComm **2020**, *22*, 2166-2172.

4 Symmetric Variation of Monomers for Constructing 1D/2D Imine-Based Covalent Organic Frameworks
Shi, P. Z.; Wang, K.; Chen, Z. A.; Wang, J. W.; Lin, K. F., Solange, N. L.; Yue, Y. F.; Guo, Z. Y.
CCS Chem. **2024**, *6*, 941–952.

5 Reticular Synthesis of One-Dimensional Covalent Organic Frameworks with 4-c sql Topology for Enhanced Fluorescence Emission
Chen, Z. A.; Wang, K.; Tang, Y. M.; Li, L.; Hu, X. L.; Han, M. X.; Guo, Z. Y.; Zhan, H. B.; Chen, B. L.
Angew. Chem. Int. Ed. **2023**, *62*, e202213268.

6 A Thin Film of Naphthalenediimide-based Metal-organic Framework with Electrochromic Properties
Wu, X. F.; Wang, K.; Lin, J. Y.; Ya, D.; Guo, Z. Y.; Zhan, H. B.
J. Colloid Interface Sci. **2021**, *594*, 73-79.

7 Novel One-Dimensional Covalent Organic Framework as a H^+ Fluorescent Sensor in Acidic Aqueous Solution
Chen, Z. A.; Wang, K.; Hu, X. L; Shi, P. Z.; Guo, Z. Y.; Zhan, H. B.
ACS Appl. Mater. Interfaces **2021**, *13*, 1145-1151.

Acknowledgements

I have walked a long and often solitary road to reach this point, this moment, this thesis. There were long stretches when progress was imperceptible, when questions multiplied faster than answers, and when conviction gave way, quietly but steadily, to doubt. Yet through these silent intervals, I came to understand that the pursuit of knowledge is seldom a path of certainty, but rather one of enduring ambiguity—and that perseverance, above all, is the quiet work of continuing without assurance.

I owe my deepest gratitude to Professor Yutaka Ie, for his professional guidance and invaluable advice throughout my doctoral research. His expertise, rigor, and high standards have profoundly shaped the way I approach science.

I am equally grateful to Dr. Seihou Jinnai, whose patient mentorship, unwavering support, and creative scientific thinking have greatly enriched my research journey. His meaningful discussions and insightful ideas have been a constant source of inspiration and encouragement.

I would also like to express my sincere thanks to Dr. Naoki Ando and Dr. Soichi Yokoyama for their frequent guidance and valuable suggestions during my time in the laboratory.

I am deeply appreciative of Dr. Chatterjee Shreyam for his professional support and instruction in the fabrication of organic solar cells.

My sincere thanks also go to Mr. Takuji Seo, Dr. Hajime Nitta, and Dr. Yasushi Hosoda for their helpful guidance in organic synthesis.

I am truly grateful to Dr. Dayang Zhou and Dr. Tsunayoshi Takehara at the Analytical Center for their expert support in NMR and single-crystal XRD measurements.

I also appreciate the scientific assistance provided by Professor Akira Yamakata, Professor Yasuhiro Kobori, Professor Hirofumi Sato, and Professor Masahiro Higashi during my experimental work.

I wish to thank my labmates—Ryo Asakawa, Hiroki Mori, Yue Zhang, and Dr. Chauhan Navya—for their invaluable help and discussions, which made the research process both more fruitful and more enjoyable.

I am also sincerely thankful to Professor Mamoru Fujitsuka and Professor Toshiyuki Kida for their careful guidance during the preparation and defense of this dissertation.

Finally, I owe my deepest gratitude to my parents, whose silent, unwavering support has been the foundation of all my efforts. Their presence, though distant in miles, has been near in every moment of doubt and silence. It is their steadfast love, their quiet sacrifices, and their enduring faith in me that have formed the unseen foundation beneath every step of this journey.